Adaptive Digital Beam-Forming for High-Resolution Wide-Swath Synthetic Aperture Radar

Master Thesis
by
Eduardo Makhoul Varona

Deutsches Zentrum für Luft-und Raumfahrt

Institut für Hochfrequenztechnik und Radarsysteme

Advisor: Dr. Federica Bordoni

Universitat Politècnica de Catalunya

Escola Tècnica Superior d'Enginyeria de Telecomunicacions de Barcelona

Co-Advisor: Prof. Antoni Broquetas Ibars

Acknowledgment

Since I entered the University, seven years have passed fast and now I am writing the last lines of my Master thesis. It has been a long and tough way, but with effort and commitment you can always make it. It would not be possible to finish my thesis work if it were not for help from my family, my advisors and my friends.

First of all, I'd like to express my immense gratitude to my family. I will be always indebted to my parents and my sisters for their unconditional love, support and encouragement. I would say that the Master degree is earned by them, not me.

I would like specially to thank my thesis advisor, Dr. Federica Bordoni, who always helped me in every step of the way. Her guidance and support have been really helpful. Dr. Marwan Younis was always willing to help me when I was in trouble. Thanks, Marwan. I also would like to thank my co-advisor Prof. Antoni Broquetas for his support.

During the months I worked at the Microwaves and Radar Institute of the DLR, I was lucky to meet a lot of nice colleagues. Marc. We used to have long conversations with a nice cup of tea. Thank you a lot for your advices. Nico. Thanks also for your advices and your "good" jokes. Martina, my office mate, always helped me in all the doubts I had. I am also grateful to Nicola, Francesco, Marcos, Anton, Prabu, Enrique and all the nice people I met during this great personal and professional experience.

My sincere thanks go to all my friends that gave their support during these years. Especially thanks and appreciation to Quim, Mario and Edu for the great people they are, and for their support.

To all these people that in someway have helped me to become the person I am, thanks.

To my grandfather.

My great family.

“Progress lies not in enhancing what is, but in advancing toward what will be”

Khalil Gibran

List of Acronyms

AASR	Azimuth-Ambiguity-to-Signal Ratio
ADBF	Adaptive Digital Beam-Forming
ASNR	Array Signal-to-Noise Ratio
CRLB	Cramér-Rao Lower Bound
CSS	Coherent Signal-Subspace
DFT	Discrete Fourier Transform
DOA	Direction of Arrival
DPCA	Displaced Phase Center Antenna
ECSS	Extended Coherent Signal-Subspace
DFT	Discrete Fourier Transform
FFT	Fast Fourier Transform
FIM	Fisher Information Matrix
FM	Frequency Modulation
FT	Fourier Transform
HPBW	Half Power Beamwidth
ISS	Incoherent Signal-Subspace
InSAR	Interferometric Synthetic Aperture Radar
MUSIC	MUltiple SIgnal Classification
NESZ	Noise-Equivalent Sigma Zero
PL	Pattern Loss
PRF	Pulse Repetition Frequency
PRI	Pulse Repetition Interval
PSD	Power Spectral Density
RADAR	RAdio Detection And Ranging
RAR	Real Aperture Radar
RASR	Range-Ambiguity-to-Signal Ratio
RCM	Range Cell Migration
RCMC	Range Cell Migration Correction
SAR	Synthetic Aperture Radar
SCORE	SCan-On-REceive
SMART	Smart Multi-Aperture Radar Technique
SNR	Signal-to-Noise Ratio
STFD	Spatial Time-Frequency Distributions
SVD	Singular Value Decomposition
ULA	Uniform Linear Array
UR	Unambiguous DOA Range

Table of Contents

List of Figures

List of Symbols

$\mathbf{b}^H$, $\mathbf{B}^H$	Conjugate transpose
$\mathbf{b}^T$, $\mathbf{B}^T$	Transpose
$\mathbf{B}^{-1}$	Inverse of $\mathbf{B}$
$\mathbf{B}^*$	Conjugate of $\mathbf{B}$
$b(\hat{\theta})$	Bias of the estimation $\hat{\theta}$
$E\{\cdot\}$	Mean statistical value
*	Convolution
$\otimes$	Hadamard product
$RMSE(\hat{\theta})$	Root Mean Square Error of the estimation $\hat{\theta}$
$std(\hat{\theta})$	Standard deviation of the estimation $\hat{\theta}$
$\text{var}(\hat{\theta})$	Variance of the estimation $\hat{\theta}$
A_a	Antenna area
$\mathbf{a}(\theta)$	$Kx1$ steering vector
$\mathbf{A}_i$	KxK diagonal matrix (steering vector $\mathbf{a}(\theta_i)$ in the diagonal)
$\mathbf{A}$	KxN_s steering matrix (columns steering vectors of N_s sources)
BW	Radar bandwidth
c_0	Speed of light $= 2.998x10^8$ m/s
$C^R(\theta)$	Elevation receive beam pattern at angle θ
$\mathbf{C}_i$	KxK speckle covariance matrix of the $i-th$
d	Inter-element spacing
$e_k(t)$	Additive thermal noise at the $k-th$ element or sub-aperture
$E_k(\omega)$	Fourier Transform of the $k-th$ element noise $e_k(t)$
$\mathbf{e}$	$Kx1$ array noise vector
$\mathbf{E}$	KxK exchange matrix (1's anti-diagonal zero elsewhere)
$\hat{\mathbf{E}}$	$Kx(K-N_s)$ matrix of eigenvectors of smallest eigenvalues of $\hat{\mathbf{R}}_\mathbf{y}$
f	Frequency
f_c	Carrier frequency
$f_N(\mathbf{y},\boldsymbol{\chi})$	Joint probability density function of the N samples of $\mathbf{y}$
g_i	Ground position of the $i-th$ source
$\mathbf{G}$	Transformation parameters matrix
h	Topographic height
$h_k(t)$	Impulse response of the $k-th$ element or sub-aperture
h_{rs}	Receive sub-aperture height
H_a	Antenna height
$H_{c,i}$	Critical antenna height for the $i-th$ source
H_i	Normalized antenna height for the $i-th$ source
$H_k(\omega)$	Fourier Transform of $k-th$ element response $h_k(t)$

H_{orb}	Satellite's orbit height
H_{tx}	Transmit antenna height
H_{rx}	Receive antenna height
$\mathbf{h}$	$Kx1$ vector of the filter complex coefficients
	$N_s x1$ vector of normalized antenna heights $\{H_i\}_{i=1}^{N_s}$
$\mathbf{h}_{BF}$	Complex coefficients of Beamformer filter
$\mathbf{h}_C$	Complex coefficients of Capon filter
$\mathbf{I}$	Identity matrix (1's diagonal and 0's elsewhere)
$\mathbf{J}_{FIM}$	Fisher Information Matrix
K	Number of array elements or sub-apertures in elevation
L_a	Antenna length
L_{sa}	Synthetic aperture length
L_{tx}	Transmit antenna length
L_{rx}	Receive antenna length
$\mathbf{L_0}$	KxK Toeplitz matrix $[\mathbf{L_0}]_{i,j} = \lvert i-j \rvert$
$\mathbf{L_1}$	KxK Toeplitz matrix $[\mathbf{L_1}]_{i,j} = -\lvert i-j \rvert / (K-1)$
M	Number of sub-apertures in azimuth
N	Number of snapshots or samples
N_F	Number of far range ambiguities
N_N	Number of near range ambiguities
N_s	Number of sources
$\hat{P}_{BF}(\omega_s)$	Beamformer functional
$\hat{P}_C(\omega_s)$	Capon functional
$\hat{P}_M(\omega_s)$	MUSIC functional
Q	Distance between the phase centers of the extreme sub-apertures
Q_O	Orthogonal component of Q, $Q_O = Q \cdot \sin(\beta)$
Q_P	Parallel component of Q, $Q_P = Q \cdot \cos(\beta)$
$Q_\perp$	Orthogonal projection of Q to line of sight, $Q_\perp = Q \cdot \cos(\beta - \theta)$
$r(t)$	Baseband received signal
$r_k(t)$	Baseband received signal at the $k-th$ sub-aperture
R_c	Slant range to the center of the swath
R_E	Radius of the earth
R_{horiz}	Slant range at the horizon
R_{fr}	Slant range at far edge of the swath
R_{nr}	Slant range at near edge of the swath
R_0	Slant range of closest approach
R_n	Slant range distance for the $n-th$ snapshot
$\mathbf{R_y}$	KxK spatial covariance matrix
$\hat{\mathbf{R}}_\mathbf{y}$	KxK spatial covariance matrix estimate

$\tilde{\mathbf{R}}_{\mathbf{y}}$	$\mathbf{R}_{\mathbf{y}}$ estimate using forward-backward averaging
$s(t)$	Baseband transmitted signal
$S(\omega)$	Fourier Transform of the transmitted signal $s(t)$
$\mathbf{s}(t)$	$N_s x1$ vector of signals
t	Fast or range time
t_{az}	Slow or azimuth time
t_{fr}	Two-way time delay at far edge of the swath
t_{nr}	Two-way time delay at near edge of the swath
T	Pulse duration
T_{ia}	Illumination time
V_s	Satellite velocity
$x(t)$	Bandpass transmitted signal
$\mathbf{x}_i$	$Kx1$ speckle vector of the $i-th$ source
$y_k(t)$	Signal at the output of the $k-th$ sub-aperture
$Y_k(\omega)$	Fourier Transform of the $k-th$ element output signal
$\mathbf{y}$	$Kx1$ array output signal vector
α_i	Radar reflectivity or texture of the $i-th$ source
	Local terrain slope of the $i-th$ source
$\boldsymbol{\alpha}$	$N_s x1$ vector of textures $\{\alpha_i\}_{i=1}^{N_s}$
β	Antenna tilt angle
γ	Angle at the center of the earth
γ_i	Propagation and backscattering of the $i-th$ source
$\delta(\cdot)$	*Kronecker* delta function
δ_{az}	Azimuth resolution
δ_{sr}	Slant range resolution
$\Delta\Omega_{az}$	Azimuth antenna beamwidth
$\Delta\Omega_{el}$	Elevation antenna beamwidth
$\Delta\theta_a$	ADBF angular displacement
$\Delta\theta_s$	SCORE angular displacement
$\Delta\tau_k$	Time delay between reference and $k-th$ sub-aperture
ΔW_g	Ground range swath width
ΔW_s	Slant range swath width
κ_r	Frequency rate of linear FM waveform (chirp rate)
η	Incidence angle between radar beam and local normal
θ	DOA of the actual echo w.r.t. nadir
$\hat{\theta}$	Estimate of the actual echo DOA
$\theta_s(t)$	SCORE steering angle w.r.t. nadir
λ	Carrier wavelength
σ_e^2	Noise variance

τ_k	Time delay at the $k-th$ sub-aperture
τ_0	Time delay at the reference sub-aperture
$\boldsymbol{\chi}$	Vector of unknown deterministic parameters to estimate
ω	Radian frequency $= 2\pi f$ in $\left[rad/\mathrm{s}\right]$
ω_c	Radian carrier frequency
ω_s	Spatial frequency
$\omega_{s,i}$	Spatial frequency of the $i-th$ source
$\boldsymbol{\omega}$	$N_s x1$ vector of spatial frequencies $\left\{\omega_{s,i}\right\}_{i=1}^{N_S}$
Ω	Signal bandwidth in $\left[rad/\mathrm{s}\right]$

List of Tables

Chapter 1 Introduction

1.1 Objectives and contributions

Spaceborne SAR systems for remote sensing applications are gaining special interest during the last decade, as testified by the increased number of recent and forthcoming missions, e.g. TerraSAR-X, COSMO-SkyMed, RADARSAT-2, and TanDEM-X. However, the conventional spaceborne SAR has a basic limitation: it is not possible to achieve high resolution and, simultaneously, wide coverage and high radiometric resolution [14],[17],[35]. The importance for many remote sensing applications to overcome these contradicting requirements has motivated the development of new SAR concepts in the framework of *Smart Multi-Aperture Radar Technique* (SMART) [32],[55].

The core of the SMART SAR systems is the use of multiple transmit/receive sub-apertures in combination with digital signal processing techniques, such as Digital Beam-Forming (DBF) [19],[32],[54],[55]. The flexibility of multi-channel structures provide a relaxation on the SAR system design constrains, which results in an improved radiometric resolution and reduction of the classical trade-off between swath width (coverage) and spatial resolution.

Among SMART SAR, the system denoted as HRWS and proposed by *Suess et al.* [45],[46], represents an approach that allows obtaining an extensive illumination capability with high gain (radiometric resolution). A wide swath is illuminated using a small transmit antenna. In reception a large multi-channel antenna in elevation and DBF provides a sharp and high gain pattern, which follows the pulse echo as it travels along the ground swath. This scansion of the receive pattern in elevation is performed through SCORE algorithm, where the steering direction corresponds to the a *priori* known DOA of the echo. In particular, according to [46], it is computed based on the vertical, slant-range plane acquisition geometry, under the hypothesis of spherical Earth model, where no topographic height is taken into account. The main drawback of this approach is that in real acquisition scenarios, characterized by mountains and relief, the steering direction (i.e. maximum gain) doesn't match the actual DOA of the echo. Therefore, when no information about the acquisition geometry is included in the steering mechanism, losses of several dBs could be obtained [7].

This situation has suggested the option to compute *adaptively* the steering direction of the receive beam, by processing the signals from the multiple sub-apertures in elevation. This information can be used to evaluate the distribution of the received power as a function of the DOA. This alternative is cast in the well-studied field of *spatial spectral estimation* and *DOA estimation* [33],[44],[50]. Nevertheless, the applicability to HRWS SAR spaceborne shows some peculiarities/challenges. In fact, the processing of the signals should be performed on board (reducing downlink data volume) and this requires dealing with wideband chirp signals.

These observations motivated, in the development of the thesis, a search in the DOA estimation literature for an algorithm that could fulfill those requirements. The well-known and simple narrowband spectral estimation methods as *Beamformer*, *Capon* or *MUltiple SIgnal Classification* (MUSIC) can not be directly applied to the wideband SAR signals. Conventional approaches, like *incoherent* and c*oherent* s*ignal sub-space* methods [51] and [52], extend the estimation to wideband signals, but do not constitute the optimum solution in the case of chirp signals. Recently, several approaches that exploit the time-frequency structure of the chirp pulses have been proposed [3],[20],[37],[53]. However, their additional complexity formulation and computational cost do not suggest their applicability on the HRWS SAR.

Based on the pervious considerations, a new algorithm, denoted as *Adaptive Digital Beam-Forming* (ADBF) is presented in this thesis. The problem of estimating the DOA of the echo at each instant of the receiving time-window is addressed by analyzing the signals at the different vertical sub-apertures, after performing on-board *range compression* and *coregistration*. This preprocessing allows tracing back the SAR signal to a well-extended narrowband DOA estimation model [44],[50]. In particular, the DOA associated to each range sample is estimated by Beamformer and Capon.

This work also analyzes the performance of the ADBF comparatively with the conventional SCORE. It is known that instrument parameters, such as dimension of the antenna, number of elements and noise level affect the estimation performance and do not allow for many degrees of freedom due to imaging requirements and physical/economical constrains. Monte Carlo simulations evaluate the ADBF in a realistic SAR operational scenario versus the main system parameters. Additionally, the Cramér-Rao Lower Bound (CRLB) analysis provides the means to study the potentiality of the ADBF, setting a benchmark in the achievable performance [44],[50].

The numerical results obtained suggest the ADBF as a possible alternative, outperforming SCORE in most of the analyzed scenario/system parameters conditions [7],[8],[9].

1.2 Structure of the thesis

The thesis has been structured in 8 chapters. Chapter 2 provides a review of the main concepts behind Synthetic Aperture Radar and introduces the basics of high-resolution wide-swath SAR. Specifically, the HRWS SAR system in junction with SCORE algorithm are described.

The key point on the ADBF algorithm is the estimation of the actual echo DOA. Then, Chapter 3 presents a general characterization of the DOA estimation problem and its possible application on the SAR field through a brief discussion of some of the existing DOA estimation algorithms.

Chapter 4 describes the ADBF algorithm based on a preprocessing of the received data at the different sub-apertures, i.e. range compression and coregistration, which allows recovering a narrowband data model. The different considerations for this model are discussed. Then, narrowband spectral estimation methods as Beamformer, Capon and MUSIC are presented.

The correct description of the data model constitutes a key point for any estimation problem. Chapter 5 formulates the signal model after pre-processing, considering extended sources limited by the azimuth pattern and the range cell dimension. A statistical characterization of the model is also assumed, which is required to perform a numerical analysis of the ADBF performance.

The ultimate performance of any (unbiased) estimation algorithm is provided by the Cramér-Rao Lower Bound. In Chapter 6, this statistical tool is formulated and derived for the data model considered in Chapter 5.

In Chapter 7, Monte Carlo simulations of the ADBF performance are presented and comparatively discussed with conventional SCORE and the CRLB. Several scenarios have been considered, where single parameters of interest are varied at once. The different performance measures and the realistic reference SAR system scenario are also described.

Finally, Chapter 8 concludes with the contributions of the thesis and the future lines of study.

Chapter 2 SAR fundamentals

The first part of this chapter reviews the basics of the classical Synthetic Aperture Radar, with special interest on SAR ambiguities and the related antenna's size constrain. The implicit trade-off between these two concepts has motivated the study of new SAR systems, which provide simultaneously high-resolution and wide-swath. Among them, it is considered the so called HRWS in combination with a digital beam-forming technique, SCan-On-REceive. The second part of the chapter presents a general description of this novel system as well as the operational principle and limitation of the SCORE algorithm.

2.1 Conventional SAR

The Synthetic Aperture Radar is a coherent[1] Radar system, which is able to retrieve high resolution images of the Earth's surface. The basic idea behind the SAR is to illuminate a certain terrain area with a sequence of electromagnetic pulses. Then, an image of the reflectivity is obtained after the processing of successive echoes received form the terrain. SAR systems work in the microwave spectral range (from 0.3 GHz to 300 GHz), which allows operating almost independently on the atmospheric conditions as well as during the night.

In conventional Real Aperture Radars (RAR) the resolution δ_{az} in the *along-track*[2] or azimuth direction is limited by the length of the real antenna [14]:

$$\delta_{az} = \Delta\Omega_{az} \cdot R_0 = \frac{\lambda}{L_a} \cdot R_0 \tag{2.1}$$

where $\Delta\Omega_{az}$ is the azimuth antenna beamwidth[3] , λ is the wavelength, L_a the antenna length and R_0 is the slant range distance (satellite-target).

From Eq. (2.1) the azimuth resolution could be very poor for long ranges (R_0) upon a given working frequency. A SAR can improve its azimuth resolution (δ_{az}) using the Doppler or phase content of several successive radar returns. This is the principle that constitutes the basis of the SAR, where the translation of the target relative to the radar produces a phase change on the response coming from the target. This translation is caused by the movement of the platform that contains the SAR system. One basic interpretation is the synthesis of a longer aperture compared with the real one, achieving a better resolution, which is just limited by the total antenna length (see section 2.1.3). The final SAR image is obtained through a proper processing of the phases and magnitudes of the multiple successive received echoes.

2.1.1 SAR Geometry

This section defines the geometric parameters involved in the SAR acquisition procedure, which are of great interest to better understand the SAR image formation.

Figure 2-1 illustrates the basic acquisition scheme of a SAR system [14]. Considering the satellite as the reference coordinate system, two main directions can be distinguished: *along-track* or azimuth direction, parallel to the platform displacement and the *across-track* direction or range direction, perpendicular to the platform movement. In the latter case we should distinguish between *slant-range* (line of sight between the sensor and the target) and its projection on the earth's surface, *ground-range*.

[1] Coherent systems preserve the phase and magnitude information of the signals.
[2] Direction parallel to the platform movement.
[3] Approximated as the ratio between the electrical length (wavelength λ) and the antenna length λ/L_a .

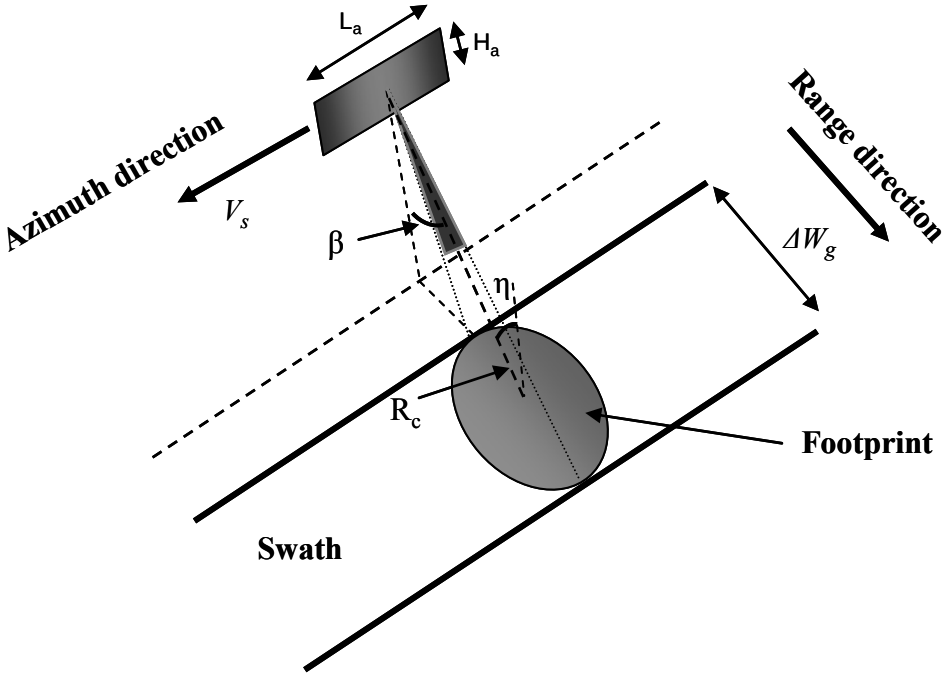

Figure 2-1: SAR geometry acquisition.

The configuration here presented is the standard *stripmap* mode [14], where the SAR sensor (fixed) moves in an approximate linear azimuth direction with constant velocity V_s. It is assumed that the radar beam is pointed perpendicular to the flight direction. The tilt β, indicates the angle between *broadside* of the antenna (pointing at the center of the footprint) and nadir[4]. In case of assuming a flat Earth surface the tilt angle and the local incidence angle η[5] are the same.

As the satellite is displacing along-track, transmits pulses with certain periodicity, so called Pulse Repetition Frequency (PRF). Each pulse is reflected by a terrain portion (footprint), illuminated by the antenna's pattern and the radar collects the different echoes. The ground extension of the radar beam is known as swath width, ΔW_g.

[4] Direction pointing below and perpendicular to the satellite.
[5] Angle between the *slant-range* direction of the observed target and the local normal to the earth's surface on the position of the target.

2.1.2 Range resolution

The (slant) range resolution δ_{sr} is defined as the minimum distance in range between two targets such that the SAR system is able to resolve both. In the case of conventional transmitted pulses the range resolution is determined by the pulse duration T as:

$$\delta_{sr} = \frac{c_0 \cdot T}{2} = \frac{c_0}{2 \cdot BW} \tag{2.2}$$

where BW is the signal bandwidth (inversely proportional to T) and c_0 the speed of light ($= 2.998x10^8$ m/s). Then, higher resolutions are obtained through shorter pulses. However, this implies higher peak power requirements.

The solution is provided by the so called *pulse compression* techniques [13]. In this case the peak power is reduced using longer modulated pulses and their compression through a matched filter allows obtaining higher resolution (shorter pulses). SAR systems use a linear frequency modulated (FM) pulses or *chirps*. These kinds of pulses have a linear variation of the instantaneous frequency within the pulse duration T as indicated in Figure 2-2[6]. The baseband expression of the chirp pulse is:

$$s_T(t) = rect\left(\frac{t}{T}\right)\exp\left\{j\pi\kappa_r t^2\right\} \tag{2.3}$$

where T is the pulse duration; κ_r chirp rate $\left[Hz/s\right]$ and t is the so-called *fast time* (range time). The frequency excursion within T generates the transmitted bandwidth of the signal, $BW = \kappa_r \cdot T$.

In order to obtain the desired range resolution, the received echo $r_T(t)$ is compressed through a matched filter to the transmit signal, $s_T^*(-t)$:

$$g_T(t) = r_T(t) * s_T^*(-t) \tag{2.4}$$

where the convolution operator is $*$ and $(\cdot)^*$ indicates conjugate.

The response $g_T(t)$ for the case of a single point target results in a *sinc*-like short pulse, whose mainlobe width determines the (slant) range resolution as:

$$\delta_{sr} = \frac{c_0}{2 \cdot BW} = \frac{c_0}{2 \cdot \kappa_r \cdot T} \tag{2.5}$$

[6] The values presented in figure are orientating values just to show the form of the chirp pulses.

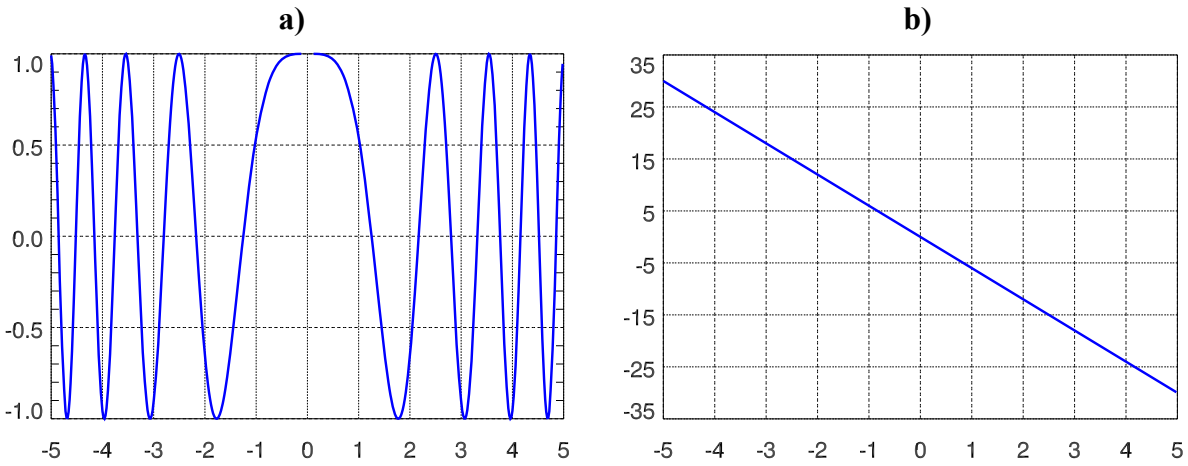

Figure 2-2: Chirp pulse **a)** complex amplitude and **b)** instantaneous frequency.

2.1.3 Azimuth resolution

In SAR systems the azimuth resolution δ_{az} is improved thanks to the synthesis of a large aperture. As the platform is moving, the SAR sensor transmits a pulse each PRF. Therefore, a sequence of sampled echoes at different positions of the platform trajectory is available, generating a larger "virtual" aperture. The time during which the target is illuminated by the azimuth's beam of the real antenna determines the extension of this synthetic aperture. As indicated in Figure 2-3, this temporal extension is called illumination time T_{ia} and can be expressed as:

$$T_{ia} = \frac{\Delta\Omega_{az} \cdot R_0}{V_s} = \frac{\lambda \cdot R_0}{L_a \cdot V_s} \tag{2.6}$$

where $\Delta\Omega_{az}$ corresponds to the azimuth antenna's beamwidth and R_0 the closest slant range approach to the target.

The extension of the *synthetic aperture* is directly related to the length of the trajectory described by the platform during the illumination time T_{ia} :

$$L_{sa} = 2 \cdot V_s \cdot T_{ia} = \frac{2 \cdot R_0 \cdot \lambda}{L_a} \tag{2.7}$$

where the factor 2 results from the two-way travel inherent in an active system.

Analog to the case of RAR, the azimuth resolution for SAR is limited in this case by the length of the synthetic aperture [14]:

$$\delta_{az} = \frac{\lambda}{L_{sa}} \cdot R_0 = \frac{L_a}{2} \tag{2.8}$$

From Eq. (2.8), the best azimuth resolution is constrained by the total length of the real antenna and is independent on the range distance of the target and the wavelength, contrary to the case of conventional RAR.

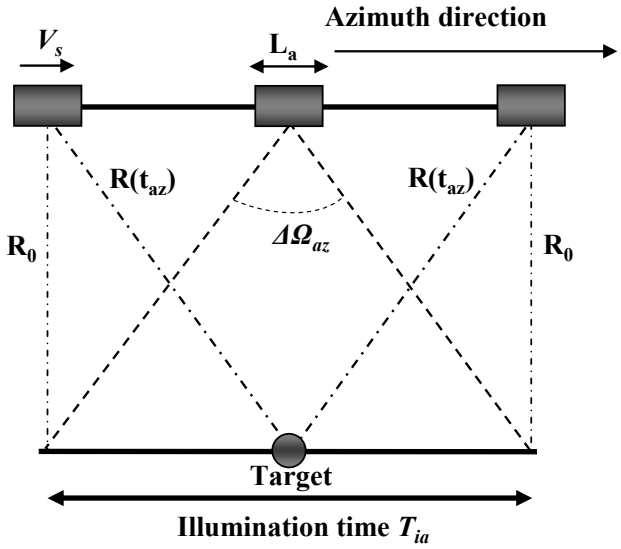

Figure 2-3: Azimuth acquisition geometry (synthetic aperture).

2.1.4 Range Cell Migration

As the platform is moving, the time delay of the received echoes from the target is changing for each azimuth position. Thus, the range $R(t_{az})$ to the target varies during the illumination time (Figure 2-3), where t_{az} is the azimuth time or *slow-time*. This phenomenon is called *Range Cell Migration* (RCM) and creates a frequency modulation (FM) characteristic on the signal in the azimuth direction, analog to the range chirp [13]. In order to capture all the signal energy, for the associated *azimuth compression*, it must be aligned in a single range cell or bin, whose range dimension is equal to the range resolution.

Figure 2-4 illustrates the range variation for a point target during the illumination time. This variation can be approximated by a parabolic function of the azimuth time t_{az}. To perform the range cell migration correction (RCMC) it is necessary to determine the total RCM, i.e. the maximum variation of the range $R(t_{az})$ respect to the closest approach R_0 within the target exposure (T_{ia}).

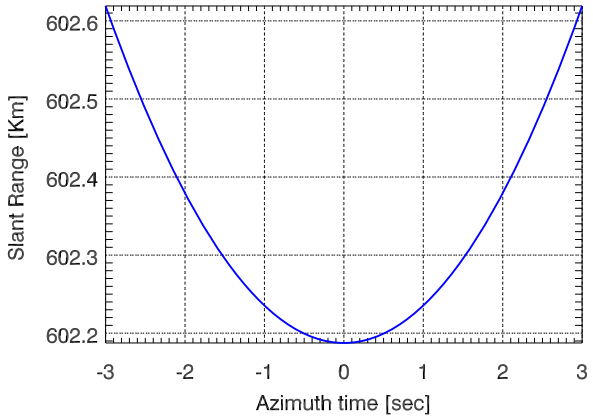

Figure 2-4: Range cell migration effect.

2.1.5 SAR processing

The objective of the SAR sensors is to provide a final image of the observed area, which can be easily interpreted. Then, the *raw* data (at the output of the sensor) should be processed to obtain a focused image. A two dimensional compression processing is performed in order to focus the spread signal over range and azimuth.

The *raw* image is formed by two different sweeps: samples of the chirp pulse along range and the azimuth samples with a PRF sampling frequency. Taking into account that the range to the target could be considered constant during the time of one pulse duration ($V_s \ll c_0$), the two-dimensional compression is decoupled into a sequence of two one-dimensional operations: one in the fast-time, propagation of the chirp pulse, and the other in the slow-time, displacement of the platform in the azimuth direction.

According to [13], the conventional standard processing sequence of the raw SAR consists on: first, the range compression is performed by a matched filter to the transmitted chirp pulse. This operation is implemented in the frequency domain via the Fast Fourier Transform (FFT) of each range line. The collection of this range-compressed data over the slow time constitutes the input for azimuth compression. However, these data is affected by RCM. The RCMC is applied in the azimuth frequency domain. Afterwards, the azimuth compression is performed, leading to the final focused SAR image.

2.1.6 Speckle noise

The quality of the final SAR images is affected by the so called speckle noise. This phenomenon can be explained due to the extended character of the natural targets within a resolution cell[7]. In SAR systems, the size of this cell or pixel ($1-100$ m) is bigger than the wavelength of the radar signal (e.g. 30 cm for an X-Band sensor).Then, within a resolution cell exist the contribution of several dispersive scatterers [14]. Therefore, the measured backscattering is a coherent superposition of the different responses of these scatterers.

Speckle is a multiplicative noise because its effect can not be attenuated increasing the transmit power. The extended characteristic of the sources is modeled by a complex valued correlated stochastic Gaussian process. The Gaussian attribute of the speckle can be justified by the *central limit theorem* when the resolution cell is conformed by a high number of scatterers and no one of them has a dominant effect over the others, i.e. homogenous extended sources [2]. Under these conditions the extended scatterers fit the classical *Swerling I* model [22], where the amplitude of the speckle is *Rayleigh* distributed and the phase has a *Uniform* statistic within $[0, 2\pi)$. Then, the pixels representing homogeneous backscattering surface do not present constant intensity.

[7] Cell or pixel of dimensions equal to the range δ_{sr} and azimuth δ_{az} resolutions.

2.1.7 SAR design and ambiguities

The design procedure in SAR systems implies the existence of a great number of interrelationships between user performance specifications (resolution, swath width, level of Signal-to-Noise Ratio), radar system parameters (system Gains, stability,..) and the available resources (payload mass, power and dimensions, platform altitude,…).

In the following, it is discussed the SAR design that contemplates the best possible resolution δ_{az} and the widest swath ΔW_g. This procedure leads to the classical minimum antenna area constrain [17]. It is precisely this restriction the one that has motivated the study of new SAR concepts as high-resolution wide-swath systems presented in section 2.2.

2.1.7.1 Minimum antenna area constrain

The classical SAR design goals are limited by contradictory requirements: achieve the best possible resolution with the widest swath [14],[35]. To better understand this trade-off it is considered the following geometry in the vertical plane, where a flat earth model is assumed.

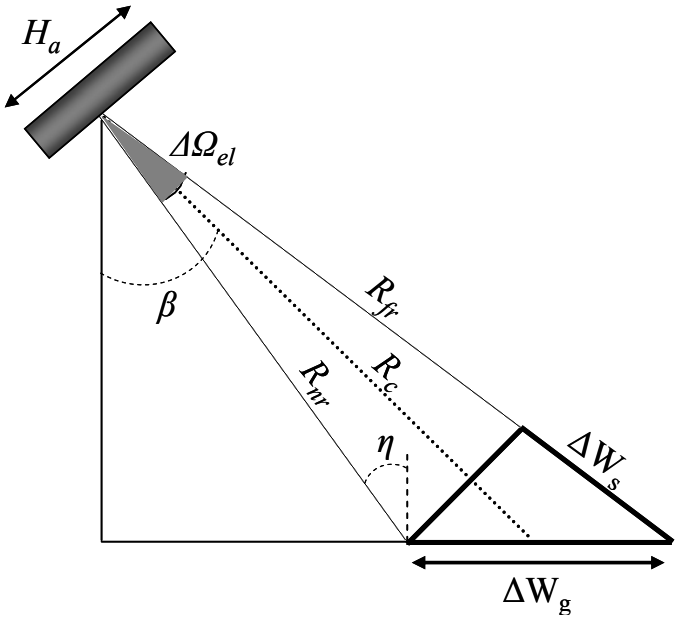

Figure 2-5: SAR geometry in the vertical plane.

From the figure above, the antenna's elevation beamwidth determines the maximum illuminated swath width on the ground (ΔW_g):

$$\Delta W_g = \frac{\Delta W_s}{\sin(\eta)} = \frac{\Delta\Omega_{el} \cdot R_c}{\cos(\eta)} = \frac{\lambda \cdot R_c}{H_a \cdot \cos(\eta)} \tag{2.9}$$

where ΔW_s is the swath width in slant range; $\Delta\Omega_{el}$ antenna elevation beamwidth; R_c is the (slant) range distance from the sensor to the center of the swath; H_a antenna height and η the local incidence angle, which is the same as the pointing angle of the beam β (centre of swath).

Ambiguous returns from both range and azimuth dimensions exist. Range ambiguities result from preceding and succeeding echoes arriving at the antenna simultaneously with the echo of interest [14]. Thus, a basic requirement is: the difference in the reception time between farthest point in the swath (far-range R_{fr}) and the nearest point (near-range R_{nr}) has to be smaller than the pulse repetition period (inverse of the PRF):

$$2 \cdot \frac{R_{fr}}{c_0} - 2 \cdot \frac{R_{nr}}{c_0} < \frac{1}{PRF} \tag{2.10}$$

From Figure 2-5 the prior constrain can be rewritten as:

$$\Delta W_s < \frac{c_0}{2 \cdot PRF} \tag{2.11}$$

The *azimuth ambiguities* appear in the image due to the discrete sampling of the azimuth or Doppler spectrum [14]. The received echoes are acquired each PRF. Thus, in order to avoid aliasing and taking into account the *Nyquist Sampling Theorem*, a lower bound on the PRF should exist:

$$PRF > \frac{2 \cdot V_s}{L_a} = \frac{V_s}{\delta_{az}} \tag{2.12}$$

where δ_{az} is the best possible azimuth resolution.

The combination of the two previous requirements to avoid ambiguities yields to the classical SAR trade-off, i.e. better azimuth resolutions are obtained at expenses of narrower swath width and vice versa:

$$\frac{\Delta W_s}{\delta_{az}} < \frac{c_0}{2 \cdot V_s} \tag{2.13}$$

From Eqs. (2.8) and (2.9), Eq. (2.13) can be reformulated into the minimum antenna area constrain [17]:

$$A_a = L_a \cdot H_a > \frac{4 \cdot V_s \cdot \lambda \cdot R_c}{c_0} \cdot \tan(\eta) \tag{2.14}$$

Equation (2.14) shows the main limitation of a conventional SAR, where swath width ΔW_g and azimuth resolution δ_{az} are contradicting requirements and can not be improved simultaneously. The antenna area constrain is especially important in the case of spaceborne systems, where the platform velocity V_s and the slant range distance R_c are order of magnitude higher than in the airborne case.

2.2 High Resolution Wide Swath technique

2.2.1 Introduction

From the previous section, the conventional SAR systems suffer from a clear restriction when trying to obtain a wide unambiguous swath coverage ΔW_g and high resolution δ_{az}. This situation led to the development of advanced SAR imaging modes with different tradeoffs between spatial coverage and resolution.

The *ScanSAR* mode is the classical solution to obtain an improved swath coverage but with a degradation on the azimuth resolution [49]. On the other hand, many remote sensing applications require SAR images with high spatial resolution (surveillance, cartographic mapping, hazard assessment…). Then, it was proposed a new operational mode, *Spotlight*, which improves the azimuth resolution at expenses of non-continuous coverage along the satellite track [11]. Nevertheless, remote sensing applications demand and will demand SAR products that combine the excellences of both modes of operation, high-resolution and wide-coverage. This has motivated an intensive research on new radar concepts based on Smart Multi-Aperture Radar Technique (SMART) [32],[55].

These SMART SAR systems combine the potentiality of the smart antennas (multiple transmit/receive channels) with new digital signal processing techniques, such as Digital Beam-Forming (DBF), in the conventional SAR systems [19],[32],[55].

A relaxation of the SAR system design constrains can be achieved through the increase on the degrees of freedom obtained by the use of Smart antennas. This is directly translated into a lower ambiguity level, higher Signal-to-Noise Ratio (SNR), improved radiometric resolution, and a reduction of the trade-off between spatial coverage (swath width) and resolution.

HRWS SAR, proposed by *Suess et al.* in [45] and [46], is a novel SAR system, which relies on the mentioned SMART concept. This new system combines the flexibility offered by a multi-channel architecture with a limited download data volume to provide a high azimuth resolution with an improved swath width and a continuous coverage in Stripmap mode. The HRWS SAR system is based on a DBF processing algorithm for steering of the elevation beam pattern, called SCORE. In the following it is described the concepts behind this novel system.

2.2.2 HRWS concept

The HRWS SAR system uses the concept of bistatic formation: separated apertures for transmit (TX) and receive (RX)[8]. The latter one is split in several sub-apertures or channels both in elevation (K) and azimuth (M), see instrument configuration in Figure 2-6.

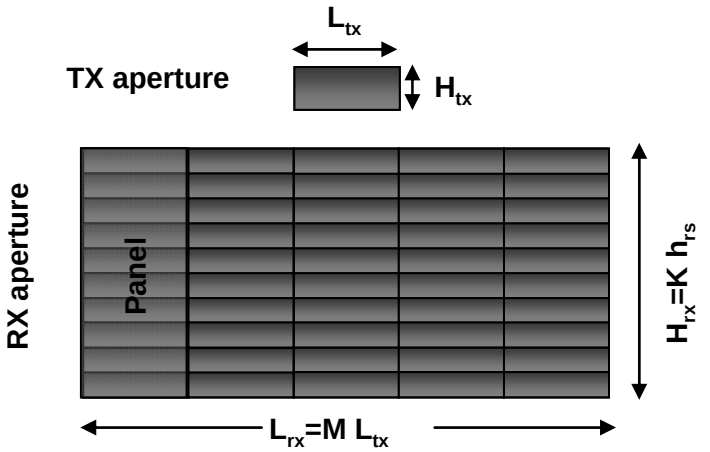

Figure 2-6: HRWS SAR architecture, Transmit (TX) and receive (RX) apertures.

From Eq. (2.9), the size of the transmit antenna determines the illuminated area, where the final swath image is inversely proportional to the height of the transmit aperture H_{tx}. To obtain a wider swath, the elevation dimension of the transmit aperture H_{tx} must be smaller than in a conventional SAR, where the same antenna is used to transmit and receive.

As in the case of classical SAR, the azimuth dimension of the transmit antenna L_{tx} determines the achievable azimuth resolution Eq. (2.8). Therefore, resolution and swath width of the bistatic system are related to the dimensions of the transmit antenna (H_{tx} and L_{tx}) and can be improved using a smaller transmit aperture.

A smaller height of the transmit antenna H_{tx}, under the same conditions as classical SAR, implies a reduction on the radiometric resolution, i.e. SNR. Thus, in order to compensate this gain loss, the height of the receiving aperture H_{rx} is larger than in a conventional SAR system. Then, the receive antenna is formed by K sub-apertures in elevation, each of them has to cover the area (swath) illuminated by the transmit aperture. Thus, the height of each receive sub-aperture h_{rs} should be smaller or equal to the elevation dimension of the transmit antenna H_{tx}. The proper combination of the signals from the different channels is performed through a DBF technique called SCan-On-REceive, later presented.

[8] The TX and RX apertures can be mounted in the same satellite or different satellites in the same constellation.

The achievable swath width ΔW_s is limited by the range ambiguities, see Eq. (2.11). One way to reduce these ambiguities is increasing the distance between subsequent transmitted pulses and so reducing the PRF. However, from Eq. (2.12), there exists a lower bound on the PRF in order to sample correctly the azimuth spectrum and reduce the azimuth ambiguities.

This conflict of the classical SAR systems is overcome in the HRWS configuration using M receive sub-apertures or panels in azimuth (Figure 2-6). This approach is known as displaced phase center antenna (DPCA) for receive in a way that the radar echo is sampled at M different positions simultaneously [15],[48]. Therefore, the PRF can be adjusted for a correct sampling taking into account the total length of the receive antenna L_{rx} instead of the sub-aperture length L_{tx} [9]. Thus, the effective PRF can be reduced by a factor of M and the swath width could be increased up to the same order depending on the desired geometric resolution [48].

[9] The RX sub-aperture length L_{rx} matches the TX antenna length L_{tx}

2.3 SCan-On-REceive

2.3.1 Introduction

In a conventional SAR an increase of the total height of the receive aperture beyond a certain point results not to be effective as the beamwidth should be kept wide enough to cover the swath. Based on this previous statement, the HRWS has to properly combine the signals from the different sub-apertures through a DBF technique called SCan-On-REceive (SCORE).

The idea of SCORE is to shape a time varying elevation beam in reception such that it follows the echo of the pulse on the ground. This approach was first suggested by *Blythe* [4] in 1981, as the necessity to improve the performance in SAR systems and reduce the system design constrains. Twenty years later, two independent works by *Kare* [31] and *Suess* [45],[46] give a more detailed insight into this approach.

In [31], *Kare* presents the *Moving Receive Beam* technique in order to improve the resolution of the conventional SAR systems over a wider coverage area, with a primary objective: reduction of the edge losses[10] and the range ambiguities. An important observation made in this work is the necessity to take into account the temporal extension of the pulses, in particular, long chirp pulses. In this case the time-frequency characteristic of this kind of pulses (section 2.1.2) implies that the time varying steering is also frequency dependent. Therefore, it is suggested that the position of the beam has to be adapted to the frequency of the received echo.

In [45] and [46], *Suess* presents the SCORE technique to be combined with the DPCA in the so called *HRWS SAR* system. In that work it is suggested a real time Digital Beam-Forming technique to process the signals received at the different sub-apertures in elevation, which yields to a sharp receive beam. As it is depicted in Figure 2-7, the multiple beam-forming process results in narrow beams steered electronically in elevation within the swath illuminated by the transmit antenna, in a way that the reflection of the pulse is followed with the maximum gain of the receive pattern.

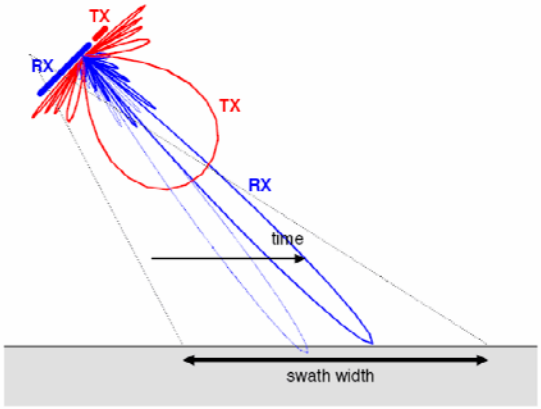

Figure 2-7: SCORE technique.

[10] Edge losses are defined as the reduction in performance at the edge of the useful portion of the radar beam compared to the performance at the center of the beam (both on transmission and reception).

2.3.2 SCORE operation

The objective of SCORE algorithm is to acquire the echoes backscattered from the swath with the maximum gain by an electronic scansion of the beam achieved through a digital processing of the signals from the different sub-apertures. This approach is included in the concept of DBF applied to SAR systems, which constitutes an active research area [19],[32],[54],[55]. In contrast to analog beam-forming, the received signals of each sub-aperture are separately amplified, down-converted, and digitized through Analog to Digital Converters (ADC). This allows *a posteriori* combination of those signals to form multiple beams.

The steering direction of SCORE $\theta_s(t)$, measured w.r.t. nadir, corresponds to the expected DOA of the echo $\theta(t)$, which is assumed a *priori* known. In particular, in [46] and [48], the echo DOA is computed based on the vertical slant-range plane acquisition geometry, considering a spherical Earth model with no topographic profile (see Figure 2-8). Under this assumption the echo's DOA from a point target is univocally associated with the two-way time delay t:

$$\theta_s(t) = \arccos\left(\frac{\left(H_{orb} + R_E\right)^2 - R_E^2 + R^2(t)}{2 \cdot \left(H_{orb} + R_E\right) \cdot R(t)} \right) \tag{2.15}$$

where H_{orb} is the orbit's height, R_E the Earth radius and $R(t)$ is the slant-range distance to the point-target.

From Eq. (2.15), there is a one-to-one relation between the required beam steering angle $\theta_s(t)$ and the time variable t. Therefore, the scansion of the beam is performed within the temporal window of the received echo. The extension of this window is limited by the time delays at the edges of the swath and the chirp pulse duration T as:

$$t_{nr} - \frac{T}{2} \le t \le t_{fr} + \frac{T}{2} \tag{2.16}$$

where t_{nr} and t_{fr} are the two-way time delays when the center of the chirp reaches respectively the near and far edges of the swath (Figure 2-8).

The steering performed by SCORE allows producing a fast-time beam scan in order to ensure that the centre of the receive beam (with maximum gain) looks at the centre of the pulse. However, the whole footprint of the pulse on the ground cannot be completely covered by the beam because a long chirp pulse is used. This means that the echo instantaneous DOA is spread [46]. Nevertheless, the chirp pulse allows having a linear variation of the frequency with the time. In this way, each frequency on the pulse is directly related to a position on the earth surface and so to a specific DOA.

In this sense SCORE carries a fast-time scanning of the beam such that the center of the pulse (carrier frequency) is acquired with the maximum gain. An additional frequency dispersion of the beam is performed in a way that each frequency component of the pulse is pointed by its "own" beam.

A detailed description of the SCORE algorithm and possible technological implementation can be found in [48]. In the thesis, it is considered that the SCORE frequency dependent beam steering allows acquiring all the pulse energy with maximum gain, when the DOA of the pulse centre is recovered.

The high gain SCORE sharp beam, which follows the echo along the ground, allows obtaining an increased SNR, compensating the low gain (wide beam) of the transmit antenna. Specifically, it mitigates the "edge losses", i.e. the typical two-way loss of the conventional SAR system at the extremes of the swath (half-power beamwidth angles).

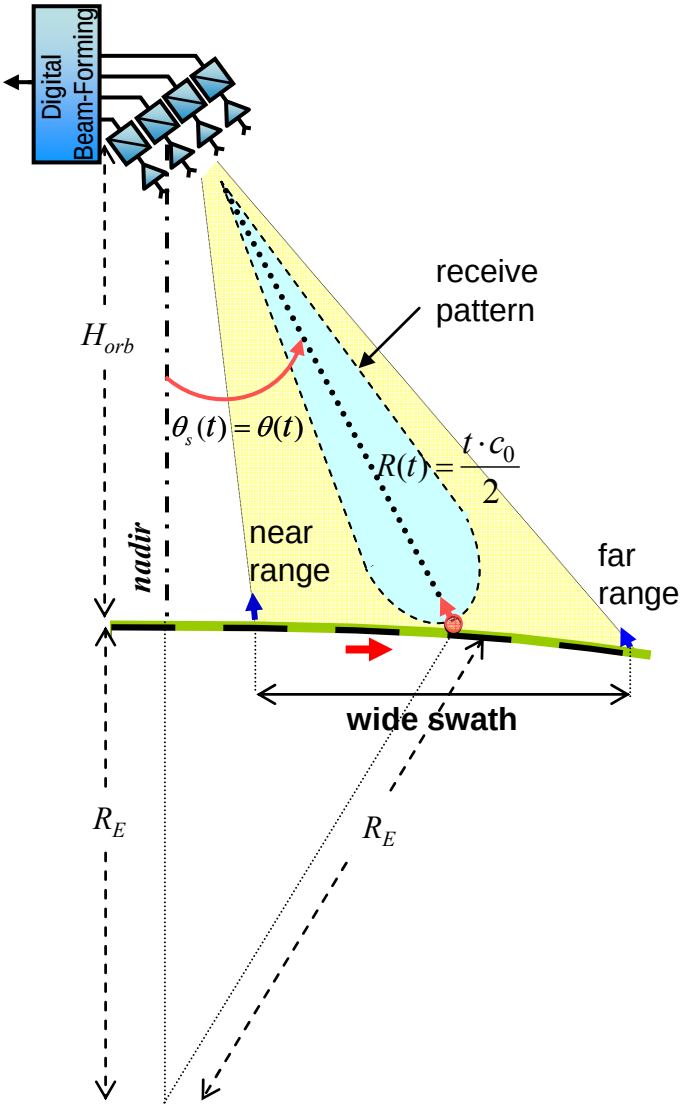

Figure 2-8: HRWS acquisition geometry in the vertical slant range plane (distances and angles not in scale).

2.3.3 SCORE limitation

In real acquisition scenarios with specific topographic profiles (mountains, relieves…), SCORE works under model mismatch (Figure 2-9). In these situations there exits an angular displacement between the DOA of the actual echo $\theta(t)$ and the steering direction $\theta_s(t)$ computed by SCORE:

$$\Delta\theta_s = \theta(t) - \theta_s(t) \tag{2.17}$$

This is directly translated into a performance loss as the echo impinging on the antenna is not weighted by the maximum of the receive beam. This degradation on SCORE can be quantified in terms of pattern loss (PL) as:

$$PL = \frac{C^R(\theta_s + \Delta\theta_s)}{C^R(\theta_s)} \tag{2.18}$$

where $C^R(\theta)$ indicates the value of the elevation receive beam pattern generated by DBF at the angle θ.

The impact of topographic height on SCORE performance was analyzed in [7]. For a realistic SAR system the angular displacement varies between 0.15º for $h = 1000\ m$ to 1.45º for $h = 8000\ m$ [11], which is typically translated into a pattern loss of several dBs, depending on the beam sharpness. SCORE steering mechanism neglects not only the effect of the actual acquisition geometry on the slant-range elevation plane, but also surface variations along the azimuth direction.

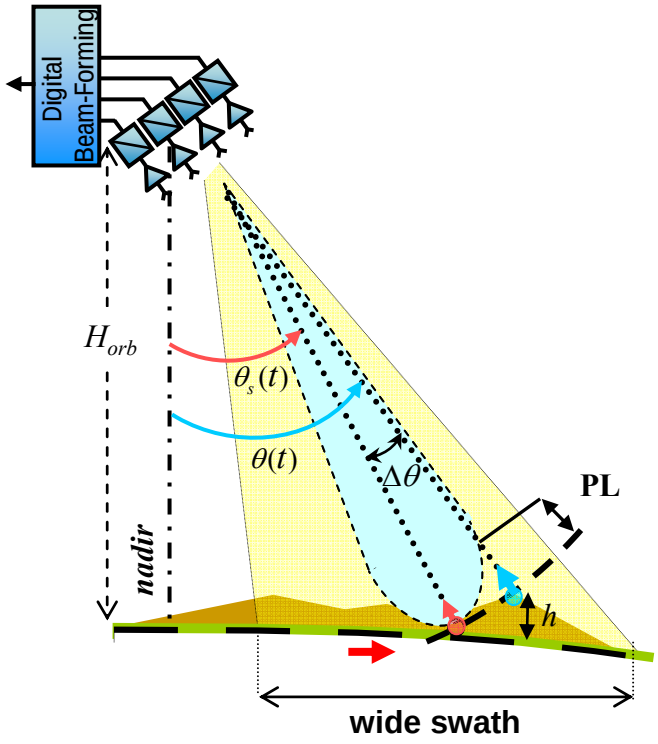

Figure 2-9: SCORE in presence of topographic height, h (not in scale).

[11] Topographic height corresponds to the elevation over the spherical Earth surface.

These observations suggest the option of an *adaptive* approach, i.e. adaptively steer the beam towards an *estimate* of the actual DOA by processing the signals available form the sub-apertures in elevation. The multi-channel receive antenna provides a spatial sampling of the signal, which can be used to evaluate the distribution of the received power as a function of the spatial location or DOA. In this sense, the receive beam direction would be selected as the one associated with the strongest signal level in a certain DOA.

The objective of the thesis is to present and evaluate this new adaptive algorithm to steer the beam according to the actual spatial distribution of the received power. This alternative approach is cast in the field of *spatial spectral estimation* and *DOA estimation*. In the next chapter the basics behind the DOA estimation problem are presented to further introduce the implementation of the ADBF in Chapter 4.

Chapter 3 Direction of Arrival estimation

The adaptive method requires the estimation of the DOA based on the proper processing of the signals impinging in a multi-channel antenna, also named as array of sensors. In the first part of the chapter, array processing is linked to the DOA parameter estimation through the signal model characterization, including both *narrowband* and *wideband* assumptions. Then, a brief review of the actual framework on the DOA estimation problem is provided. This allows to better understand whether there is a solution that can fulfill the specific requirements of the adaptive implementation in the SAR field.

3.1 Array processing and DOA estimation

The problem of DOA estimation is based on the location of N_s radiating sources through an array of sensors[12], which basically consists of K sensors, distributed in the space. Then, the corresponding impinging signals are sampled both temporally and spatially by the sensors array.

This additional spatial diversity is used to determine the distribution of power over the space, where the sources' DOAs (locations) represent points with high concentration of power. Thus, the DOA estimation is turned into a spatial spectral estimation problem. Then, it is required a proper formulation of the signal at the output of the array. In the following the general data model is presented, based on the analysis made by *Stoica* and *Moses* in [44].

The next hypotheses are considered: the wave fields of the impinging signals are *plane waves*, i.e. the sources are located in the far-field. This assumption is valid since the distance between the sources of interest and the array is large compared with the array itself. The sources are *point emitters*, i.e. non-spatially spread. The sensors are modeled as linear elements with known impulse response and locations, i.e. *calibrated*.

Then, the complex valued signal at the output of the $k-th$ element for a single source can be expressed as:

$$y_k(t) = h_k(t) * x(t - \tau_0 - \Delta\tau_k) + e_k(t) \tag{3.1}$$

where $*$ is the linear convolution; $h_k(t)$ the response of the $k-th$ sensor; $x(t)$ is the source signal; τ_0 the time-delay measured at a *reference point*[13]; $\Delta\tau_k$ the time delay between the reference point and the $k-th$ sensor and $e_k(t)$ is the additive thermal noise at the $k-th$ sensor.

From Eq. (3.1), the signal $x(t)$ received at the $k-th$ sensor has an additional time delay $\Delta\tau_k$ respect to the reference phase centre. This difference in time delay depends on the position of the sensor on the array and the space location of the source. Then, the DOA estimation problem relays on a differential measure of the time delay between the sensors, which is independent on the absolute (common) time τ_0. This information can be extracted through the correlation between the different sensors, grouped in the so called KxK covariance matrix $\mathbf{R}_\mathbf{y}$ with elements:

$$\left[\mathbf{R}_\mathbf{y}\right]_{k,l} = E\left\{y_k(t) \cdot y_l^*(t)\right\}, \quad k,l = 1,\ldots,K \tag{3.2}$$

where $E\{\cdot\}$ indicates the statistical expectation and $(\cdot)^*$ conjugate operator. The Fourier Transform (FT) of these correlation sequences is the spatial *power spectral density* (PSD) of the output signal. Thus, DOA estimation can be traced to the problem of estimating the spatial PSD.

[12] The term sensor is used in signal array processing and is completely analog to element, channel or sub-aperture used in the different chapters along the thesis.

[13] Represents a time/phase reference and can be located at any physical point of the array, e.g. sensor phase center.

3.2 Signal model

Assume that $x(t)$ is a bandpass signal obtained by the complex modulation of the baseband signal $s(t)$ at ω_c. Then, the frequency domain representation of the signal in Eq. (3.1) is:

$$Y_k(\omega) = H_k(\omega)\cdot\left[S(\omega-\omega_c)+S^*(-\omega-\omega_c)\right]\cdot\exp\{-j\omega\cdot(\tau_0+\Delta\tau_k)\}+E_k(\omega) \quad (3.3)$$

where $H_k(\omega)$, $S(\omega)$ and $E_k(\omega)$ correspond respectively to the Fourier Transform of $h_k(t)$, $s(t)$ and $e_k(t)$; $(\cdot)^*$ indicates conjugate; $\omega = 2\pi f$ is the radian frequency [rads/s] and ω_c the carrier frequency.

After demodulation and lowpass filtering, matched to the bandwidth of $s(t)$, Eq. (3.3) is expressed as:

$$Y_k(\omega) \approx H_k(\omega_c)\cdot S(\omega)\cdot\exp\left\{-j\omega_c\cdot\left(1+\omega/\omega_c\right)\cdot(\tau_0+\Delta\tau_k)\right\}+E_k(\omega+\omega_c) \quad (3.4)$$

where it is assumed that the response of the sensor $H_k(\omega)$ is constant over the signal bandwidth Ω; while for the thermal noise, this hypothesis might not be true and $E_k(\omega+\omega_c)$ corresponds to the part of the noise, after demodulation, that fall within the signal bandwidth.

3.2.1.1 Narrowband signals

For narrowband sources, the fractional bandwidth is much smaller than the unit, i.e. $\Omega/\omega_c \ll 1$. Then, Eq. (3.4) can be rewritten as in Eq. (3.5), where the time delay has been converted into a phase term, decoupling temporal and spatial information of the source.

$$y_k(t) = H_k(\omega_c)\cdot s(t)\cdot\exp\{-j\omega_c\cdot\Delta\tau_k\}+e_k(t), \quad (3.5)$$

where, without loss of generality, the phase corresponding to the common time delay τ_0 has been included in the signal $s(t)$.

Then, it is defined the *K*-dimensional *array steering vector*:

$$\mathbf{a}(\theta) = \left[H_1(\omega_c)\cdot e^{-j\omega\cdot\Delta\tau_1} \quad \cdots \quad H_K(\omega_c)\cdot e^{-j\omega\cdot\Delta\tau_K}\right]^T \quad (3.6)$$

such that θ indicates the source DOA, and $(\cdot)^T$ is the transpose operator.

Using vector notation, the sampled version of $y_k(t)$ is given by:

$$\mathbf{y}(t) = \mathbf{a}(\theta)s(t)+\mathbf{e}(t), \qquad t = 1,...,N \quad (3.7)$$

where $\mathbf{y}(t)$, $\mathbf{a}(\theta)$ and $\mathbf{e}(t)$ are *K*-dimensional column vectors; t indicates a time-discrete variable and N the total number of samples of $\mathbf{y}(t)$.

Assuming that the responses of the different sensors are *omnidirectional*, i.e. independent on θ, *identical* and the first sensor ($k=1$) as the phase reference, the steering vector is reformulated like:

$$\mathbf{a}(\theta)=\begin{bmatrix}1 & \cdots & e^{-j\omega\Delta\tau_K}\end{bmatrix}^T \tag{3.8}$$

The data model in Eq. (3.7) can be generalized to N_s sources in far-field:

$$\mathbf{y}(t)=\sum_{i=1}^{N_s}\mathbf{a}(\theta_i)\cdot s_i(t)+\mathbf{e}(t)=\mathbf{A}\cdot\mathbf{s}(t)+\mathbf{e}(t),\qquad t=1,...,N \tag{3.9}$$

where θ_i denotes the DOA associated to the $i-th$ source; the KxN_s matrix $\mathbf{A}$ is the *steering matrix*, whose columns are $\{\mathbf{a}(\theta_i)\}_{i=1}^{N_s}$ and the source signals are grouped in the N_s-dimensional column vector $\mathbf{s}(t)$.

Figure 3-1, illustrates the uniform linear array configuration (ULA) used along the thesis. Then, for the $i-th$ source, the time delay $\Delta\tau_{i,k}$ between the reference phase center ($k=1$) and the $k-th$, under the assumption of plane wave, is expressed as:

$$\Delta\tau_{i,k}=\frac{(k-1)\cdot d\cdot\sin(\beta-\theta_i)}{c_0},\quad k=1,\ldots,K \tag{3.10}$$

with d inter-element spacing between two consecutive phase centers; β tilt angle of the antenna and θ_i the DOA of the $i-th$ source (both angles measured respect to nadir).

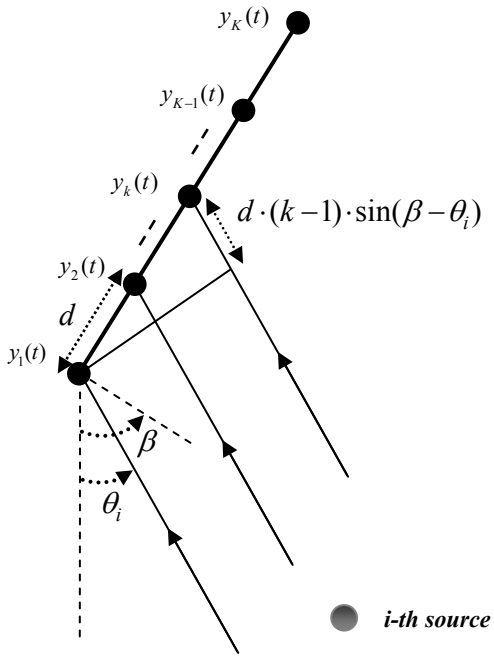

Figure 3-1: Geometry of a ULA array of sensors (phase center representation)

3.2.1.2 Wideband signals

In case of wideband signals, the term ω/ω_c in Eq. (3.4) can not be neglected since the bandwidth is in the order of the carrier frequency. Then, additional to the spatial diversity, frequency diversity should be also taken into account. This means that the steering vectors that contain the information regarding the DOA are frequency dependent. Analogy to the data model in Eq. (3.9), the sensor output can be expressed in the temporal frequency domain as frequency dependent narrowband signals, also called frequency domain snapshot model (pp. 334-349, [50]).

$$\mathbf{Y}(\omega) = \mathbf{A}(\omega, \boldsymbol{\theta}) \cdot \mathbf{S}(\omega) + \mathbf{E}(\omega) \tag{3.11}$$

where $\mathbf{Y}(\omega)$, $\mathbf{S}(\omega)$ and $\mathbf{E}(\omega)$ are the FT of $\mathbf{y}(t)$, $\mathbf{s}(t)$ and $\mathbf{e}(t)$, respectively.

Then, the wideband DOA estimation can be interpreted as a collection of narrowband problems. This decomposition is achieved through a filter bank approach or using the Fast Fourier Transform (FFT) over a time segment of the data at the different channels[14]. Thus, additional complexity and computational effort is required compared to the case of narrowband signals, where it is exploited the fact that time delays between channels are just phase differences.

[14] In [24], it can be found a detailed description of the wideband snapshot model and the narrowband decomposition approach.

3.3 DOA estimation methods

It was necessary to search in the literature for an estimation method that can handle with the peculiarities/challenges of the multi-channel SAR scenario:

- The processing should be performed on-board in order to reduce the data volume in the downlink.
- Radar signals are wideband chirp pulses (section 2.1.2).
- Chirped radar systems have a spread of the instantaneous echo direction due to long pulse durations [48]: each position within the ground extension of the pulse (≈ 45 km $- 17$ km)[15] is associated to a different direction (DOA spread $\approx 4.4^{\circ} - 0.6^{\circ}$) and to a different frequency component due to the linear time-frequency structure of the chirp pulses.
- In the wide illuminated swaths, the useful signal could be super-imposed to range-ambiguous returns with the same power (multi-source scenario).

Based on the data model, the different estimation algorithms are primary grouped in two sets: *narrowband* and *wideband*.

- ***Narrowband estimation***

The narrowband estimation problem has been extensively studied in the literature [33],[44],[50]. Its potentiality is based on the simple implementation of estimation algorithms such as: classical space exploration techniques, e.g. Beamformer and Capon [44], or the well-known subspace method MUSIC (MUltiple SIgnal Classification)[16], which provides a high performance and relative low computational cost. These estimation methods have been successfully addressed also to multibaseline interferometric SAR (InSAR) [23]. However, they can not be directly applied to the specific scenario here considered since the SAR signals, i.e. wideband chirps, do not fit the narrowband model in Eq. (3.9).

- ***Wideband estimation***

The DOA estimation has application in many areas such as Radar and communications, where the involved signals are wideband. This has led to an exhaustive research for wideband estimation techniques. Table 3-1 summarizes the main characteristics and limitations of some of these methods.

Conventional approaches, *incoherent signal-subspace* (ISS) and *coherent signal-subspace* (CSS), extend the application of methods as MUSIC to wideband sources, dividing the band into narrowbands and then applying subspace processing to each one [51],[52].

[15] For a chirp pulse with duration $T = 95\ \mu s$ computed within swath of interest 300 km – 370 km [6].

[16] MUSIC is a superresolution method based on the eigendecomposition of the covariance matrix in two orthogonal subspaces [39].

These methods have limited application to chirp signals, because they do not exploit their time-frequency structure [21],[53]. Moreover, CSS is based on an iterative approach that requires initial estimates of the DOA, which can result critical to the performance and may imply additional on-board computational complexity.

Several approaches, as the iterative algorithm for wideband chirps by *Wang et al.* [53] and the *extended coherent signal-subspace* (ECSS) by *Gershman et al.* [20], take advantage of the time-frequency structure of the chirp signals. These procedures rely on the concept of Spatial Time-Frequency Distributions (STFD) that allows formulating efficient MUSIC-type techniques with improved performance (see [1] and references therein). The main drawback of the first approach is that the convergence of the iterative process is not guaranteed [20],[37]. Similar to the conventional CSS, the ECSS approach relies on initial estimates of the DOA and it suffers also from high computational cost [21].

An alternative approach, *chirp beamformer* was presented by *Gershman* in [21], which allows the estimation of chirp parameters, i.e. DOA, chirp rate and initial frequency. This method assumes a single source case and can be extended to multiple sources when one or more of the signal parameters are "well-separated". However, in the scenario here considered with possible range-ambiguous returns, the chirp rates of these signals and the one of interest are exactly the same.

Then, the actual wideband DOA estimation framework may not provide a suitable solution for the specific SAR scenario. Most of the analyzed wideband methods represent an additional computational effort to the processing that should be performed on-board. Moreover, the techniques based on extending the MUSIC subspace method to the wideband case, as ISS, CSS or ECSS, do not take into account the spread direction of the echo, i.e. each frequency component is associated to a different DOA. This situation suggests an alternative that could re-drive the DOA estimation over SAR signals to a narrowband estimation problem. In the next chapter this novel algorithm is presented.

Method	Description	Limitations	Ref.
Incoherent signal-subspace (ISS)	average estimates at different frequency components	degradation at low SNR not able handle correlated sources limited application to chirp signals	[51]
Coherent signal-subspace (CSS)	transform subspaces at different frequencies into a focused subspace and apply MUSIC to the average	require initial DOA estimates focusing matrix limit performance limited application to chirp signals	[52]
Iterative algorithm for wideband chirps	time-frequency analysis to estimate chirp rates and compensation of the chirp structure in an iterative manner	require initial DOA estimates convergence not guaranteed	[53]
Extended coherent signal-subspace (ECSS)	STFD formulation combined with CSS (averaging over time-frequency points, not only frequency points as in CSS)	require initial DOA estimates focusing matrix limit performance high computational cost	[20]
Chirp beamformer	approximate solution of log-likelihood function of single chirp signal	extended to multiple sources when DOA or chirp rates are "well-separated"	[21]

Table 3-1: Conventional and wideband chirp estimation methods.

Chapter 4 Adaptive Digital Beam-Forming

In this chapter the new steering algorithm, denoted as Adaptive Digital Beam-Forming (ADBF), is described. A pre-processing of the data is included in the algorithm, allowing to trace back the SAR signal to a model typically used in narrowband spectral estimation [44],[50] and in multibaseline Interferometric SAR [23]. Then, narrowband spectral estimation algorithms, such as Beamformer, Capon and MUSIC are presented. The last part of the chapter introduces the concept of unambiguous DOA range as well as the procedure used to detect and associate the DOA estimates to the true values.

4.1 Data pre-processing

As it has been discussed in the previous chapter, the wideband nature of the SAR signals does not allow a direct application of the narrowband estimation methods. On the other hand, the necessity to perform the processing on-board discards the high computational wideband approaches. This situation has motivated the alternative considered by the ADBF, where the narrowband DOA estimation is performed over a pre-processed data, see block diagram Figure 4-1.

The pre-processing step allows translating the DOA estimation of the impinging SAR echoes into the determination of the DOA corresponding to each sample of the range compressed signal, i.e. backscattered by the area at slant range distance R^{tx} and R_1^{rx} from the transmit and first receive sub-aperture, respectively. This area is delimited by the (slant) range resolution δ_{sr} (section 2.1.2) and the mainlobe aperture of the azimuth pattern. In the following, for simplicity, the pre-processing stage is described for a point-like target. Afterwards, Chapter 5 generalizes the model for extended sources.

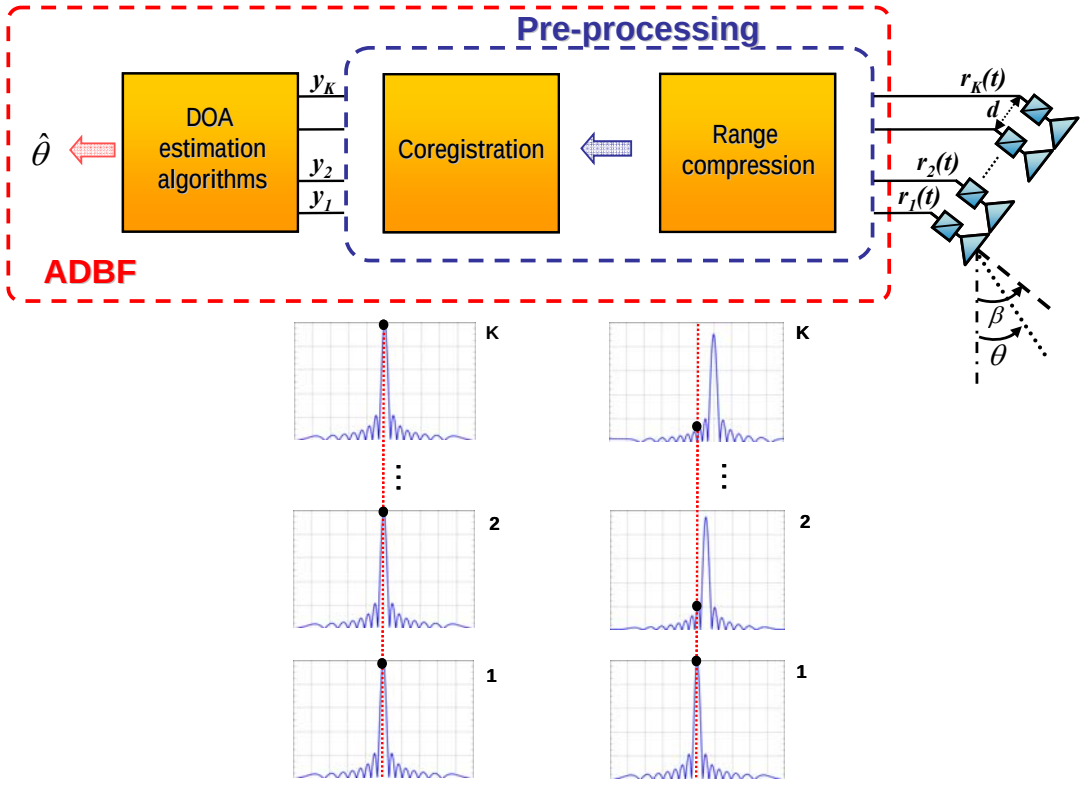

Figure 4-1: ADBF block diagram (point target analysis).

Assume that the transmitted SAR pulse is a chirp:

$$s(t) = rect\left[\frac{t}{T}\right] \cdot \exp\left\{ j \cdot (2\pi f_c t + \kappa_r \pi t^2) \right\} \tag{4.1}$$

where T is the pulse duration of the chirp, f_c the carrier frequency and κ_r chirp rate.

It is considered an antenna in elevation formed by K sub-apertures arranged according to a ULA and plane-wave assumption for the impinging signals. Then, the two-way time delay of the corresponding echo, received by the $k-th$ sub-aperture from a point target at R^{tx} and R_1^{rx}, has two different contributions:

$$\tau_k = \tau_0 + \frac{d \cdot (k-1) \cdot \sin(\beta - \theta)}{c_0}, \quad k = 1, ..., K \tag{4.2}$$

where τ_0 is the two-way time delay between the phase centre of the transmit antenna and the first receive sub-aperture, assumed as the phase reference, $\tau_0 = (R^{tx} + R_1^{rx})/c_0$. The second term in Eq. (4.2) refers to the time-difference between the first and the $k-th$ sub-aperture for a specific inter-element spacing d. This time-delay contains information regarding the spatial location of the target, where θ is the echo DOA and β the tilt angle of the receive antenna, both measured w.r.t. nadir.

After demodulation the equivalent baseband signal of the echo at the $k-th$ sub-aperture is written as:

$$r_k(t) = \gamma \cdot rect\left[\frac{t-\tau_k}{T}\right] \cdot \exp\left\{ j \cdot \kappa_r \cdot \pi (t-\tau_k)^2 - j \cdot 2\pi f_c \tau_k \right\}, \quad k = 1, \ldots, K \tag{4.3}$$

where γ is a complex amplitude that accounts for the propagation and backscattering mechanism. Note that from here on t indicates a discrete time variable.

After range compression with a matched filter to the transmit pulse, the signal at each sub-aperture is a short pulse centered at the respective time delay:

$$r_k(t) = \gamma \cdot \mathrm{sinc}\left\{ \kappa_r \cdot T \cdot \left(t - \tau_k\right) \right\} \cdot \exp\left\{ -j \cdot 2\pi f_c \tau_k \right\}, \quad k = 1, ..., K \tag{4.4}$$

The recorded samples from the different channels are located at different two-way time delays τ_k and so with different (slant) range distances to the target. It is worth noting that a coregistration process is necessary to ensure that the samples in each channel correspond to the same backscattering area.

The slant range difference between the sub-apertures has a linear evolution along the swath and is slightly affected by the topography (see Annex A.1). For the reference system, described in Table 7-1, this variation between the extreme sub-apertures is below 0.07 m, which is in the order of a tenth of the slant range resolution ($\delta_{sr} \approx 0.6$ m). Then, a registration process to the first sub-aperture can be used to reduce the mismatch until 1/30 of the range resolution [36].

Once the coregistration has been performed the signal at the different channels in elevation could be written as:

$$r_k(t) = \gamma \cdot \mathrm{sinc}\left\{\kappa_r \cdot T \cdot \left(t - \tau_0\right)\right\} \cdot \exp\left\{-j \cdot 2\pi f_c \tau_k\right\}, \quad k = 1,...,K \tag{4.5}$$

Then, the recorded sample corresponding to $t = \tau_0$ is:

$$r_k = \gamma \cdot \exp\left\{-j \cdot \frac{2\pi}{\lambda} \cdot d \cdot (k-1) \cdot \sin(\beta - \theta)\right\}, \quad k = 1,...,K \tag{4.6}$$

where λ is the radar wavelength, and without loss of generality, the phase term $\exp\left\{-j \cdot 2\pi f_c \tau_0\right\}$, associated to the common two-way time delay τ_0, has been included in the complex constant γ.

At this point Eq. (4.6) can be expressed using vector notation, taking into account the presence of an additive thermal noise, which corrupts the useful signal:

$$\mathbf{y} = \gamma \cdot \mathbf{a}(\theta) + \mathbf{e} \tag{4.7}$$

where $\mathbf{y}$, $\mathbf{a}(\theta)$ and $\mathbf{e}$ are *Kx1* complex vectors. The contribution of the thermal noise is modeled through $\mathbf{e}$ and the steering vector $\mathbf{a}(\theta)$ collects the phase difference between the channels, which is directly related to the DOA:

$$\mathbf{a}(\theta) = \left[\left[\exp\left\{-j \cdot \frac{2\pi}{\lambda} \cdot d \cdot (k-1) \cdot \sin(\beta - \theta)\right\}\right]_{k=1}^{K}\right]^T \tag{4.8}$$

The estimation of the DOA would be improved by the availability of independent and identically distributed observations of the signal $\mathbf{y}$. Then, it is interesting to consider the echoes, corresponding to the same target, from different, subsequent pulse transmissions. These multiple observations or *snapshots* are acquired during the azimuth displacement of the satellite. As the satellite is flying, the acquisition geometry is changing, which implies: variation of the echo DOA and presence of the range cell migration (RCM) effect on the time delay (section 2.1.4), i.e. the position of the recorded samples for the same target changes.

A detailed analysis of the multiple acquisitions and the associated effects can be found in Annex A.2. For a number of snapshots < 100, the DOA variation ($< 10^{-5}$ degrees) can be neglected in comparison with the best achievable performance of the ADBF, i.e. the Cramér-Rao Lower Bound $\approx 0.003º$ (see section 7.3.4). The RCM effect can be omitted when the snapshots are below 72 since the range variation for those cases is below 1/30 times the slant range resolution ($\delta_r \approx 0.6$ m)[17].

These observations allows considering N equivalent samples or snapshots of the signal in Eq. (4.7):

$$\mathbf{y}(n) = \gamma \cdot \mathbf{a}(\theta) + \mathbf{e}(n), \qquad n = 1,\ldots,N \tag{4.9}$$

[17] In general, for the whole swath (170 km – 557 km) imaged by the HRWS SAR in Table 7-1, a number of snapshots below 72 allows neglecting variations of the DOA ($< 1.25x10^{-5}$ degrees) and RCM (< 0.022 m).

In real scenarios, multiple echoes of the transmitted pulses are acquired simultaneously by the receive antenna due to: a) signal of interest (actual echo) in combination with preceding or succeeding pulses with time-delays separated a multiple of the PRF, known as *range ambiguities* [14] or b) backscattering sources in *layover*, i.e. the echo from different terrain patches with different topography arrive simultaneously (same time-delay) to the antenna [23]. Figure 4-2 illustrates a possible scenario with sources in layover and range-ambiguous returns.

Under the principle of superposition, Eq. (4.9) can be generalized to account for N_s sources:

$$\mathbf{y}(n) = \sum_{i=1}^{N_s} \gamma_i \cdot \mathbf{a}(\theta_i) + \mathbf{e}(n), \qquad n = 1, \ldots, N \tag{4.10}$$

At this point it has been recovered a narrowband data model completely analog to the one described in section 3.2.1.1. In fact, the recorded samples at the different channels or sub-apertures differ only from a phase term, independent on the bandwidth of the echo and equivalent to the propagation of a plane wave with wavelength λ and DOA θ_i. Therefore, it is possible to apply the different narrowband estimation algorithms in order to retrieve the estimate of the actual DOA $\hat{\theta}_i$, used as input to steer the receive beam pattern in elevation. Actually, the beam is directed towards the center of the chirp pulse, i.e. the estimated DOA corresponds to the carrier frequency. A further frequency dependent beam dispersion is required to deal with long chirp signals, as is done for conventional SCORE [48]. In the thesis it is assumed that once the DOA of the pulse center has been acquired, both the conventional and adaptive approaches are able to retrieve the energy from the whole pulse without losses.

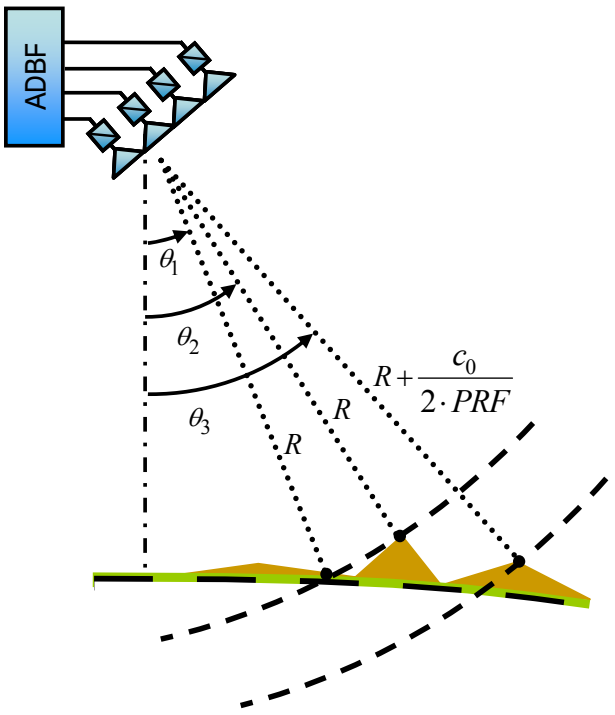

Figure 4-2: Multi-source scenario, first and second sources in layover and third source corresponds to a range ambiguity (distances and angles not in scale).

4.2 Narrowband DOA estimation algorithms

In this section is described the possible narrowband estimation methods considered in the implementation of the ADBF: beam-forming techniques, such as Beamformer and Capon and the subspace method MUSIC. All these methods generate functionals of the DOA, based on the availability of the spatial covariance matrix $\mathbf{R}_\mathbf{y}$:

$$\mathbf{R}_y = E\left\{\mathbf{y}(n)\mathbf{y}^H(n)\right\} \tag{4.11}$$

with $\mathbf{y}(n)$ the $Kx1$ data vector and $(\cdot)^H$ conjugate and transpose operator.

4.2.1 Beam-forming techniques

Beamformer and Capon are classified as exploration techniques since they scan the "space" sequentially through a beam that is dependent on the desired direction to be focused. In this sense, they can be interpreted as spatial filters that pass the desired direction and try to attenuate the contribution from all other directions. Both provide an estimation of the spatial power spectral density (PSD).

Let's consider the vector $\mathbf{h}$ that contains the K complex coefficients of the filter:

$$\mathbf{h} = \begin{bmatrix} h_1 & h_2 & \cdots & h_K \end{bmatrix}^T \tag{4.12}$$

To provide an estimate of the spatial power distribution as a function of the DOA, both methods rely on the measure of the mean power at the output of the filter given the data $Kx1$ vector $\mathbf{y}(n)$:

$$E\left\{\left|\mathbf{h}^H \cdot \mathbf{y}(n)\right|^2\right\} = \mathbf{h}^H \cdot \mathbf{R}_\mathbf{y} \cdot \mathbf{h} \tag{4.13}$$

In the design of the complex coefficients $\mathbf{h}$, the first condition is to keep the desired DOA without distortion:

$$\mathbf{h}^H \cdot \mathbf{a}(\omega_s) = 1 \tag{4.14}$$

where ω_s is defined as the spatial frequency, directly related to the DOA from the steering vector $\mathbf{a}(\theta)$ in Eq. (4.8):

$$\omega_s = -2\pi \frac{d}{\lambda} \cdot \sin(\beta - \theta), \qquad -\pi \le \omega_s \le \pi \tag{4.15}$$

The second driver filter design tries to minimize the contribution of all other directions as much as possible. It is precisely this requisite the one that differentiate both, Beamformer and Capon.

4.2.1.1 Beamformer

The Beamformer filter is obtained as the solution to the following optimization problem:

$$\mathbf{h}_{BF} = \arg\min_{\mathbf{h}} \left\{ \mathbf{h}^H \cdot \mathbf{h} \right\}, \quad \text{constrained to } \mathbf{h}^H \cdot \mathbf{a}(\omega_s) = 1 \tag{4.16}$$

Under this optimization criterion and from Eq. (4.13), the quantity to minimize results in the output power for the spatially white scenario, i.e. $\mathbf{R_y} = \mathbf{I}$, which leads to the Beamformer filter[18]:

$$\mathbf{h}_{BF} = \frac{\mathbf{a}(\omega_s)}{\sqrt{\mathbf{a}^H(\omega_s) \cdot \mathbf{a}(\omega_s)}} = \frac{\mathbf{a}(\omega_s)}{K} \tag{4.17}$$

From Eq. (4.17), Beamformer can be interpreted as a filter matched to the desired DOA and independent on the data ($\mathbf{R_y}$), such that introduced in Eq. (4.13) provides the functional:

$$\hat{P}_{BF}(\omega_s) = \frac{\mathbf{a^H}(\omega_s) \cdot \hat{\mathbf{R}}_\mathbf{y} \cdot \mathbf{a}(\omega_s)}{K^2} \tag{4.18}$$

where $\hat{\mathbf{R}}_\mathbf{y}$ represents an estimate of the unknown covariance matrix $\mathbf{R_y}$.To obtain the spatial PSD, the previous equation should take into account a normalization factor [25]. However, this normalization does not affect the estimation of the DOAs and is omitted.

The DOA estimates $\left\{\hat{\theta}_i\right\}$ are directly related to the spatial frequencies $\left\{\hat{\omega}_{s,i}\right\}$ estimates, obtained as the locations of the N_s highest peaks in the functional or spectrum (4.18).

Considering the estimate $\hat{\mathbf{R}}_\mathbf{y}$ as the sample covariance matrix obtained from the N available snapshots of the data $\mathbf{y}(n)$:

$$\hat{\mathbf{R}}_\mathbf{y} = \frac{1}{N} \cdot \sum_{n=1}^{N} \mathbf{y}(n) \cdot \mathbf{y^H}(n), \tag{4.19}$$

Beamformer is regarded as the spatial analogue of the classical *periodogram* in spectral estimation [33],[44]. In fact, the expression in (4.18) can be understood as averaging the periodogram over N snapshots:

$$\hat{P}_{BF}\left(\omega_s\right) = \frac{1}{K^2 N} \sum_{n=1}^{N} \left| \mathbf{a^H}(\omega_s) \cdot \mathbf{y}(n) \right|^2 \tag{4.20}$$

The analogy with the periodogram suggests that the resolution[19] of Beamformer is also restricted by the so-called *Rayleigh* limit, about $\lambda/(\text{antenna height})$, i.e. in the order of the antenna beamwidth, see Figure 4-3.

[18] The problem of minimization with restrictions can be solved using *Lagrange multipliers* [50].

[19] Resolution understood as the capability to discern between two frequency components or in this particular case between two DOAs.

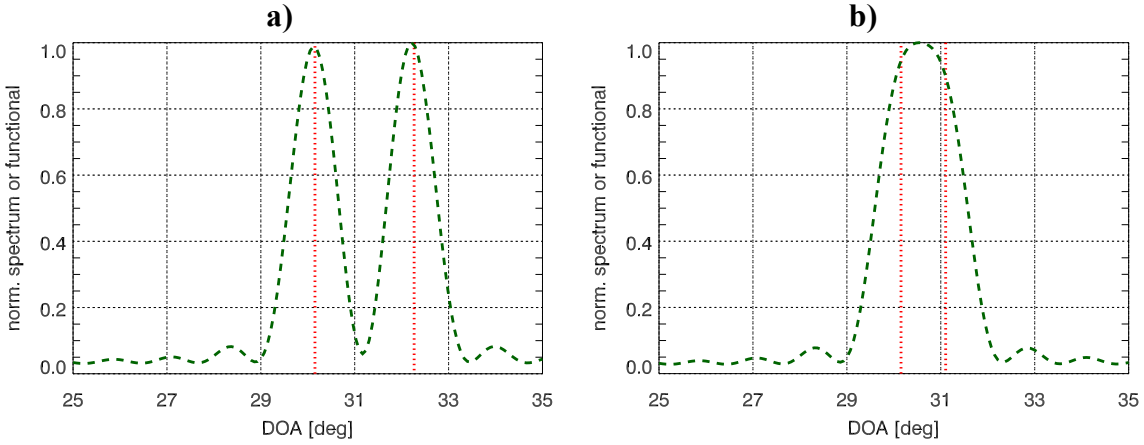

Figure 4-3: Normalized Beamformer spectrum for two sources separated, **a)** above and **b)** below the antenna beamwidth $\approx 1^{o}$ (red dotted lines indicate true DOAs).

4.2.1.2 Capon

Beamformer suffers from leakage introduced by the directions different from the desired one, $\text{DOAs} \neq \theta$, since the filter used to explore every DOA was the same and independent on the data. In this sense Capon is designed as a "data-dependent" filter under the following criterion:

$$\mathbf{h}_C = \arg\min_{\mathbf{h}} \left\{ \mathbf{h}^H \cdot \mathbf{R}_y \cdot \mathbf{h} \right\}, \quad \text{constrained to } \mathbf{h}^H \cdot \mathbf{a}(\omega_s) = 1 \tag{4.21}$$

The solution to the prior minimization is given by

$$\mathbf{h}_C = \frac{\hat{\mathbf{R}}_y^{-1} \cdot \mathbf{a}(\omega_s)}{\mathbf{a}^H(\omega_s) \cdot \hat{\mathbf{R}}_y^{-1} \cdot \mathbf{a}(\omega_s)} \tag{4.22}$$

where the spatial covariance matrix $\mathbf{R}_y$ has been substituted by an estimate $\hat{\mathbf{R}}_y$.

Capon provides an estimate of the PSD and the DOA estimates $\left\{\hat{\theta}_i\right\}$ are also obtained through the spatial frequencies $\left\{\hat{\omega}_{s,i}\right\}$ as the location of the N_s highest peaks in:

$$\hat{P}_C(\omega_s) = \frac{1}{\mathbf{a}^H(\omega_s) \cdot \hat{\mathbf{R}}_y^{-1} \cdot \mathbf{a}(\omega_s)} \tag{4.23}$$

From Eq. (4.22), the Capon filter is formulated as data adaptive, which allows reducing the leakage from closely spaced sources and obtaining a better resolution capability compared to classical Beamformer. In Figure 4-4, the normalized spectrums for both methods are represented for a separation between the sources below the antenna beamwidth. It can be observed that Capon provides a spectrum with reduced width of the peaks and lower secondary lobes compared to Beamformer. However, this improved resolution is quite dependent on the antenna size and the level of Signal-to-Noise ratio [33].

4.2.2 Multiple Signal Classification (MUSIC)

MUSIC, proposed by Schmidt in [39], is a subspace method that exploits in an efficient way the structure of the covariance matrix $\mathbf{R}_y$ through its *eigenvectors* and *eigenvalues*[20].

It was conceived as a parametric algorithm for frequency estimation of sinusoidal signals embedded in additive white noise [44]. Thus, the associated power spectral density (PSD) is formed by spectral lines centered in the expected frequencies or analogy in the DOAs for the spatial case. Additionally, MUSIC assumes that the number of sources N_s is known and none of them are completely correlated or *coherent*. According to [39], the functional of the MUSIC algorithm is expressed as:

$$\hat{P}_M(\omega_s) = \frac{1}{\mathbf{a}^H(\omega_s)\cdot\hat{\mathbf{E}}\cdot\hat{\mathbf{E}}^H\cdot\mathbf{a}(\omega_s)} \tag{4.24}$$

where $\hat{\mathbf{E}}$ is the noise subspace. The columns of this $Kx(K-N_s)$ matrix correspond to the eigenvectors associated to the $(K-N_s)$ smallest eigenvalues of the Singular Value Decomposition (SVD) of the estimated covariance matrix $\hat{\mathbf{R}}_y$.

$\hat{P}_M(\omega_s)$ is not a true spectrum, but exhibit peaks in the vicinity of $\{\omega_{s,i}\}$ or equivalently the DOAs, since the steering vectors of the true DOAs $\mathbf{a}(\omega_s)$ are orthogonal to the noise subspace [43]. Therefore, the estimates $\{\hat{\theta}_i\}$ are related to the location of those peaks in the "pseudospectrum".

Figure 4-4 illustrates that this algorithm offers an improved resolution capability (narrower peaks) compared to Beamformer and Capon. However, those two methods are more robust than MUSIC as they do not assume any specific model for the data. Moreover, MUSIC considers the number of sources to be known. Then, if the model does not accurately match the one assumed by MUSIC, degradation in the performance is expected.

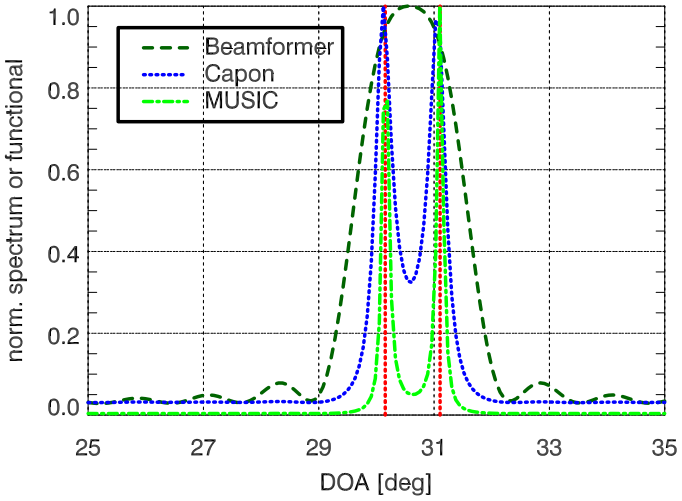

Figure 4-4: Beamformer, Capon and MUSIC normalized spectrums for two sources separated below the antenna beamwidth $\approx 1^o$ (red dotted lines indicate true DOAs).

[20] A detailed algebraic matrix review can be found in annex A of *Van Trees* [50].

4.3 Unambiguous Direction of Arrival range

A multi-channel antenna provides a finite *spatial sampling* of the impinging signals. Then, the vector $\mathbf{a}(\theta)$ or equivalently $\mathbf{a}(\omega_s)$ is uniquely defined, i.e. no *spatial aliasing* exists, when the spatial frequency is constrained to:

$$|\omega_s| \leq \pi, \tag{4.25}$$

which is reformulated according to Eq. (4.15) as:

$$d \cdot |\sin(\beta - \theta)| \leq \frac{\lambda}{2} \tag{4.26}$$

In a ULA the DOAs measured respect to broadside of the antenna, i.e. angle $(\theta - \beta)$ [21], are limited to the interval $[-90º, 90º]$. This is because two sources located at symmetric positions respect to the line of the antenna can not be distinguished one from the other. Then, both have the same time delays and steering vectors. Taking into account this interval of DOAs, Eq. (4.26) is satisfied if

$$d \leq \frac{\lambda}{2} \tag{4.27}$$

This means that when the inter-element spacing, i.e. the spatial sampling period, is greater than half of the wavelength, the response of the array is ambiguous. Therefore, two or more sources with different DOAs can have the same steering vector and can not be distinguished. Equivalently, periodicities in the spatial spectrum appear as the associated spatial frequencies lie out of the interval (4.25).

Figure 4-5 illustrates the occurrence of these ambiguous responses or periodicities in the spectrum. It can be observed that not only a peak in the vicinity of the true position is formed, but also false peaks associated to the spatial aliasing are present within the scan angle range $[-90º, 90º]$.

In the case of Beamformer and Capon the appearance of these ambiguous peaks can be explained by the analog phenomena of grating lobes in the array pattern formation [50]. These ambiguities arise in the MUSIC pseudospectrum since two or more DOAs have the same array response and so two or more steering vectors are orthogonal to the noise subspace, from Eq. (4.24).

[21] Counterclockwise defined.

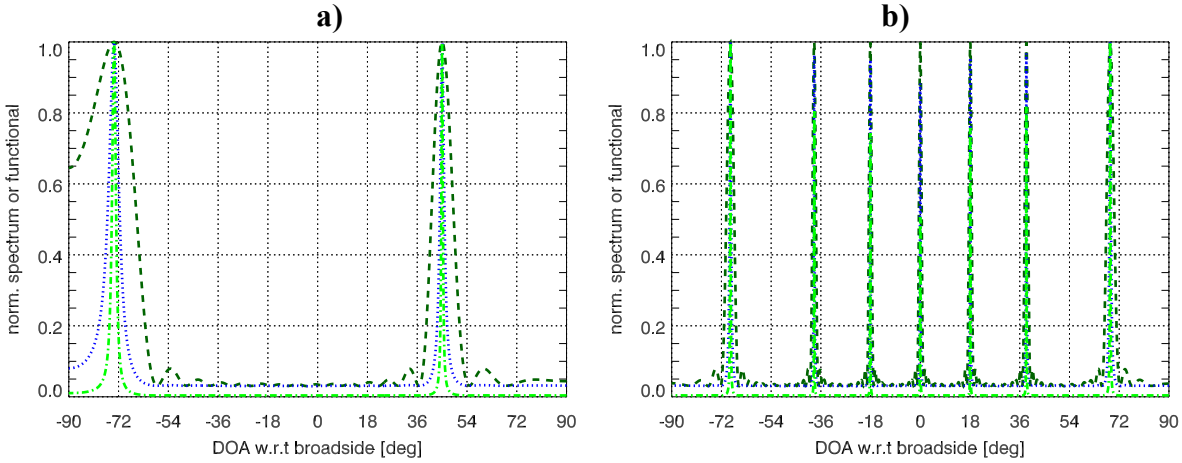

Figure 4-5: Ambiguities in Beamformer (dark green dashed curve), Capon (blue dotted curve) and MUSIC (light green dash-dotted line) normalized spectrums versus DOA w.r.t. broadside of the antenna for a unique source: **a)** at 45º and d=0.6λ **b)** at 0º and d=3.218λ.

In any case, this ambiguous problem is translated into misleading results as two or more DOAs are estimated and only one valid DOA exits, but in practice this is unknown to the user.

In order to avoid these ambiguous peaks in the estimation, the formation of the spatial spectrum is restricted to a specific range of DOA, known as *unambiguous range* (UR). This is achieved constraining the spatial frequency to $|\omega_s| \leq \pi$, when the inter-element spacing is $d > \lambda/2$. From Eq. (4.15), the unambiguous range in terms of DOA w.r.t. nadir, for $d > \lambda/2$ [22], can be expressed as:

$$\beta - \arcsin\left(\frac{\lambda}{2d}\right) < \theta_{unamb} < \beta + \arcsin\left(\frac{\lambda}{2d}\right) \tag{4.28}$$

For the reference system in Table 7-1, the corresponding UR is $23.3º < \theta_{unamb} < 41.2º$. This span allows covering the DOAs ($29.6º \leq \theta_{swath} \leq 35.3º$) of the sources of interest located within the imaged swath (300 km – 370 km) for topographic heights from 0 km to 8 km.

[22] For $d \leq 0.5\lambda$ the unambiguous range of DOA is $[\beta - 90º, \beta + 90º]$.

4.4 Peak detection and sorting estimates

Beamformer, Capon and MUISC provide the corresponding DOA estimates based on the detection of the N_s highest peaks in the estimated spectrums or functionals. As mentioned before, Beamformer and Capon do not require from the knowledge of the number of sources N_s to perform the estimation. However, in MUSIC the correct determination of N_s results crucial for the good operation of this sub-space method [26]. Along the thesis, the number of sources is assumed known.

The search for those peaks in the estimated spectrums or functional of the different methods is performed in a two-step procedure. First, a rough detection is done. Afterwards, the DOAs are accurately retrieved by the recomputation of the spectrums in the vicinity of the first estimated peaks.

To obtain the performance of the different algorithms[23], the estimates have to be associated to the corresponding true DOAs. Therefore, a kind of search and sort algorithm is required.

In this work, the criterion of minimum distance has been selected. It must be noted that the following algorithm has been implemented considering just two sources, which is the scenario analyzed in Chapter 7. For each one of the possible combinations that associate the true DOAs $\{\theta_i\}$ and the estimated DOA $\{\hat{\theta}_i\}$ the distances are computed in absolute terms. Then, the true/estimate pairs with minimum distances are selected. In case the two estimates are linked to the same true DOA, it should be compared the distances to the other true DOA, which is associated to the estimate with minimum distance.

[23] In Chapter 7, the specific performance measurements for ADBF are presented for the numerical part.

Chapter 5 Data Model

In any parameter estimation problem, the proper definition of a model is necessary to further develop the analytical study and evaluate the potentiality of the estimation method. In this chapter the data model at the output of the multi-channel receive antenna is described and statistically characterized.

5.1 Formulation

Consider a spaceborne SAR system with orbital height H_{orb} as in Figure 5-1 a), where the receive antenna is formed by K sub-apertures in elevation aligned as a uniform linear array. Assuming that each sub-aperture has a dimension equal to the inter-element spacing d, it should be distinguished: the total height of the antenna $H_a = K \cdot d$ and the distance between the extreme phase centers $Q = (K-1) \cdot d$, see Figure 5-1 b). The geometric description is completed with two angles measured respect to nadir: the tilt angle β corresponds to the broadside of the antenna, looking at center of the swath, and θ is the DOA of a ground target with a topographic height h.

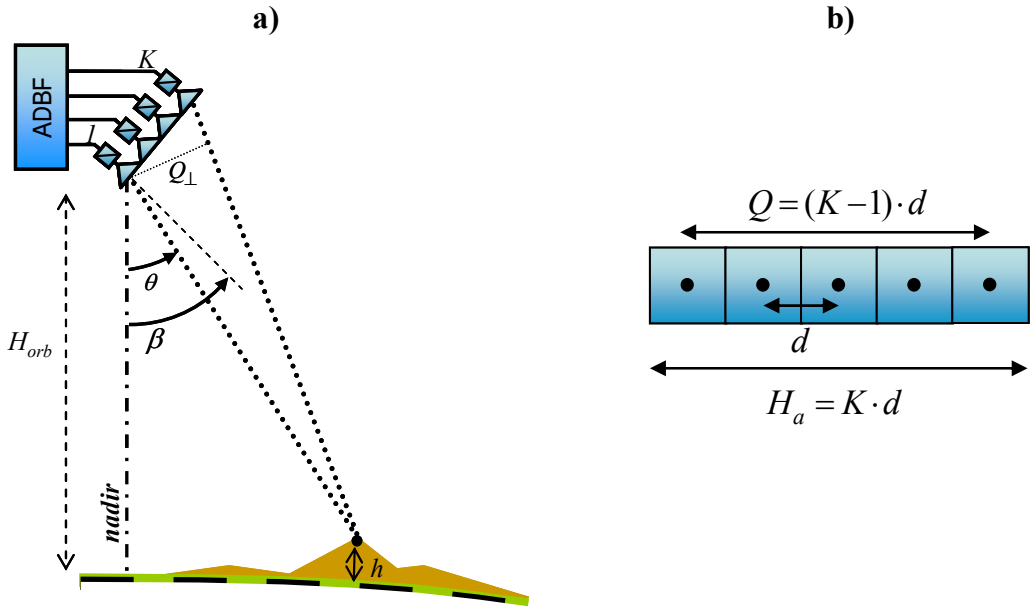

Figure 5-1: a) Acquisition geometry in vertical plane **b)** receive antenna structure.

From Chapter 4, the pre-processed data at the output of the K sub-apertures for point targets is expressed as:

$$\mathbf{y}(n) = \sum_{i=1}^{N_s} \gamma_i \cdot \mathbf{a}(\theta_i) + \mathbf{e}(n), \qquad n = 1, \ldots, N \tag{5.1}$$

where $\mathbf{y}(n)$, $\mathbf{a}(\theta_i)$ and $\mathbf{e}(n)$ are $Kx1$ complex vectors; N is the number of snapshots that allow having equivalent observations of the data (annex A.2) and N_s is the number of targets, i.e. sources in layover or range ambiguities (Figure 4-2). It is assumed that $N_s \leq K-1$, otherwise the estimation problem would not be identifiable. The first term in Eq. (5.1) represents the useful signal contribution, where the complex term γ_i accounts for the backscattering and propagation mechanism; and $\mathbf{a}(\theta_i)$ is the steering vector expressed as in Eq. (4.8). Finally, $\mathbf{e}(n)$ denotes the additive thermal noise that corrupts the useful component of the data.

The previous data model is generalized to take into account extended homogeneous backscattering sources, where each one is characterized by a multiplicative noise known as speckle (section 2.1.6). Then, Eq. (5.1) is rewritten as [23]:

$$\mathbf{y}(n) = \sum_{i=1}^{N_s} \sqrt{\alpha_i} \cdot \mathbf{a}(\theta_i) \otimes \mathbf{x}_i(n) + \mathbf{e}(n), \text{ for } n = 1,..., N \tag{5.2}$$

where $\otimes$ indicates the *Hadamard* product[24]; $\mathbf{x}_i(n)$ is the speckle complex K-dimensional vector of the $i-th$ source and the real scalar term α_i denotes the radar reflectivity of each source, i.e. the mean power level related to the source.

In order to statistically describe Eq. (5.2), it is referred to the data model used in multi-channel Interferometric SAR [23]. In that work, the estimation of the interferometric phase allows solving the problem of N_s sources in layover when applying spectral estimation algorithms on the complex pixel collected by K sensors.

Then, the estimation of the DOA corresponding to each slant range sample proposed by the ADBF turns to be analogous to the determination of the interferometric phase in [23]. However, there is a difference between the two models: in the InSAR model, the extended sources are bound by the pixel size, i.e. cell of dimensions equal to range and azimuth resolutions; whereas in the model here considered, they correspond to the areas illuminated by the mainlobe aperture of azimuth pattern and delimited by the range resolution cell.

In order to consider the statistical description of multi-channel InSAR, the model in Eq. (5.2) assumes an illuminated swath, with homogenous backscattering surface and constant topographic height along the ISO-range lines (all points with the same slant-range distance to the satellite).

As the received signal is spread over the azimuth pattern, the assumption on homogeneous surface allows modeling α_i as a deterministic parameter and the speckle component $\mathbf{x}_i(n)$ as complex Gaussian process[25]. Considering constant topographic height along ISO-range implies that all possible backscatters within the azimuth footprint collapse into the same DOA in the vertical plane for small azimuth apertures; otherwise, different elevation profiles for those targets are mapped into different DOAs, which is analogous to the layover problem. This additional contribution can affect the estimation performed by ADBF when sweeping the swath with the receive beam.

An example can better illustrate this latter situation. Assume the satellite is imaging the ocean, where a ship (high reflectivity) and a relief in the coast (different azimuth location) have the same slant range distance. Let's consider topographic heights of 0 km and 1 km respectively. Then, as computed in section 7.4, the DOA difference is below the resolution capabilities of the considered narrowband methods. From the estimated PSD a single peak can be distinguished, located in between the DOA of the ship and the coast relief (if both have same mean power level). Therefore, the ADBF will steer the beam towards a DOA in between the two targets.

[24] Element by element product ($[\mathbf{a} \otimes \mathbf{b}]_i = \mathbf{a}_i \cdot \mathbf{b}_i$).

[25] Gaussianity arises from the *central limit theorem* due to the multiple contribution of identically (homogeneous) distributed sources within the azimuth pattern extension.

This ideal assumption regarding the vertical profile (topography) is simple but allows comparing in a first approach the performance of the conventional SCORE with the ADBF.

Under the previous hypothesis, the contribution of the extended sources $\mathbf{x}_i(n)$ is modeled as a zero complex Gaussian process with unit variance and certain covariance KxK matrix $\mathbf{C}_i = E\left\{\mathbf{x}_i(n)\cdot\mathbf{x}_i^H(n)\right\}$, [23]. It is considered that the speckle components of different sources are independent ($\mathbf{x}_i(n)$ and $\mathbf{x}_j(n)$ independent for $i \neq j$) as the echoes are backscattered from different areas. Moreover, the speckle component for the different snapshots $\{\mathbf{x}_i(n)\}_{n=1}^{N}$ can be regarded as independent and identically distributed. This is true since the different observations appear to be realizations of the same random process: for each acquisition, the aspect geometry observation of the multiple scatterers that conform the extended sources is changing in a random fashion.

The thermal noise $\mathbf{e}(n)$ in Eq. (5.2) is modeled as complex Gaussian spatially and temporally white process with variance σ_e^2 and uncorrelated with the speckle.

Considering the previous statistical description of the data model (5.2), the signal at the output of the receive antenna $\mathbf{y}(n)$ has a Gaussian distribution $N(\mathbf{0},\mathbf{R}_y)$ with zero mean and covariance matrix $\mathbf{R}_y$:

$$\mathbf{R}_y = E\left\{\mathbf{y}(n)\cdot\mathbf{y}^H(n)\right\} = \sum_{i=1}^{N_s}\alpha_i\cdot\mathbf{A_i}\cdot\mathbf{C_i}\cdot\mathbf{A_i^H} + \sigma_e^2\mathbf{I} \tag{5.3}$$

where $\mathbf{I}$ is the identity KxK matrix, i.e. 1's at the diagonal, and $\mathbf{A_i}$ is a KxK diagonal matrix whose elements are the components of the steering vector $\mathbf{a}(\theta_i)$ of the $i-th$ source:

$$\mathbf{A_i} = diag\left\{\exp\left\{-j2\pi\frac{d}{\lambda}\cdot(k-1)\sin(\beta-\theta_i)\right\}\right\}_{k=1}^{K} \tag{5.4}$$

Then, the problem here presented is based on the estimation of the DOAs $\{\theta_i\}$ for each slant range sample corrupted by multiplicative noise $\mathbf{x}_i(n) \sim N(\mathbf{0},\mathbf{C}_i)$ and immersed in additive noise $\mathbf{e}(n) \sim N(\mathbf{0},\sigma_e^2\cdot\mathbf{I})$.

Finally, an important relation is the Array Signal-to-Noise ratio ($ASNR$) for the $i-th$ source:

$$ASNR_i = K\cdot\frac{\alpha_i}{\sigma_e^2} \tag{5.5}$$

where α_i/σ_e^2 corresponds to the Signal-to-Noise ratio at the individual sub-aperture.

Analogy to the case of multibaseline InSAR, it is assumed decorrelation of the speckle just due to the receive antenna geometry. In this sense, the speckle correlation sequences between the different sub-apertures have a triangular model [5],[23]:

$$\left[\mathbf{C}_i\right]_{u,v} = E\left\{\left[\mathbf{x}_i(n)\right]_u \cdot \left[\mathbf{x}_i(n)\right]_v^*\right\} = \begin{cases} 1 - \dfrac{|u-v|}{K-1} \cdot H_i & \text{for } |u-v| \le \dfrac{(K-1)}{H_i} \\ 0 & \text{otherwise} \end{cases} \tag{5.6}$$

where H_i is the normalized antenna height[26]:

$$H_i = \frac{Q_\perp}{H_{c,i}} = \frac{Q \cdot \cos(\beta - \theta_i)}{H_{c,i}}, \tag{5.7}$$

ratio between the orthogonal projection $Q_\perp$ to the line of sight (see Figure 5-1), and the critical antenna height $H_{c,i}$, for which the $i-th$ speckle component is completely decorrelated at the extreme sub-apertures. In annex A.3, this concept is related to the critical baseline in InSAR [18], which is dependent on the sensor parameters (frequency and bandwidth) and the local slope of the terrain. For the reference system in Table 7-1 and considering zero slope, the normalized antenna height is almost zero since $H_{c,i} \approx 20$ km - 27 km compared to $Q = 1.4$ m. Then, the speckle component is almost completely correlated along the different sub-apertures of the receive antenna.

From Eqs. (5.6) and (5.3), the correlation of the data between the different sub-apertures is expressed as:

$$\left[\mathbf{R}_y\right]_{u,v} = E\left\{\left[\mathbf{y}(n)\right]_u \cdot \left[\mathbf{y}(n)\right]_v^*\right\} = \sum_{i=1}^{N_s} \alpha_i \cdot \left[C_i\right]_{u,v} \cdot \exp\left\{j(u-v)\omega_{s,i}\right\} + \sigma_e^2 \cdot \delta(u-v) \tag{5.8}$$

where $\omega_{s,i}$ is the spatial frequency associated to the $i-th$ source and $\delta(\cdot)$ is the *Kronecker* delta function.

The Discrete Fourier Transform (DFT) of the sequences in Eq. (5.8) provides the theoretical spatial PSD in terms of the spatial frequency ω_s:

$$S_y(\omega_s) = \sum_{i=1}^{N_s} \frac{\alpha_i \cdot H_i}{K-1} \cdot \frac{\sin^2\left(\dfrac{(K-1)\cdot(\omega_s - \omega_{s,i})}{2 \cdot H_i}\right)}{\sin^2\left(\dfrac{\omega_s - \omega_{s,i}}{2}\right)} + \sigma_e^2 \tag{5.9}$$

[26] H_i is the normalized orthogonal projection to the line of sight of the distance between the extreme phase centers $Q = H_a - d$, with H_a the antenna height.

In Figure 5-2, the theoretical spatial PSD is presented versus the DOA, for a scenario with two sources. Its shape is a *sinc*-like function centered at the respective DOAs. From Eq. (5.9), its mainlobe width is controlled by the normalized antenna height. Thereby, when the speckle is completely correlated $H_i = 0$, the signal is constant over the different sub-apertures and the PSD is formed by spectral lines (sinusoidal signals in the spatial domain). On the other hand, increasing the decorrelation of speckle, implies a broadening of the PSD and it is expected a degradation in the estimation performance, confirmed by the numerical simulations in section 7.3.6.

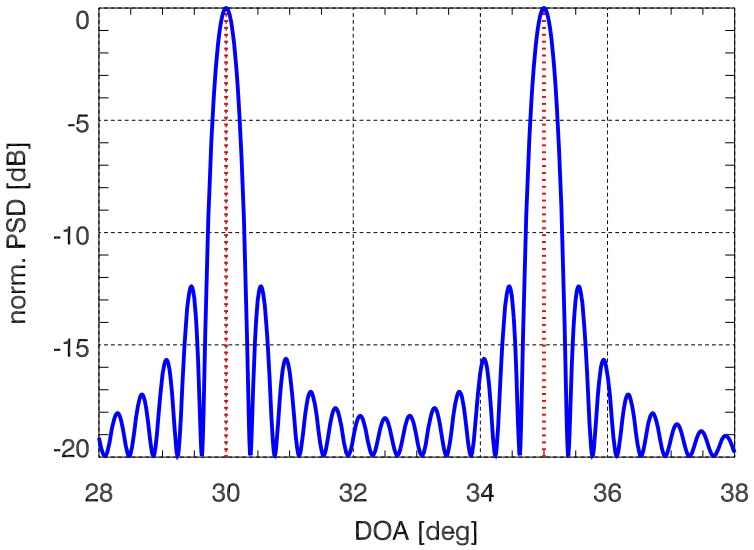

Figure 5-2: Theoretical normalized PSD, two-source scenario
($ASNR_{1,2} = 15$ dB , $\sigma_e^2 = 1$, $H_{1,2} = 0.3$, $K = 15$, $\theta_1 = 30^\circ$ and $\theta_2 = 35^\circ$)

Chapter 6 Cramér-Rao Lower Bound

In this chapter, the Cramér-Rao Lower Bound (CRLB) on the estimate of the DOAs is derived, providing a benchmark on the Adaptive Digital Beam-Forming performance since it represents a lower bound on the variance of any unbiased estimator. In a first approach, it is depicted a general description and formulation of the CRLB, which is later particularized for the data model presented in Chapter 5.

6.1 Definition

Assume a vector of *unknown parameters* $\boldsymbol{\chi}$ to be estimated from an available set of N samples of the observed data, e.g. the complex vector at the output of the receive antenna $\mathbf{y} \in \mathbb{C}^{Kx1}$. Consider $\hat{\boldsymbol{\chi}}$, the vector of *unbiased* estimates, i.e. $E\{\hat{\boldsymbol{\chi}}\} = \boldsymbol{\chi}$. Then, the CRLB sets a lower bound on the variance of these estimates, such that there exists no unbiased estimator whose variance is less than the CRLB [30],[44],[50]:

$$\mathrm{var}\{\hat{\chi}_i\} \geq CRLB(\chi_i) \tag{6.1}$$

From [44], the general CRLB formulation for multiple parameter estimation is:

$$\mathbf{C}_{CR}(\boldsymbol{\chi}) = \left(E\left\{ \left[\frac{\partial \ln f_N(\mathbf{y},\boldsymbol{\chi})}{\partial \boldsymbol{\chi}} \right] \cdot \left[\frac{\partial \ln f_N(\mathbf{y},\boldsymbol{\chi})}{\partial \boldsymbol{\chi}} \right]^T \right\} \right)^{-1} = \left(\mathbf{J}_{\mathrm{FIM}}\right)^{-1} \tag{6.2}$$

where $f_N(\mathbf{y},\boldsymbol{\chi})$ is the joint probability density function of the N samples of $\mathbf{y}$. The inner term $\mathbf{J}_{\mathrm{FIM}}$ is known as the Fisher Information Matrix (FIM), which provides the amount of relative information of the unknown parameters included in the observed data. Intuitively, the higher the information level, the lower is the bound and so the variance.

The CRLB on the different unknown parameters χ_i is obtained as the diagonal elements of the inverse of the FIM matrix [30]:

$$CRLB(\chi_i) = \left[\left(\mathbf{J}_{\mathrm{FIM}}\right)^{-1} \right]_{ii} \tag{6.3}$$

From this general description, two considerations are fundamental in the study of the CRLB. The first one is related to the statistical description of the data model, i.e. the distribution $f_N(\mathbf{y},\boldsymbol{\chi})$, and the second regarding the identification of the unknown parameters, $\boldsymbol{\chi}$. This latter concept is associated with the dimensionality of the problem, i.e. the higher the number of unknown parameters to estimate the bigger is the dimension of the Fisher matrix $\mathbf{J}_{\mathrm{FIM}}$.

6.2 Derivation

To evaluate the ultimate achievable performance of the ADBF approach, the CRLB on the DOA is computed based on the model presented in the previous chapter. The derivation is analog to the case of multibaseline InSAR [23]. The data vector $\mathbf{y}(n)$ in Eq. (5.2) contains additional parameters that should be also estimated. Then, from Eq. (5.2) and the speckle decorrelation model in Eq. (5.6), these *real deterministic* quantities are collected in:

$$\boldsymbol{\chi} = \left[\boldsymbol{\omega} \quad \boldsymbol{\alpha} \quad \mathbf{h} \quad \sigma_e^2 \right]^T \tag{6.4}$$

the $(3N_s + 1)x1$ vector of unknown parameters, where

$$\boldsymbol{\omega} = \left[\omega_{s,1} \quad \cdots \quad \omega_{s,N_s} \right], \text{ with } \omega_{s,i} = -\frac{2 \cdot \pi}{\lambda} \cdot d \cdot \sin(\beta - \theta_i) \tag{6.5}$$

correspond to the N_s spatial frequencies related to the parameters of interest, the DOAs $\{\theta_i\}$,

$$\boldsymbol{\alpha} = \left[\alpha_1 \quad \cdots \quad \alpha_{N_s} \right] \tag{6.6}$$

textures or radar reflectivity of the different sources,

$$\mathbf{h} = \left[H_i \quad \cdots \quad H_{N_s} \right] \tag{6.7}$$

the normalized antenna heights defined in Eq. (5.7) and σ_e^2 the noise variance.

Once the unknown parameters have been identified, the next step is to recognize the statistical distribution of the corresponding data. From the considerations made in Chapter 5, each of the N independent snapshots of $\mathbf{y}(n)$ is complex Gaussian distributed , $N(\mathbf{0}, \mathbf{R}_y)$, with zero mean vector and covariance matrix:

$$\mathbf{R}_y = E\left\{ \mathbf{y}(n) \cdot \mathbf{y}^H(n) \right\} = \sum_{i=1}^{N_s} \alpha_i \cdot \mathbf{A_i} \cdot \mathbf{C_i} \cdot \mathbf{A_i^H} + \sigma_e^2 \mathbf{I} \tag{6.8}$$

where $\mathbf{A_i}$ and the speckle covariance matrix $\mathbf{C_i}$ are respectively defined in Eqs. (5.4) and (5.6).

The first step to derive the CRLB on the DOAs $\{\theta_i\}$ is based on the computation of the FIM. For the zero mean Gaussian distribution of the N independent observations $\{\mathbf{y}(n)\}_{n=1}^{N}$, the elements of $\mathbf{J}_{\text{FIM}}$ according to [50] are:

$$\left[\mathbf{J}_{\text{FIM}} \right]_{i,j} = N \cdot tr\left\{ \mathbf{R_y^{-1}} \cdot \frac{\partial \mathbf{R}_y}{\partial \chi_i} \cdot \mathbf{R_y^{-1}} \cdot \frac{\partial \mathbf{R}_y}{\partial \chi_j} \right\} \tag{6.9}$$

where, $tr\{\mathbf{B}\}$ indicates the trace of the matrix $\mathbf{B}$, i.e. sum of the diagonal elements of the matrix.

To build up the Fisher matrix (6.9), the partial derivatives of the covariance matrix $\mathbf{R}_y$ respect to the unknown parameters $\boldsymbol{\chi}$ have to be computed:

$$\frac{\partial \mathbf{R}_y}{\partial \omega_{s,i}} = j \cdot \alpha_i \cdot \mathbf{A_i} \cdot \mathbf{C_i} \cdot \mathbf{A_i^H} \otimes \mathbf{L_0} \tag{6.10}$$

$$\frac{\partial \mathbf{R}_y}{\partial \alpha_i} = \mathbf{A_i} \cdot \mathbf{C_i} \cdot \mathbf{A_i^H} \tag{6.11}$$

$$\frac{\partial \mathbf{R}_y}{\partial H_i} = \alpha_i \cdot \mathbf{A_i} \cdot \mathbf{L_1} \cdot \mathbf{A_i^H} \tag{6.12}$$

$$\frac{\partial \mathbf{R}_y}{\partial \sigma_e^2} = \mathbf{I} \tag{6.13}$$

where $\otimes$ indicates the Hadamard product between matrices,. $\mathbf{L_0}$ and $\mathbf{L}_1$ are *KxK* Toeplitz[27] matrices with elements:

$$\left[\mathbf{L}_0\right]_{i,j} = (i-j), \qquad i,j = 1,\ldots,K \tag{6.14}$$

and

$$\left[\mathbf{L_1}\right]_{i,j} = -\frac{|i-j|}{K-1}, \qquad i,j = 1,\ldots,K \tag{6.15}$$

In Eq. (6.4) it has been considered as unknown parameters the spatial frequencies $\{\omega_{s,i}\}$ associated to each source, which are related to the DOAs through Eq. (4.15). Then, based on the transformation of parameters formula (pp. 44, [30]) the CRLB on $\{\theta_i\}$ can be expressed as:

$$CRLB(\theta_i) = \left[\mathbf{G} \cdot \mathbf{J}_{\text{FIM}}^{-1} \cdot \mathbf{G}^T\right]_{i,i}, \quad i = 1,\ldots,N_s \tag{6.16}$$

where, $\mathbf{G}$ is a $(3N_s+1)x(3N_s+1)$ diagonal matrix with elements:

$$\left[\mathbf{G}\right]_{i,j} = \begin{cases} \dfrac{\lambda}{2\pi d \cdot \cos(\beta - \theta_i)} & \text{for } i = j = 1,\ldots,N_s \\ 1 & \text{for } i = j = N_s+1,\ldots,3N_s+1 \\ 0 & \text{otherwise} \end{cases} \tag{6.17}$$

[27] A Toeplitz matrix has constant diagonals, i.e. the elements along each diagonal of the matrix are equal.

From the definition of the FIM and taking into account the vector of unknown parameters here considered, it is expected that the CRLB on the DOAs is affected by:

- The DOAs themselves. From Eq. (6.16), the term $\cos(\beta - \theta_i)$ in the denominator indicates that signals impinging the array from the *Broadside*, i.e. β, are better estimated than the ones entering from *Endfire* (along antenna axis). Then, the array antenna is more sensitive to DOAs in the first cases.

- Array Signal-to-Noise Ratio $\{ASNR_i\}$ of the different sources.

- The antenna aperture size, in terms of number of sub-apertures K and inter-element spacing d.

- Level of speckle decorrelation, measured through normalized antenna height $\{H_i\}$.

Then, the different system parameters affect the ultimate performance of the ADBF algorithm provided by the CRLB. A study of the ADBF potentiality can be found in [7]. In this work the possibilities of the ADBF are comparatively analyzed respect to SCORE through the computation of the CRLB in Eq. (6.16) for the main SAR parameters in a realistic scenario.

Chapter 7 Numerical Analysis

In this chapter the performance of the novel algorithm ADBF is evaluated by Monte Carlo (MC) simulations and compared with conventional SCORE as a function of single parameters of interest, keeping constant the value of the other parameters for a given reference HRWS SAR realistic system/scenario.

7.1 Performance parameters

To comparatively evaluate the ADBF approach against the conventional SCORE, it is necessary to define which are the performance measures.

According to [7] and as it is described in section 2.3.3, the loss in SCORE performance is quantified in terms of the so called *angular displacement* and the associated *pattern loss*. Analogy, it is defined the corresponding measures for the ADBF approach.

- ***Angular displacemenet***

The angular displacement $\Delta\theta_s$ in the conventional SCORE represents a deterministic measure:

$$\Delta\theta_s = \theta - \theta_s, \tag{7.1}$$

difference between steering direction θ_s and the actual echo DOA θ.

In the ADBF case, the angular displacement is statistically described by the Root Mean Square Error on the estimation of the actual echo DOA $\hat{\theta}$:

$$\Delta\theta_a = RMSE(\hat{\theta}) = \sqrt{E\left\{\left(\hat{\theta}-\theta\right)^2\right\}} = \sqrt{b^2(\hat{\theta}) + \mathrm{var}(\hat{\theta})}, \tag{7.2}$$

a measure of how far is the estimate from the actual echo DOA (accuracy of the estimation), including both the bias:

$$b(\hat{\theta}) = E\left\{\hat{\theta}-\theta\right\}, \tag{7.3}$$

which provides an idea of how large in average is the estimation error; and the variance

$$\mathrm{var}(\hat{\theta}) = E\left\{\left(\hat{\theta}-E\left\{\hat{\theta}\right\}\right)^2\right\}, \tag{7.4}$$

or the degree of dispersion of the estimates.

In the numerical simulations the CRLB on the echo DOA is also included, providing the best achievable performance for the adaptive approach. Then, for any unbiased estimation, i.e. $b(\hat{\theta}) = 0$, is true[28]:

$$\Delta\theta_a \geq \sqrt{CRLB(\theta)} \tag{7.5}$$

The CRLB provides a benchmark to selectively discern between the different estimation algorithms giving an insight on their statistical efficiency. Therefore, the comparative study allows to determine which are the most appropriate estimators that are able to keep its performance below the conventional SCORE and as close as possible to the CRLB.

[28] For any unbiased estimation the RMSE coincides with the square root of the variance and the result stated by the CRLB holds (see section 6.1).

- ***Pattern Loss***

In both approaches, ADBF and SCORE, the steering direction θ_s does not match the actual echo DOA θ. Then, the signal impinging on the antenna is not acquired with the maximum gain of the receive pattern, which corresponds to θ_s, see Figure 7-1.

This gain loss is quantified in terms of *pattern loss* (PL), defined as the value of the normalized receive beam pattern, which weights the actual echo DOA of arrival, θ:

$$PL = \frac{C^R(\theta)}{C^R(\theta_s)}, \tag{7.6}$$

where $C^R(\theta)$ is the value of the elevation receive beam pattern generated by DBF corresponding to θ.

In the conventional SCORE, θ_s is computed according to Eq. (2.15). In the ADBF case it is reported a mean measure of the PL, i.e. average of the PLs obtained for the steering directions

$$\theta_s = \theta + b(\hat{\theta}) \pm std(\hat{\theta}), \tag{7.7}$$

where $b(\hat{\theta})$ and $std(\hat{\theta})$ are respectively the bias and the standard deviation[29] on the estimation of the actual DOA. The PL for CRLB is computed analogy, i.e. zero bias and standard deviation represented by the square root of the CRLB.

The extent of the PL depends on the receive beam shape. In particular, for the reference HRWS SAR in Table 7-1, the half power beamwidth (HPBW) is in the order of 1º (see Figure 7-1).

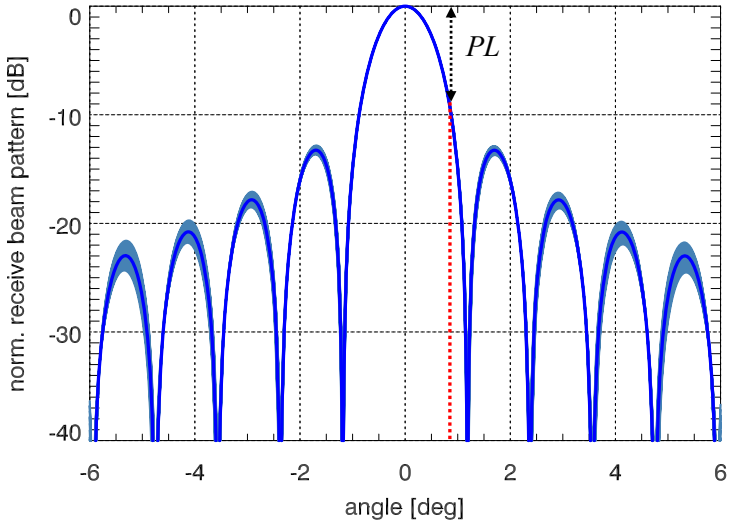

Figure 7-1: Normalized elevation receive beam patterns generated by DBF during the scansion of the swath (steering direction θ_s reported at the origin). Actual echo pattern weight indicated by red dotted line.

[29] The standard deviation is defined as the square root of the variance, $\sqrt{\text{var}(\hat{\theta})}$.

7.2 Reference scenario specifications

The numerical simulations here presented consider a realistic SAR scenario, based on the reference HRWS SAR system parameters indicated in Table 7-1. This system allows for a spatial resolution and swath width of 1 m and 70 km[30], respectively, a Noise-Equivalent Sigma Zero (NESZ) below -22 dB, Range-Ambiguity-to-Signal Ratio (RASR) below -30 dB and Azimuth-Ambiguity-to-Signal Ratio (AASR) below -26 dB. A proper definition of these quantities can be found in [6] and [14].

The reference acquisition scenario is illustrated in Figure 7-2 and the values of the different parameters are also included in Table 7-1. Two targets are assumed, where source #1 represents the signal coming from the imaged swath of interest (ground position 300 km -370 km) and source #2 is associated to the first far range ambiguity. The effect of higher order ambiguities is neglected since they are more than 18 dB below the "useful" signal (see Annex B).

The narrowband estimation methods search for unambiguous estimates restricted to $23.3^{\circ} < \theta_{unamb} < 41.2^{\circ}$, from Eq. (4.28). This span covers the possible DOA range of interest $29.6^{\circ} \leq \theta_{swath} \leq 35.3^{\circ}$, corresponding to sources located along the swath, considering topographic heights from 0 km to 8 km.

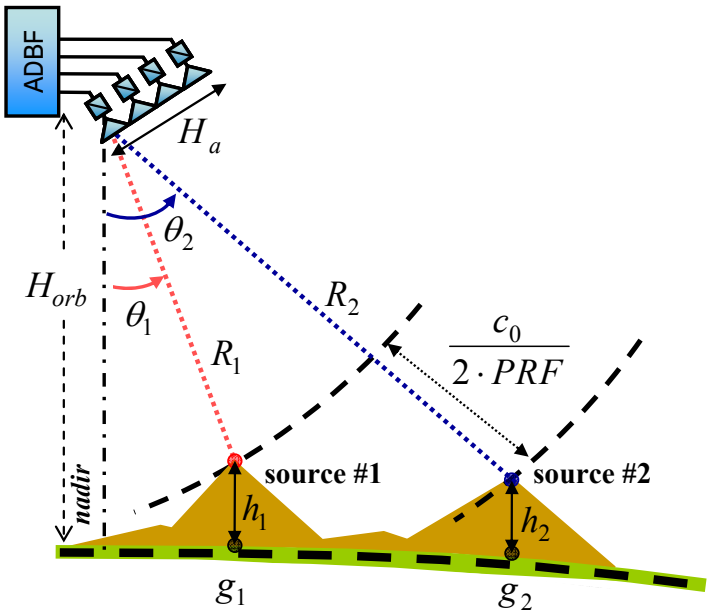

Figure 7-2: Reference scenario acquisition geometry (not in scale).

[30] The HRWS SAR system in Table 7-1 covers a whole swath of ground range between 170 km -557 km, by means of seven different subswaths mapped through a roll maneuver of the satellite (variation of the tilt angle of the antenna), [6]. The analysis here considered specifically assumes one of these subswaths (300 km- 370 km).

PARAMETER	SYMBOL	UNIT	VALUE
Geometry			
Orbit height	H_{orb}	[km]	520
Antenna tilt angle	β	[deg]	32.25
Swath limits (look ang.[31], ground range[32])		[deg] [km]	[29.6, 34.9] [300, 370]
Radar Parameters			
Pulse repetition frequency	PRF	[Hz]	1775
Carrier Frequency	f_c	[GHz]	9,65
Pulse Bandwidth	BW	[MHz]	250
Av. Tx Power		[W]	1100
TX Antenna			
Height	H_{tx}	[m]	0.50
Length	L_{tx}	[m]	2.45
RX Antenna			
Height	H_a	[m]	1.5
Nr. of sub-apert. in elevation	K		15 (x 0.10 m)
Length	L_{rx}	[m]	9.8
Nr. of sub-apert. in azimuth	M		7
Scenario Parameters			
Ground position	g	[km]	[304.41, 440.14]
Topographic height	h	[km]	[3, 3]
DOA	θ	[deg]	[30.15, 39.60]
Array Signal-to-Noise Ratio	$ASNR$	[dB]	[9, 3]
Normalized antenna height	H[33]		[$7\text{x}10^{-5}$, $4\text{x}10^{-5}$]
Snapshots	N		50

Table 7-1: HRWS SAR system parameters and reference scenario.

[31] Angle between the projection of the source on the Earth surface and nadir direction.
[32] Ground distance respect to the ground location of the satellite's nadir.
[33] The normalized antenna height is computed assuming zero local slope for both sources (see annex A.3).

7.3 Simulations

In this section the performance of the ADBF is numerically simulated via 10^4 Monte Carlo experiments (trials) using the IDL environment. Starting from the reference scenario/system presented in the previous section, ADBF and SCORE are comparatively evaluated in different operational scenarios, where single parameters of interest are varied keeping constant the others. Table 7-2 summarizes the different scenarios considered and the associated single parameter under variation. The objective is to analyze for which conditions the ADBF represents a better solution than the conventional SCORE.

The different simulations are based on the data model introduced in Chapter 5, which assumes homogeneous backscattering and constant topographic height along ISO-range lines.

The ADBF integrates narrowband estimation algorithms, which require from the estimation of the covariance matrix $\mathbf{R}_\mathbf{y}$. As it has been discussed, the number of snapshots or samples is limited by the DOA variation and the RCM effect (annex A.2). Then, it is considered *Forward-Backward averaging* to estimate $\mathbf{R}_\mathbf{y}$ since more accurate spectral estimates can be obtained (pp. 165-167, [44] and pp. 712-728, [50]):

$$\tilde{\mathbf{R}}_\mathbf{y} = \frac{1}{2}\cdot\left(\hat{\mathbf{R}}_\mathbf{y} + \mathbf{E}\cdot\hat{\mathbf{R}}_y^T\cdot\mathbf{E}\right) \tag{7.8}$$

where $\hat{\mathbf{R}}_\mathbf{y}$ is the sample covariance matrix defined in Eq. (4.19) and $\mathbf{E}$ is the exchange matrix, i.e. ones in its anti-diagonal and zero elsewhere.

In the following the performance regarding the source of interest (#1) is analyzed for the different operational scenarios. Conventional SCORE is computed also for source #1 with topographic height of 3 km. The results corresponding to the reference system are indicated by an asterisk in each figure. A summary of the numerical analysis for the different scenarios can be found at the end of this section in Table 7-3.

Scenario	Parameter Variation
0	Angular separation $\Delta\theta$ (θ_2 varies and θ_1 fixed)
1	Topographic height source #1, 2 (h_1, h_2)
2	Ground position source #1, 2 (g_1, g_2)
3	Array Signal-to-Noise Ratio source #1 ($ASNR_1$)
4	Antenna height (H_a) const. inter-element spacing (d)
5	Antenna height (H_a) const. number of elements (K)
6	Number of elements (K) const. antenna height (H_a)
7	Speckle decorrelation source #1 (norm. antenna height H_1)
8	Number of snapshots (N)

Table 7-2: Operational scenarios for the numerical performance analysis.

7.3.1 Angular separation

This scenario represents a preliminary step to decide which are the estimation algorithms among Beamformer, Capon and MUSIC, considered in the ADBF performance study.

In this case, the performance of the different estimation algorithms as a function of the angular (spatial) separation between the two sources is analyzed to confirm the different resolution capabilities of the methods.

The DOA corresponding to the first source is fixed, $\theta_1 = 30.15º$, and the second source is progressively distanced from the former one. It must be noted that the analysis here presented is symmetric to increasing the separation between the sources such that $\theta_2 \leq \theta_1$. To point out the capability of the methods to discern the DOAs, it has been considered a worse scenario, where the two sources have the same level, i.e. $ASNR_{1,2} = 9$ dB.

In Figure 7-3, the RMSE (angular displacement) and the bias on the estimation of θ_1 are evaluated as a function of the angular separation normalized to the receive antenna half power beamwidth (HPBW[34]). From this analysis comes clear the different resolution capabilities of the methods, where MUSIC provides the best one (separation $\Delta\theta \approx 0.7$ HPBW), dependent on the total aperture H_a and the level of $ASNR$. On the other hand Beamformer has the poorest resolution about 1.5 HPBW, limited by the antenna aperture. When the sources are really close to each other, the CRLB has a marked degradation due to numerical problems since it is not well-conditioned [41].

Comparing the bias of the different methods, when both sources almost collapse ($\Delta\theta \leq 0.25$ HPBW), Beamformer provides the lowest bias. This is because one estimate is associated to the mainlobe peak and the second is alternatively linked to secondary lobes symmetrically located at both sides of the former peak. Increasing the angular separation and below 0.7 HPBW, the bias on Beamformer turns to increase. In this situation the combination of the spectrums of both sources still provides one mainlobe peak and one predominant secondary lobe, which justifies the increase of the bias.

In any case the higher is the angular separation between the sources, the lower are the bias and RMSE (angular displacement) for the different estimation methods. At angular separations $\Delta\theta > 1.5$ HPBW Beamformer, Capon and MUSIC provide the same performance, reaching the CRLB with an approximate improvement w.r.t. SCORE about 0.5º.

[34] For the reference system the HPBW is in the order of 1º.

For the whole set of subswaths that the HRWS SAR system covers (170 km - 557 km) and the reference one (300 km -370 km), the angular separation between the source of interest and the first far range ambiguity[35] is located in an interval of 5º-15º. Therefore, the super-resolution capability offered by MUSIC is not required.

MUSIC is a model-based method, which assumes a spatial PSD of the signals formed by spectral lines. In real acquisition scenarios this hypothesis can not be regarded as valid in all circumstances. Moreover, the correct determination of the number of sources is critical in the operation of such a model-based signal-subspace method [26].

Beamformer and Capon do not rely on any *a priori* knowledge of the signals statistic and the number of sources. In this sense, they are more robust and provide an estimation of the spatial PSD, which can allow simply associating the DOA of the source of interest with the highest peak power concentration on the estimated spectrum.

From the previous premises, the MUSIC algorithm has been discarded in the performance analysis of the ADBF, carried for the different operational scenarios.

[35] The near range ambiguities and the higher order far ones can be neglected as they are weighted more than 18 dB below the signal of interest, see Annex B. These values are in accordance with the Range-Ambiguity-to-Signal Ratio (RASR) performance analysis carried in [6].

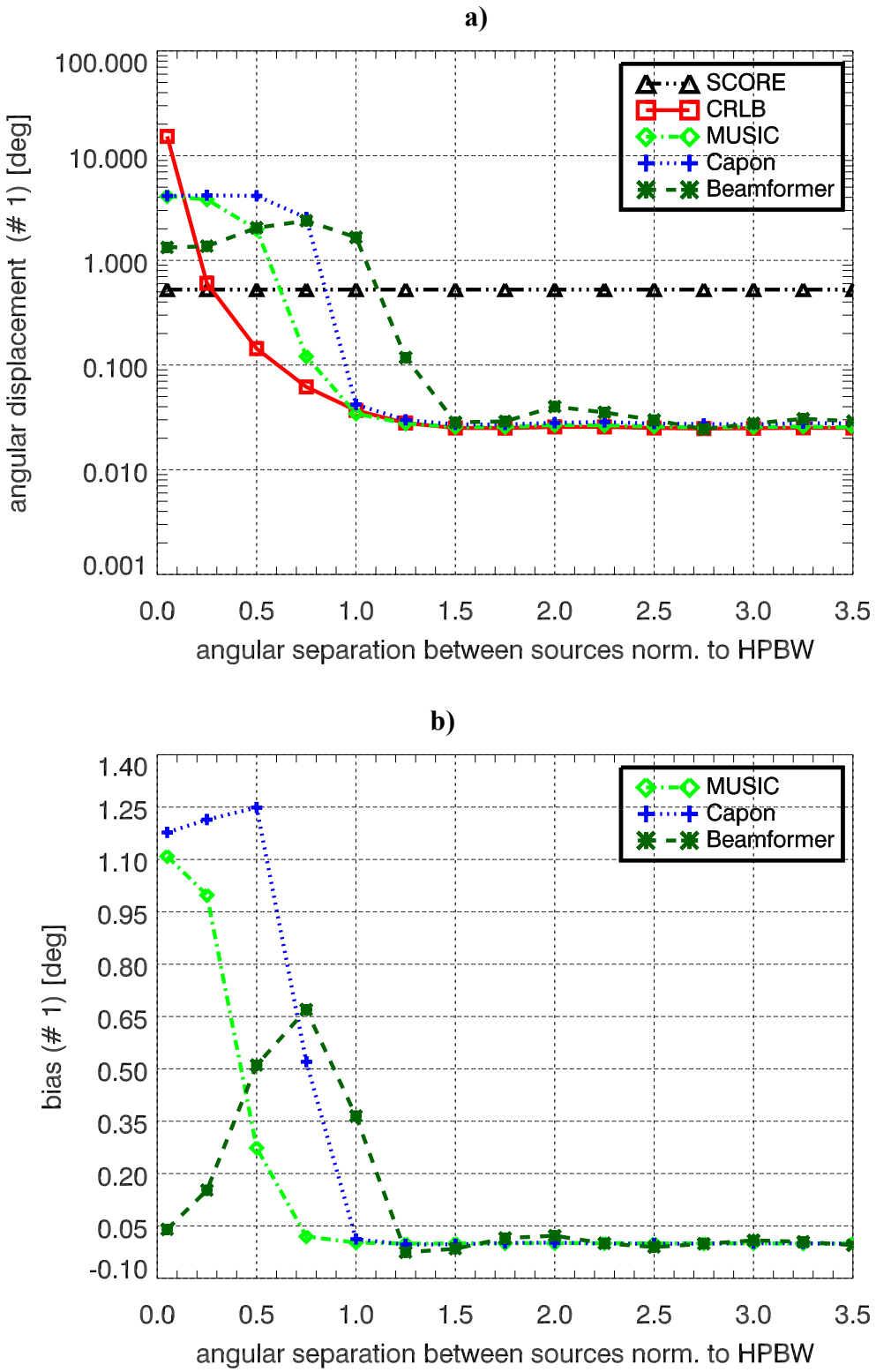

Figure 7-3: a) RMSE or angular displacement and **b)** bias on source #1 vs. angular separation between sources norm. to the antenna half power beamwidth (HPBW).

7.3.2 Topographic height

As it has been described in section 2.3.3, the presence of topographic height profiles degrades the performance of the conventional SCORE. Then, it is interesting to evaluate the adaptive approach in a specific scenario where the topographic height of both sources ($h_{1,2}$) is being varied from 0 km to 8 Km.

The ground location ($g_{1,2}$) of both sources is kept constant. Therefore, a variation on their respective DOAs exists: $30º \le \theta_1 \le 30.4º$ and $39.4º \le \theta_2 \le 39.9º$ for $0 \text{ km} \le h_{1,2} \le 8 \text{ km}$. The angular separation is kept almost constant (9 HPBW) and the first range ambiguity (source #2) is still located within the reference unambiguous DOA interval (UR).

These conditions justify the constant angular displacement of Beamformer and Capon as a function of the topography, see Figure 7-4 a). Both methods present a similar tendency, following the CRLB for the different height profiles since for such angular separation they provide the same performance as discussed in the previous scenario.

When a stringent spherical earth model (no topography) is considered, the conventional SCORE works without error. However, for elevation greater than 1 km its angular displacement (0.17º-1.42º) is more than one order of magnitude higher than the ADBF approach (0.025º). This is directly translated into a degradation on the acquisition gain ranging from -0.3 dB to -25 dB, Figure 7-4 b). It must be noted the dramatic increase on pattern loss of SCORE for a topography of 7 km. In this case the corresponding angular displacement ($\approx 1.24º$) is located in the vicinity of the first null of the receive pattern, see Figure 7-1.

One may think to consider a reference topographic height in the conventional SCORE to reduce the pointing error. Nevertheless, from Figure 7-4 it is clear that still high degradation can be obtained when high variations on the surface profiles exit. In the other hand, ADBF allows acquiring the echo of interest with almost the maximum gain independently on the elevation profiles.

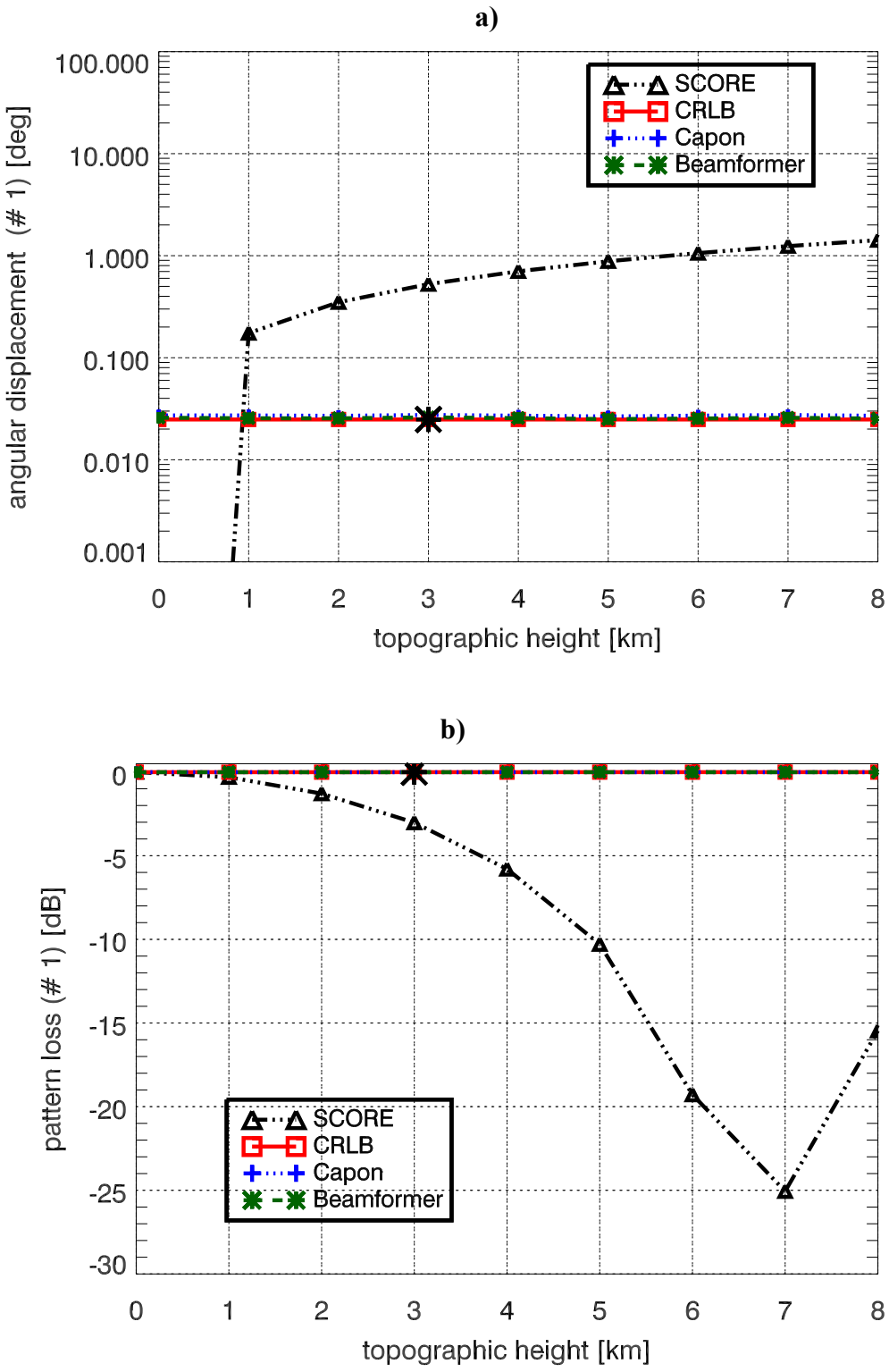

Figure 7-4: a) Angular displacement and **b)** pattern loss on source #1 vs. topographic height.

7.3.3 Ground position

According to [7], the displacement of SCORE, for a fixed height, weakly decreases for increasing ground location of the source[36]. In this specific scenario the ground position ($g_{1,2}$) of the two sources is varied along the imaged swath ($300\ \text{km} \le swath \le 370\ \text{km}$). The source #1 fixes implicitly the location of the second considering that the angular separation ($\approx 9 \cdot \text{HPBW}$) and the topographic height ($h_{1,2} = 3\ \text{km}$) are kept constant. Then, the ground variation implies also a DOA variation for both sources, i.e. $29.75º \le \theta_1 \le 35.06º$ and $39.20º \le \theta_2 \le 44.50º$.

The results obtained in Figure 7-5 are consistent with the described scenario. Since the angular separation between the sources is kept constant, Beamformer and Capon provide the same performance as before explained. The angular displacement for both presents almost a flat response (0.025º), decoupling the dependency of the estimation accuracy on the ground position. It is known that the array antenna provides better accuracy estimation to the DOA close to the *broadside* (tilt angle) than the ones coming from the *endfire* of the antenna [24]. This is explained due to the sinusoidal term $\sin(\beta - \theta)$ of the steering vector in Eq. (4.8). In this specific scenario the DOA variation respect to broadside of the antenna is in the order $\pm 2.5º$ for source #1. Thus, the sinusoidal term can be well approximated by its argument and it is not expected a variation on the accuracy estimation.

In any case, the ADBF outperforms the conventional SCORE for the different positions along the swath, considered the specific topography, with an improvement between 2 dB and 3 dB in the acquisition gain, see Figure 7-5 b).

It must be noted that for ground positions of source #1 $g_1 > 325\ \text{km}$, the second source DOAs are located out of the unambiguous DOA range (UR), $23.3º < \theta_{unamb} < 41.2º$. Since the estimation of the DOA is performed within this span, it is expected a degradation on the corresponding angular displacement for source #2. This is because the estimation of the second source, out of the UR, is associated to an ambiguous DOA that folds back in the mentioned interval. Then, the estimation of the source #2 DOA does not result reliable for the proper implementation of a possible null-steering technique for range ambiguity suppression [27].

[36] Ground position corresponds to the ground range distance from the satellite's nadir to the ground projection of the source on the Earth surface.

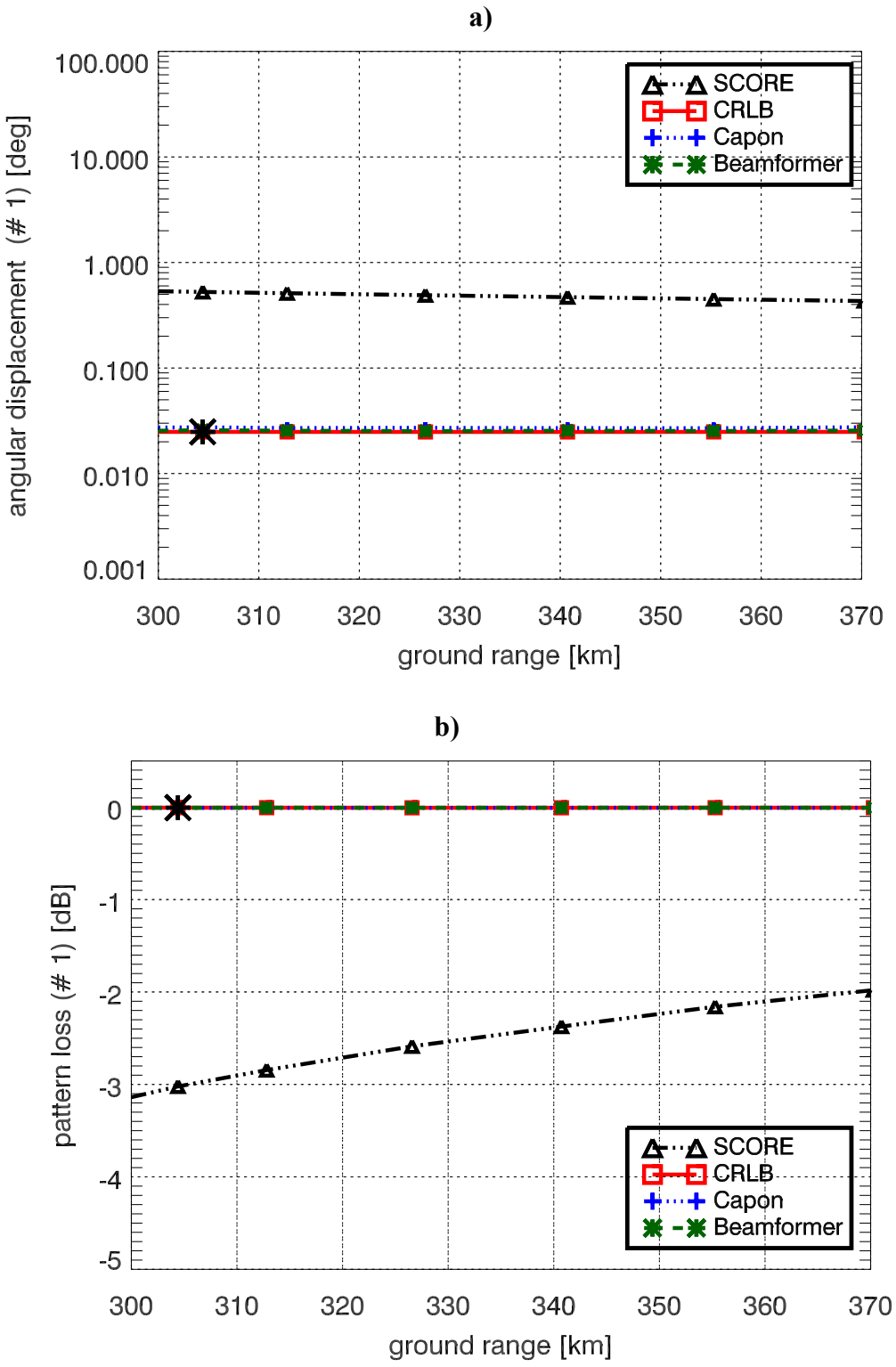

Figure 7-5: a) Angular displacement and **b)** pattern loss on source #1 vs. ground position of source #1 along swath.

7.3.4 Array Signal to Noise Ratio (ASNR)

This scenario takes into account how the performance of the ADBF is affected by the variation of the mean power level of the source of interest, i.e. the reflectivity of the first source α_1. It is evaluated in terms of Array Signal-to-Noise Ratio ($ASNR_1$), defined as $ASNR_1 = K \cdot \alpha_1 / \sigma_e^2$, keeping the $ASNR_2$ and the other system/scenario parameters constant.

From Figure 7-6 a), the angular displacement on the source #1 for the estimation methods and the CRLB decreases as the signal of interest strength increases, i.e. a better accuracy in the estimation is obtained; whereas the conventional SCORE presents a constant steering error since the angular displacement just depends on the acquisition geometry.

There exists a threshold effect on the performance of Beamformer and Capon at $ASNR_1 = 3$ dB, where both reach the CRLB. For $ASNR_1$ below this value there is a dramatic degradation on the performance of both methods. This can be easily understood through the associated gain loss ranging from -3 dB to -30 dB for this "noisy" environment, see Figure 7-6 b). The variability in the pattern loss in the interval $-18 \text{ dB} \leq ASNR_1 \leq -3 \text{ dB}$ is a consequence of acquiring the echo of interest with secondary lobes of the sharp receive pattern. Then, the ADBF obtain a better performance compared to SCORE for $ASNR_1 > 0$ dB with almost a constant 3 dB improvement in the PL.

It must be noted that this threshold effect depends on which is the angular separation between the sources and the $ASNR$. In this specific scenario both Beamformer and Capon have the same boundary value since the angular separation is well above the worse resolution capability of Beamformer. However, assuming a worse scenario, e.g. source separation $\approx 1 \cdot \text{HPBW}$ and $ASNR_2 = 9$ dB that can model a scenario with sources in layover, different threshold values exists as can be seen in Figure 7-7. For $ASNR_1 \geq 9$ dB Capon reaches the CRLB since the estimated spectrum presents two clear peaks associated to the different sources. However, the corresponding angular displacement of Beamformer does not achieve the CRLB when increasing the $ASNR_1$. This is because for such angular separation Beamformer is not able to distinguish two differentiated peaks in the spectrum and the influence of secondary lobes associated to the second source produces this difference w.r.t. the CRLB.

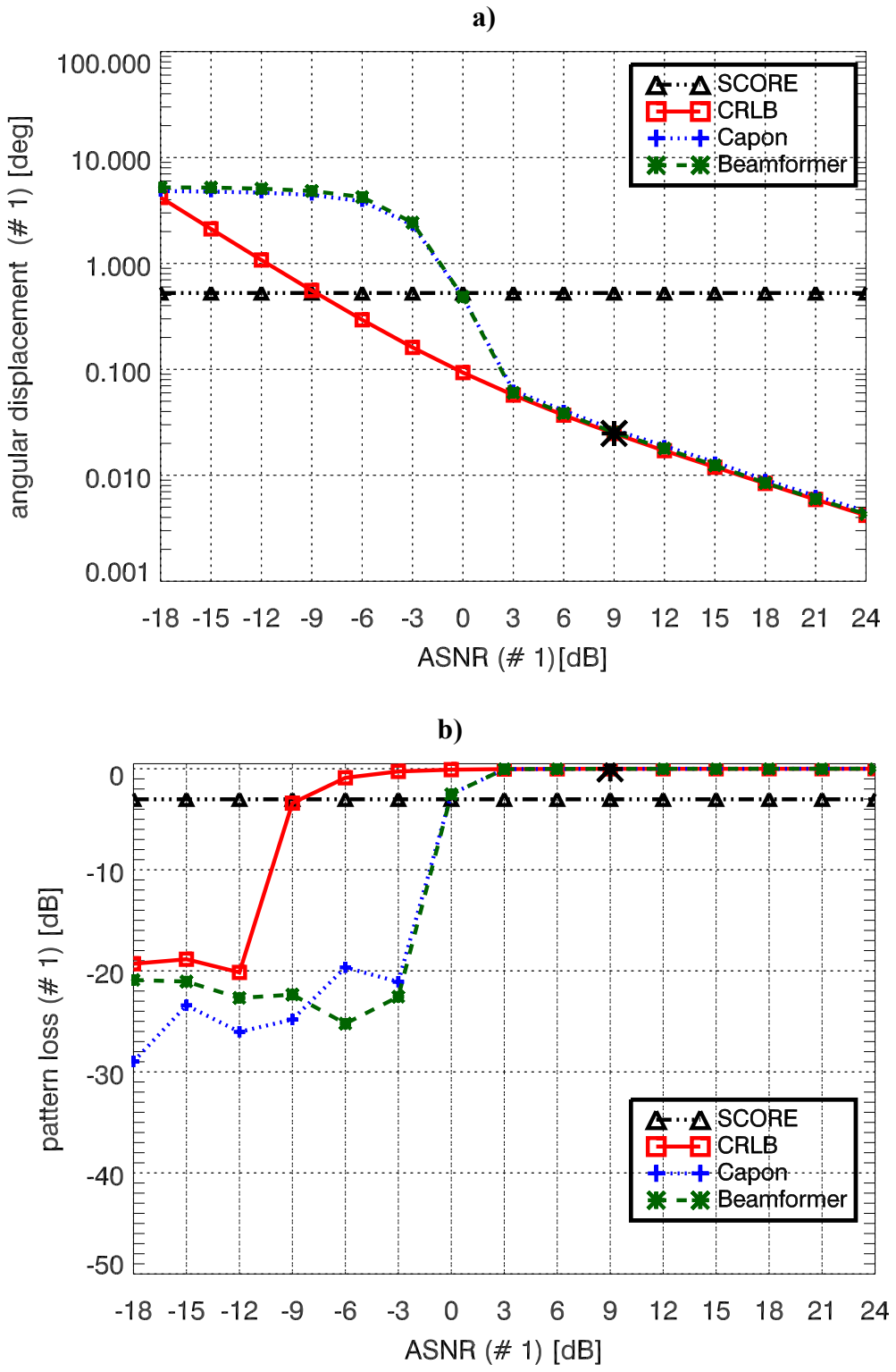

Figure 7-6: a) Angular displacement and **b)** pattern loss on source #1 vs. $ASNR_1$ with $ASNR_2 = 3$ dB constant and angular separation ≈ 9 HPBW .

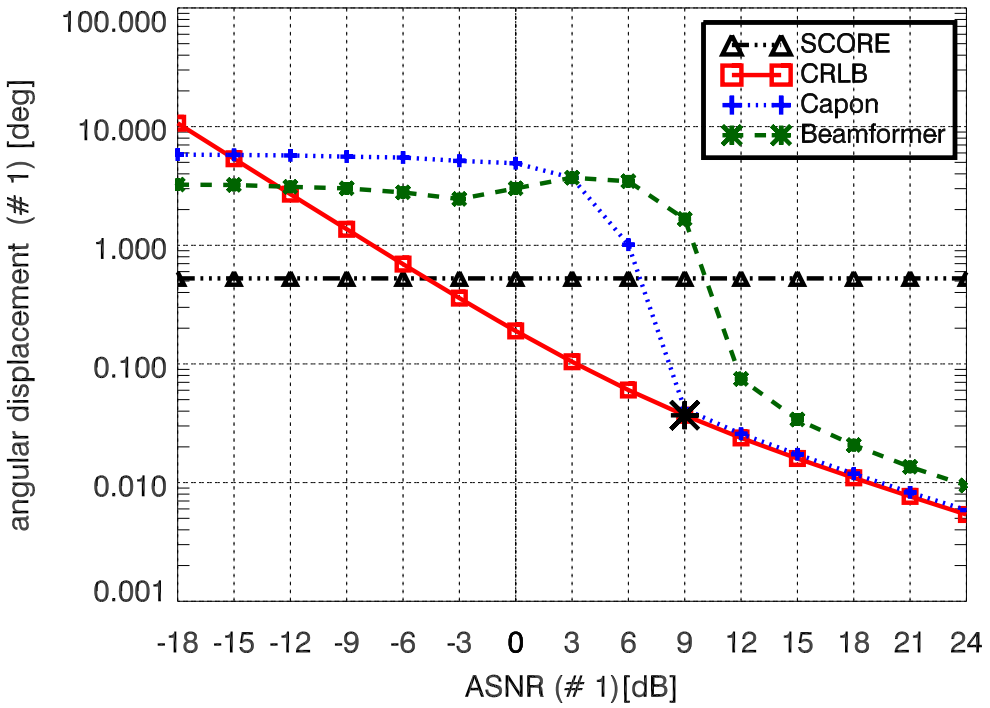

Figure 7-7: Angular displacement on source #1 vs. $ASNR_1$ with $ASNR_2 = 9$ dB constant and angular separation ≈ 1 HPBW.

7.3.5 Receive antenna geometry

In SAR systems, specially the spaceborne case, there are not too many degrees of freedom in the design of the antenna. Instrument parameters as dimension of the antenna and number of sub-apertures (elements) are bound by physical/economical constrains and strongly affect the complexity of the ADBF itself.

In this section three different scenarios regarding the receive antenna configuration are analyzed. In the two first, the performance of the ADBF and SCORE are evaluated as a function of the antenna height, considering constant inter-element spacing in one case and constant number of elements in the other. Finally, the third scenario studies the impact of the number of sub-apertures keeping the antenna height constant.

In all three scenarios the $ASNR_{1,2}$ are maintained as the reference one, adjusting the power transmit requirements to this end. It must be noted that the correlation of the speckle between the different sub-apertures also changes from one scenario to another according to the definition given in Eqs. (5.6) and (5.7). However, for the HRWS SAR system the critical antenna height is in the order of several or tens of kilometers (annex A.3). Then, the speckle is almost completely correlated along the different sub-apertures.

7.3.5.1 Antenna height (constant spacing)

The increase on the antenna height is accomplished through the addition of higher number of elements or sub-apertures. In this scenario the angular sector of unambiguous DOA (UR) keeps $23.3º < \theta_{unamb} < 41.2º$ (w.r.t. nadir) since the inter-element spacing between adjacent sub-apertures in elevation is not modified, $d = 0.1$ m.

From Figure 7-8 a), the angular displacement for Beamformer and Capon tends to decrease as the total receive aperture increases, following the CRLB. The lower the number of elements K (smaller the antenna height) the lower is the resolution capabilities of the estimation methods. However, both provide the same performance since the angular separation between the sources ($\approx 9º$) is still well above the lower resolution capability of Beamformer (HPBW $\approx 4º$ for antenna height of 0.4 m).

Increasing K allows higher resolutions, but a worse estimation of the covariance matrix is obtained. Then, a degradation on the performance accuracy for the methods is obtained. This effect is more evident in the case of Capon algorithm since is formulated as a "data-dependent" spatial filter which requires from the computation of $\hat{\mathbf{R}}_y^{-1}$. The existence of such an inverse is restricted to values $N \geq K$, [44]. Therefore, in situations where the number of sub-apertures is in the same order as the snapshots N, a worse performance of Capon compared to Beamformer is expected.

From the angular displacements in Figure 7-8 a), the ADBF approach provides better results than conventional SCORE for the different antenna configurations. From Figure 7-8 b), the improvement in terms of pattern loss ranges from 0.2 dB to 5.8 dB since the constant steering SCORE error is translated into an increase of PL as the synthesized beam pattern becomes narrower.

The results obtained in this scenario suggest that with a lower number of elements it is also possible to obtain still a good performance relative to SCORE, e.g. 4 elements. It would be interesting to use just the signal from a reduced number of elements ($K < 15$) keeping the reference configuration/architecture of the antenna, i.e. $H_a = 1.5$ m with 15 sub-apertures. Thus, the system power requirements and the associated Range-Ambiguity-to-Signal Ratio (RASR) performance are not modified. Moreover, the computational cost of the ADBF is reduced since lower number of range lines should be compressed and less memory demand is required. However, the results obtained in this scenario consider constant $ASNR_i = K \cdot \alpha_i / \sigma_e^2$ and so a variation on the transmit power. Then, to evaluate the possibility of activating just some of the channels to estimate the DOA it has been analyzed the same scenario but keeping constant the $SNR_{1,2}$ at each sub-aperture as in the reference antenna configuration.

From Figure 7-9 a), where the previous conditions are considered, the angular displacement on source #1 increases for Beamformer and Capon, especially for a number of sub-apertures below 8. For higher antenna sizes and number of elements, the tendency is quite similar to the case analyzed in Figure 7-8. Therefore, the ADBF steering direction could be estimated using a low number of elements; then, the sharp beam can be synthesized through the whole receive antenna ($H_a = 1.5$ m, $K = 15$) so that the antenna gain does not change. For $K = 4$ the angular displacement is in the order of 0.22º and the PL is still negligible, see Figure 7-9 b). In this case the PL associated to SCORE is constant since the receive pattern is generated using the same antenna reference configuration ($H_a = 1.5$ m, $K = 15$).

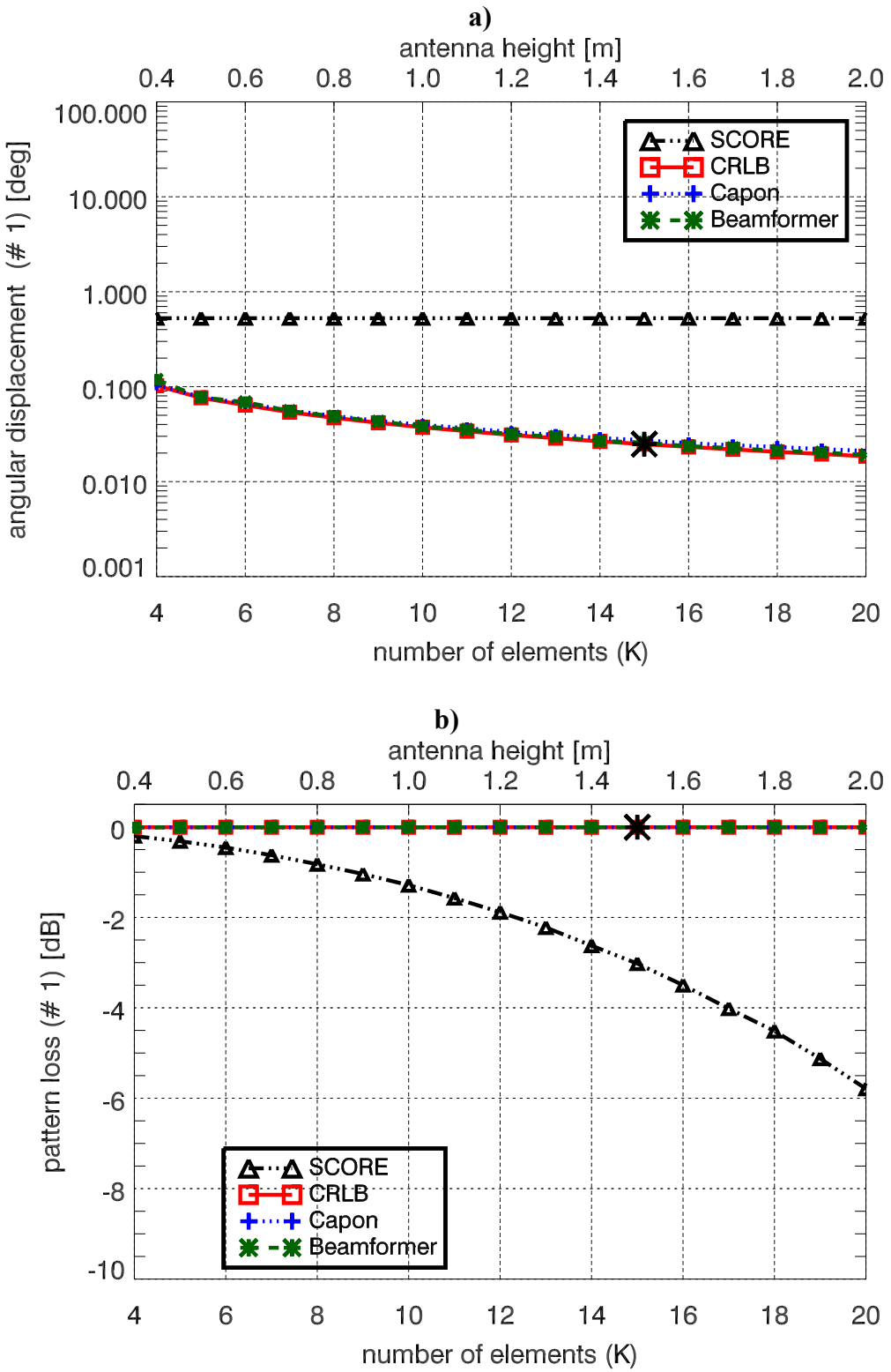

Figure 7-8: a) Angular displacement and **b)** pattern loss on source #1 vs. antenna height ($d = 0.1$ m and constant $ASNR$).

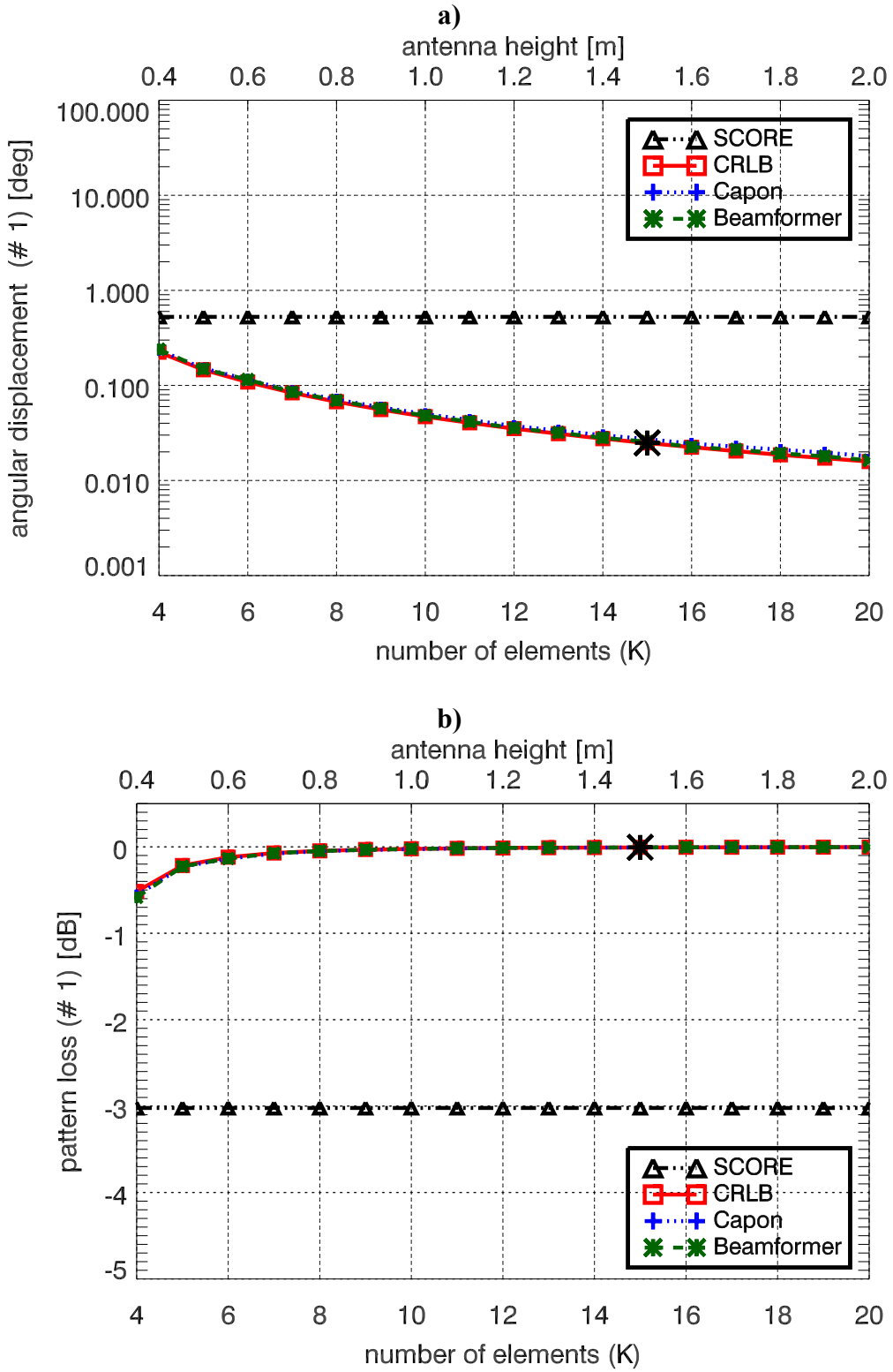

Figure 7-9: a) Angular displacement and **b)** pattern loss on source #1 vs. antenna height ($d = 0.1$ m and $ASNR$ varies). Receive sharp beam synthesized using the whole antenna ($H_a = 1.5$ m, $K = 15$).

7.3.5.2 Antenna height (constant number of elements)

In this scenario the antenna height is varied between the same values as in the previous case, but the total number of sub-apertures $K = 15$ is fixed and consequently the inter-element spacing d changes. The reference $ASNR_{1,2}$ is also kept constant.

It must be noted that the height of each sub-aperture is changed accordingly to the inter-element spacing. Then, as mentioned in section 2.2, the dimension of each sub-aperture should be equal or smaller to the transmit antenna dimension ($H_{tx} \approx 16 \cdot \lambda$) in order to cover the imaged swath. This requirement is fulfilled in the analysis here considered from Figure 7-10, where the associated inter-element spacing in terms of the wavelength is labeled in a second axis.

Comparing the angular displacement for Beamformer and Capon in Figure 7-10 a) with the previous scenario in Figure 7-8 a), they have a common trend. Under the same total antenna height variation, which determines the resolution of methods, and the same $ASNR$ conditions it is expect a similar behavior in the angular displacement.

The associated pattern loss has also the same tendency as in the previous section. It is known that the respective receive patterns generated in these two scenarios are different; position of the grating lobes and number of sidelobes distinguishes them. However, the null-to-null mainlobe width is the same for both approaches. Then, as in both cases the mean error in the estimation given by the angular displacement is similar, an analogous PL is obtained. The same justification arises for conventional SCORE, where the error is constant.

This invariance w.r.t. the previous scenario confirms that $K = 15$ provides redundant information and suggests the possibility of using a sub-set of the available number of sub-apertures as it has been discussed in the previous section.

It must be noted that in this specific scenario a variation of the unambiguous DOA range (UR), $(\beta - \arcsin(\lambda/2d), \beta + \arcsin(\lambda/2d))$, exists since the inter-element spacing also changes. Increasing d, this unambiguous interval decreases and for values of the antenna height greater than 1.8 m the second source is located out of the unambiguous interval. From Figure 7-11 this situation is translated into a high degradation on the angular displacement of the second source ($\approx 14^\circ$), affected by a strong bias in the same order. This is because the peak detection has been performed within the UR; then, the estimate of source #2 is associated to an ambiguous DOA that folds back within this span $(25.5^\circ, 38.9^\circ)$, see Figure 7-12, where the estimated spectrum of Beamformer and Capon are represented for $H_a = 2.0$ m.

Then, one may think to reduce the total height of the antenna in order to cover a higher spatially unambiguous sector, e.g. with an antenna of 0.4 m the corresponding interval is $-3.37^\circ < \theta_{unamb} < 67.87^\circ$ (measured w.r.t. nadir). However, the radiometric resolution will be worse and the different sub-apertures will be closely located in the array, which in real conditions can be translated into an increase of the coupling effect and a degradation of the estimation performance [34].

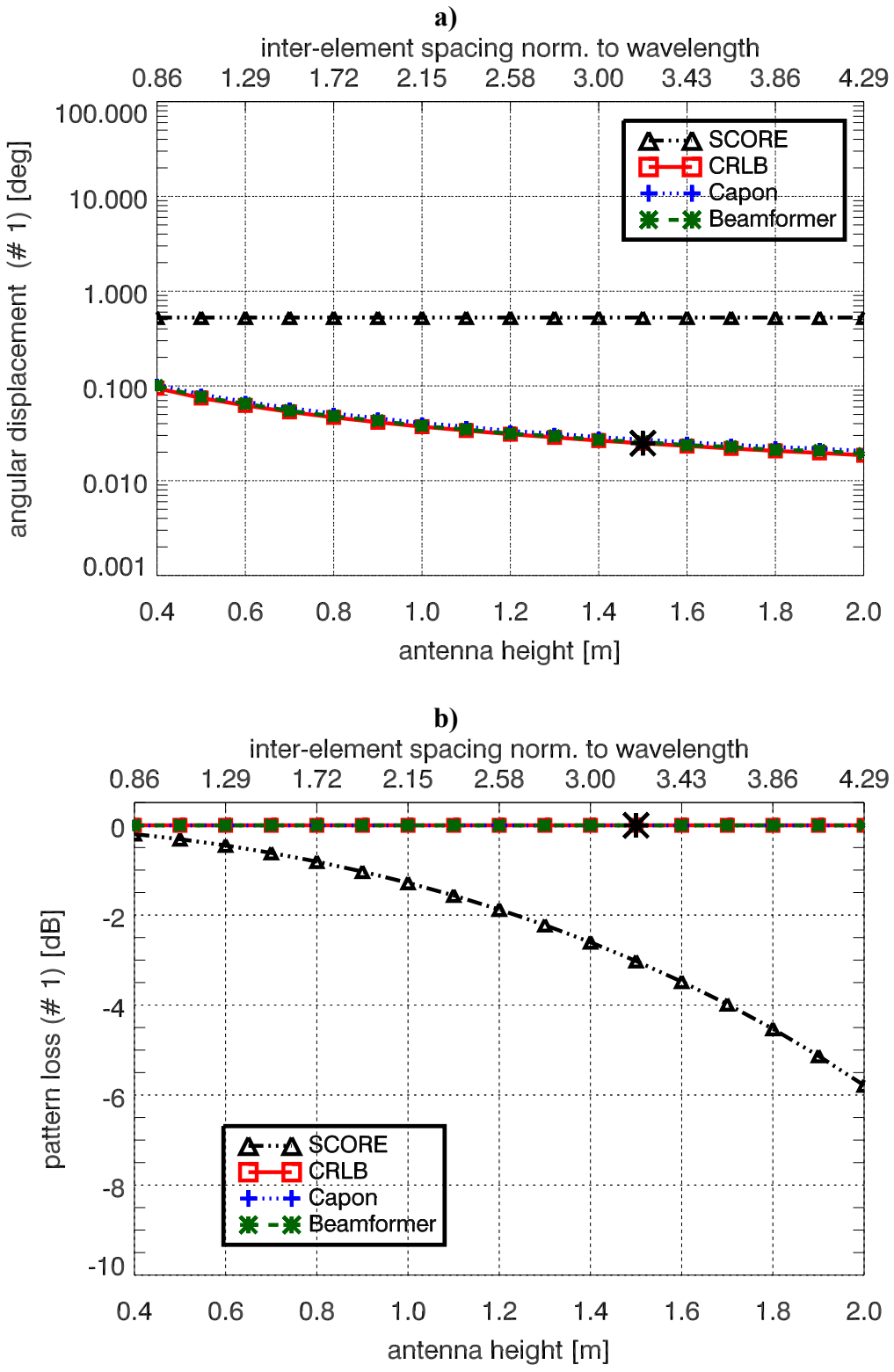

Figure 7-10: a) Angular displacement and **b)** pattern loss on source #1 vs. antenna height ($K = 15$ and constant $ASNR$).

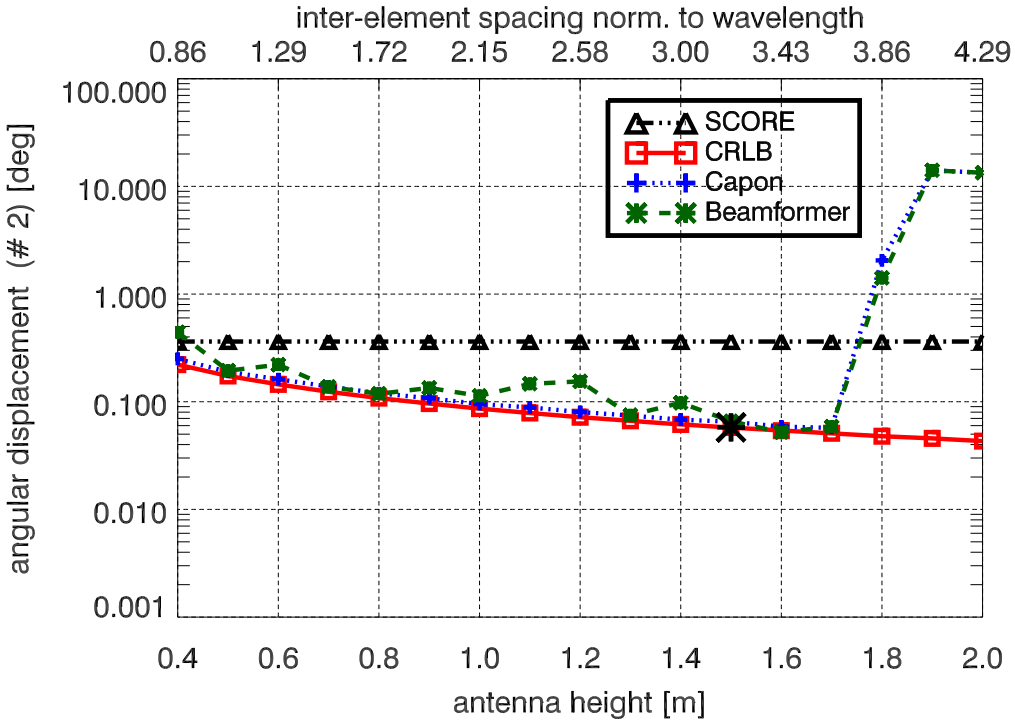

Figure 7-11: Angular displacement on source #2 vs. antenna height ($K = 15$ and constant $ASNR$)

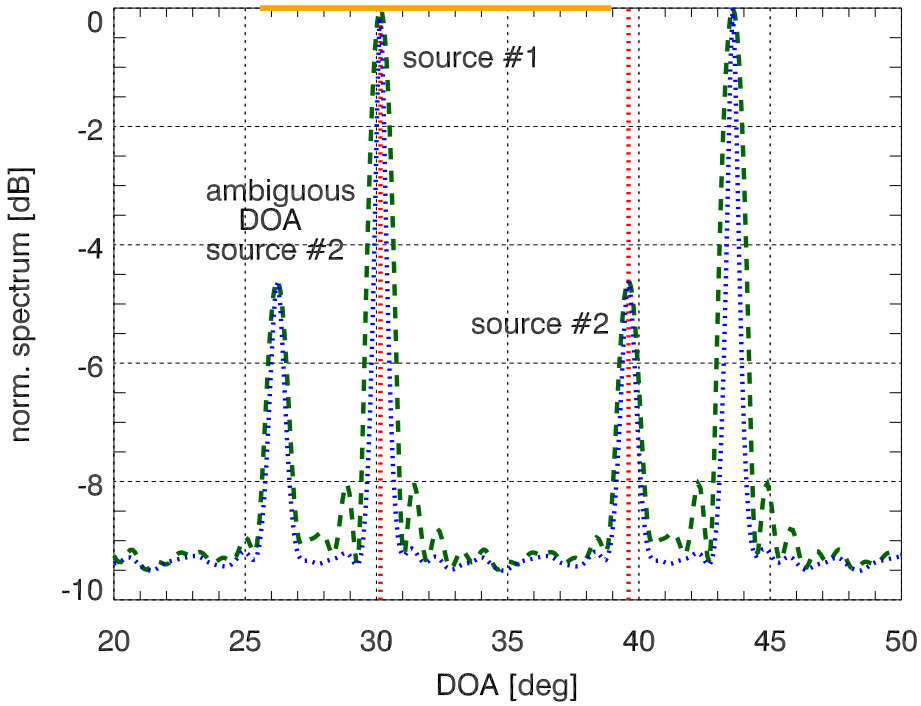

Figure 7-12: Normalized spectrums Beamformer (green dashed curve) and Capon (blue dotted curve) averaged over 100 trials, for $H_a = 2.0$ and $K = 15$ (orange solid line indicates UR and red dotted lines true DOAs).

7.3.5.3 Number of elements (constant antenna height)

The total number of channels or sub-apertures is a complexity driver in the overall design of the SAR systems, especially in the spaceborne case. Increasing the number of sub-apertures in elevation implies a higher number of receive modules, radio frequency (RF) chains and Analog to Digital Converters (ADC) for each channel. Therefore, the associated cost also constitutes an important effort. Moreover, the ambiguity requirements, in terms of RASR [14], are also affected by the total number of elements in elevation.

In this scenario it is analyzed how this variation of sub-apertures, keeping the total height of the antenna, affects the performance of the ADBF. A constant antenna height allows maintaining the radiometric resolution. However, the inter-element spacing d changes and so the UR.

Figure 7-13 a), where the angular displacement is represented as a function of the number of elements, illustrates the effect of reducing the unambiguous DOA interval. For a number of sub-apertures below 13, the true DOA of the source #2 is out of the corresponding UR. For 4 and 8 elements, the location of the second source is such that almost overlaps with ambiguous DOAs associated to the first source. In Figure 7-14, the estimated Beamformer and Capon spectrums are presented for the 4 elements antenna configuration, where the peak corresponding to the true DOA of source #2 coincides almost with a periodic peak of the first source.

For the CRLB, there exists a strong degradation with $K = 4$ and 8 because the corresponding steering vectors of the two sources are almost linearly dependent and the CRLB is not well conditioned [41]. Thus, numerical problems exist and this justifies the peak response for the CRLB. These cases are completely analogous to having closely spaced sources, see Figure 7-3.

It must be noted that for these situations on the CRLB, its corresponding steering directions, i.e. $\theta \pm sqrt(CRLB)$, are such that the maximum of the receive pattern is not located at these directions but at an associated grating lobe. This is due to the steering of the array factor (green dotted curve) affected by the corresponding sub-aperture pattern (red dashed curve) as can be seen in Figure 7-15. The PL has been computed in accordance with this situation, i.e. respect the maximum of the receive pattern.

For Beamformer and Capon the angular displacement (or RMSE) is slightly affected by the superposition of the two peaks in the estimated spectrums[37]. This is due to the association algorithm (sorting estimates) used after the peak detection to compute the corresponding RMSE, section 4.4. Therefore, the strong unique peak within the unambiguous DOA range is associated to the source #1, whereas the second source is alternatively associated to noisy peaks within this interval.

[37] The overlap of the peak associated to the second source introduces a small bias (-10^{-2} degrees) in the DOA estimation of the signal of interest (source #1).

Beamformer and Capon associate the highest peak in the estimated spectrum to the signal of interest. Thereby, in this situation, the ADBF would steer towards the DOA associated to the unique highest peak in the estimated spectrum, which is slightly biased from the actual echo DOA due to the influence of the overlapped ambiguous peak.

From Figure 7-13 a), the angular displacement of ADBF, for both Beamformer and Capon, is almost non-sensitive to the variation of the number of elements and below conventional SCORE. Then, it could be considered a different configuration of the receive antenna, i.e. lower number of sub-apertures in order to reduce the technological/economical effort. Moreover, the ADBF approach would save memory requirements and complexity as lower number of range lines should be compressed.

For a 4 elements configuration antenna, the unambiguous DOA range is reduced to $29.8º < \theta_{unamb} < 34.6º$. Taking into account the swath/subswath of interest ($300\ \text{km} - 370\ \text{km}$) and different topographic heights ($0\ \text{km} - 8\ \text{km}$), the potential DOA interval of interest ($29.6º \leq \theta_{swath} \leq 35.3º$) is not covered by the former range. Moreover, there is a degradation on the RASR[38] performance, which is below -16 dB within the swath of interest compared to -30 dB for the reference system.

A 10 sub-aperture antenna can be considered a better choice since in terms of RASR its value is below -25 dB not only for the subswath of interest but for the whole swath that HRWS SAR system should cover ($170\ \text{km} - 557\ \text{km}$). For this configuration, the associated interval of unambiguous DOA ($26.3º < \theta_{unamb} < 38.2º$) allows embracing the subswath of interest.

[38] The values here presented have been computed according to conventional SCORE for no topography in the terrain [6]. Though not strictly valid for the ADBF RASR performance, these results can be useful to discard some antenna configurations.

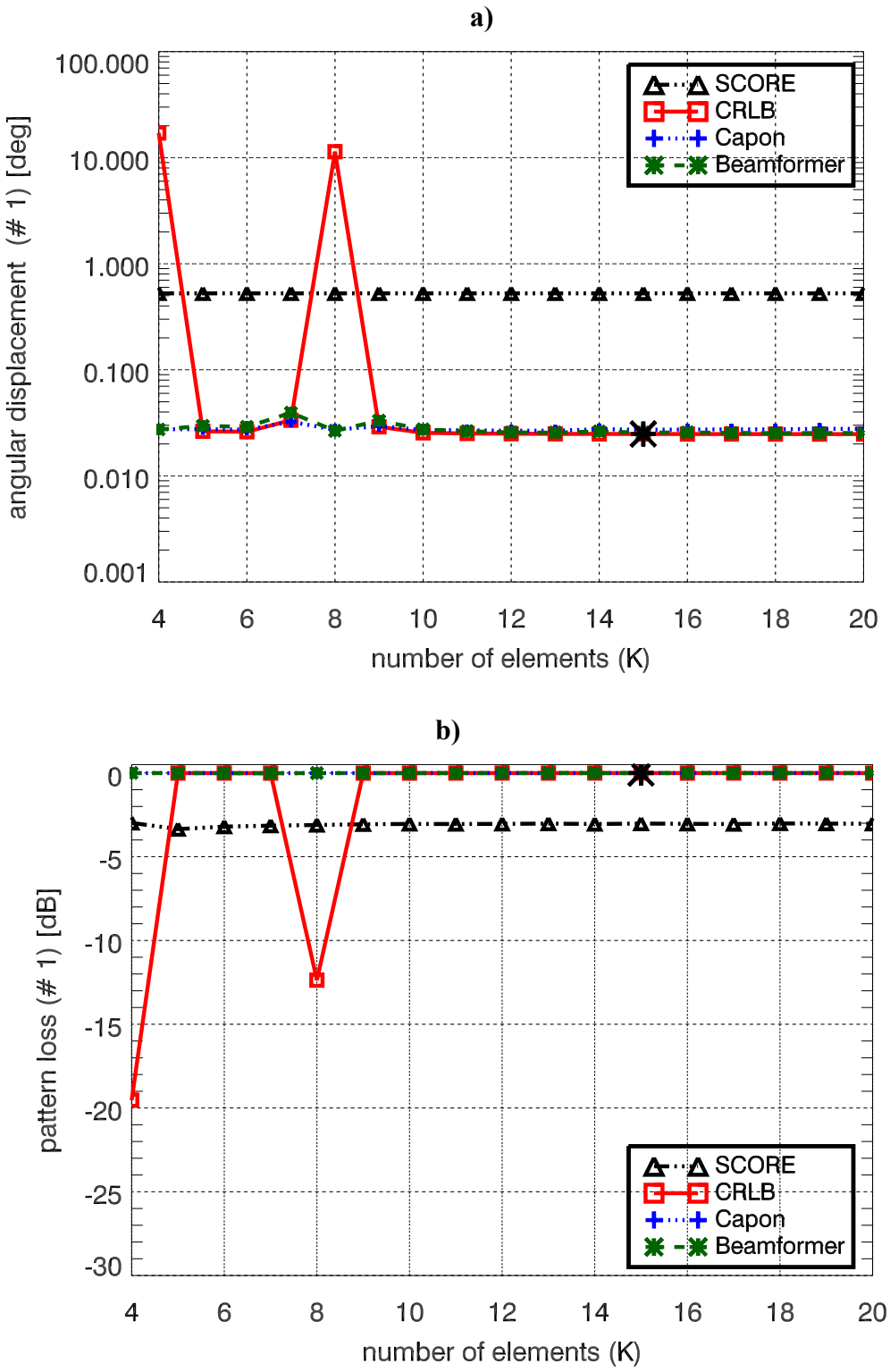

Figure 7-13: a) Angular displacement and **b)** pattern loss on source #1 vs. number of elements K, keeping total antenna height of $H_a = 1.5$ m.

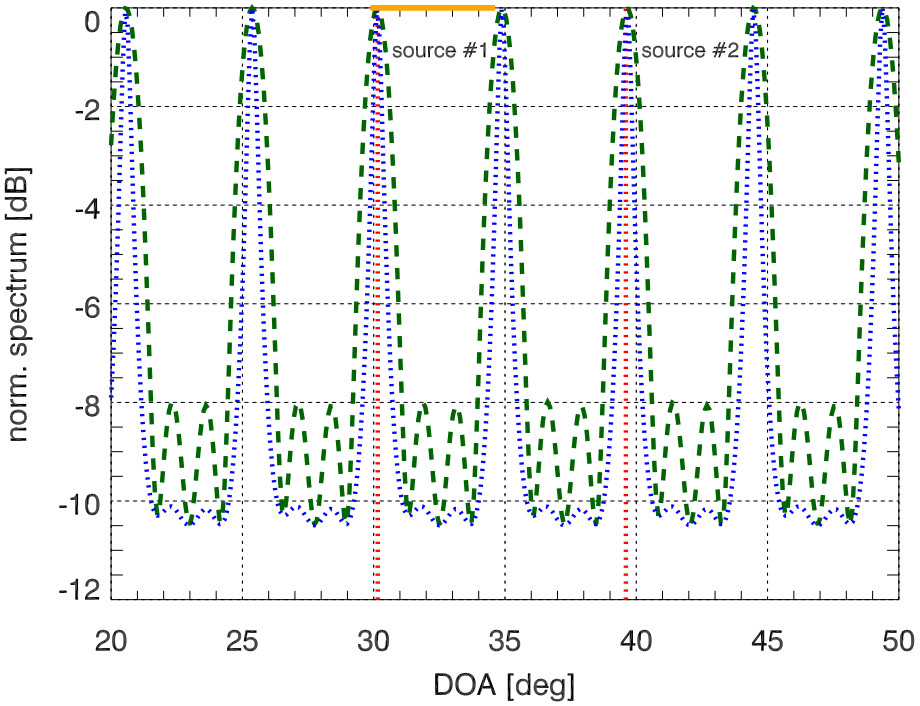

Figure 7-14: Normalized spectrums of Beamformer (green dashed curve) and Capon (blue dotted curve) vs. DOA, averaged over 100 trials. $H_a = 1.5$ m with $K = 4$ sub-apertures (orange solid line indicates UR and red dotted lines true DOAs).

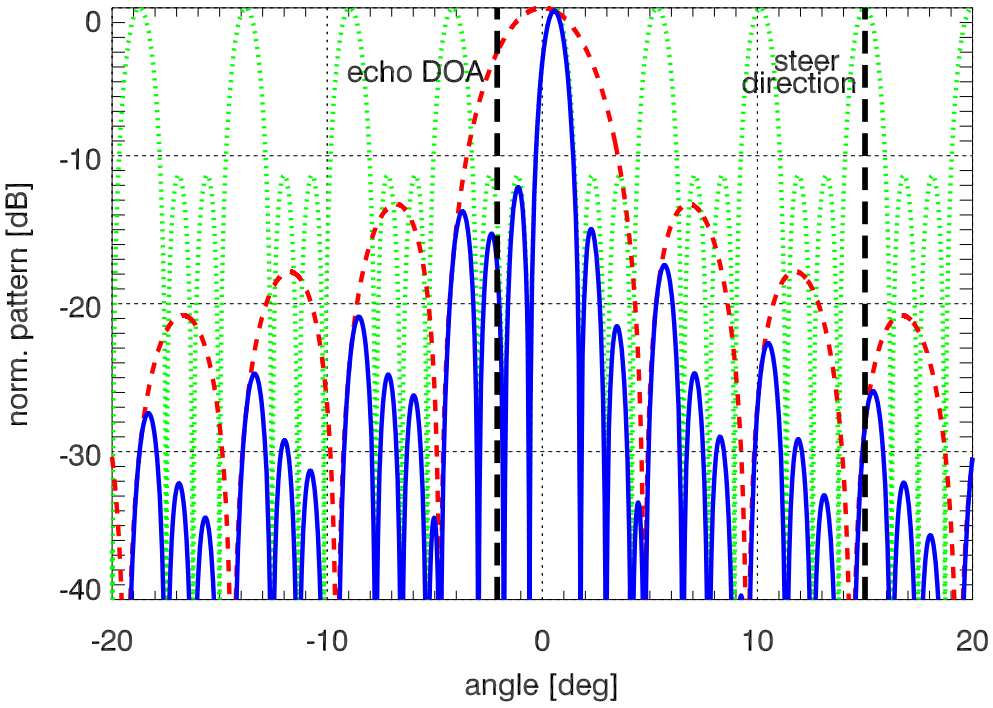

Figure 7-15: Receive elevation pattern (blue solid curve) for $H_a = 1.5$ m and $K = 4$ vs. angle w.r.t. broadside. Steering direction $\theta + sqrt(CRLB)$; array factor (green dotted curve) and element pattern (red dashed curve).

7.3.6 Speckle decorrelation

This scenario analyses the effect of the speckle decorrelation along the antenna for the first source. As described in section 5.1, the normalized antenna height controls the level of decorrelation at the extreme phase centers of the receive aperture. Then, the normalized antenna height H_1 is varied from 0 (complete correlation) to 1 (total decorrelation) through different values of the local slope for the source #1, see annex A.3.

From Figure 7-16 a), the angular displacement for Beamformer and Capon increases departing from the CRLB. This degradation on the accuracy estimation can be explained due to the multiplicative characteristic of the speckle. This noise adds a random complex phase, uniformly distributed (*Swerling I* model [22]), to the signal at the different sub-apertures. Moreover, these narrowband estimation methods relay on the phase difference between the sub-apertures to retrieve the DOA, i.e. on the correlation between the different channels. This additional phase term can be interpreted as a "calibration" error of the steering vectors, which contain this phase information. Then, as the speckle decorrelates the phase information between the different sub-apertures becomes less reliable to obtain an accurate estimation.

In section 5.1, the theoretical spatial PSD is a *sinc*-like function, whose mainlobe width is controlled by the normalized antenna height. Then, increasing the value of H_1, the mainlobe associated to source #1 becomes wider. The estimated spectrums in Figure 7-17 illustrates this broadening effect on the peaks related to the first source, when considering the two extreme cases. Therefore, it becomes more difficult to estimate accurately the location of the peak, justifying the degradation on the performance.

In any case, the angular displacement experimented by the ADBF approach keeps still below the conventional SCORE (0.35º below in the worst case), which allows to approximately maintain the 3 dB improvement in the PL, Figure 7-16 b).

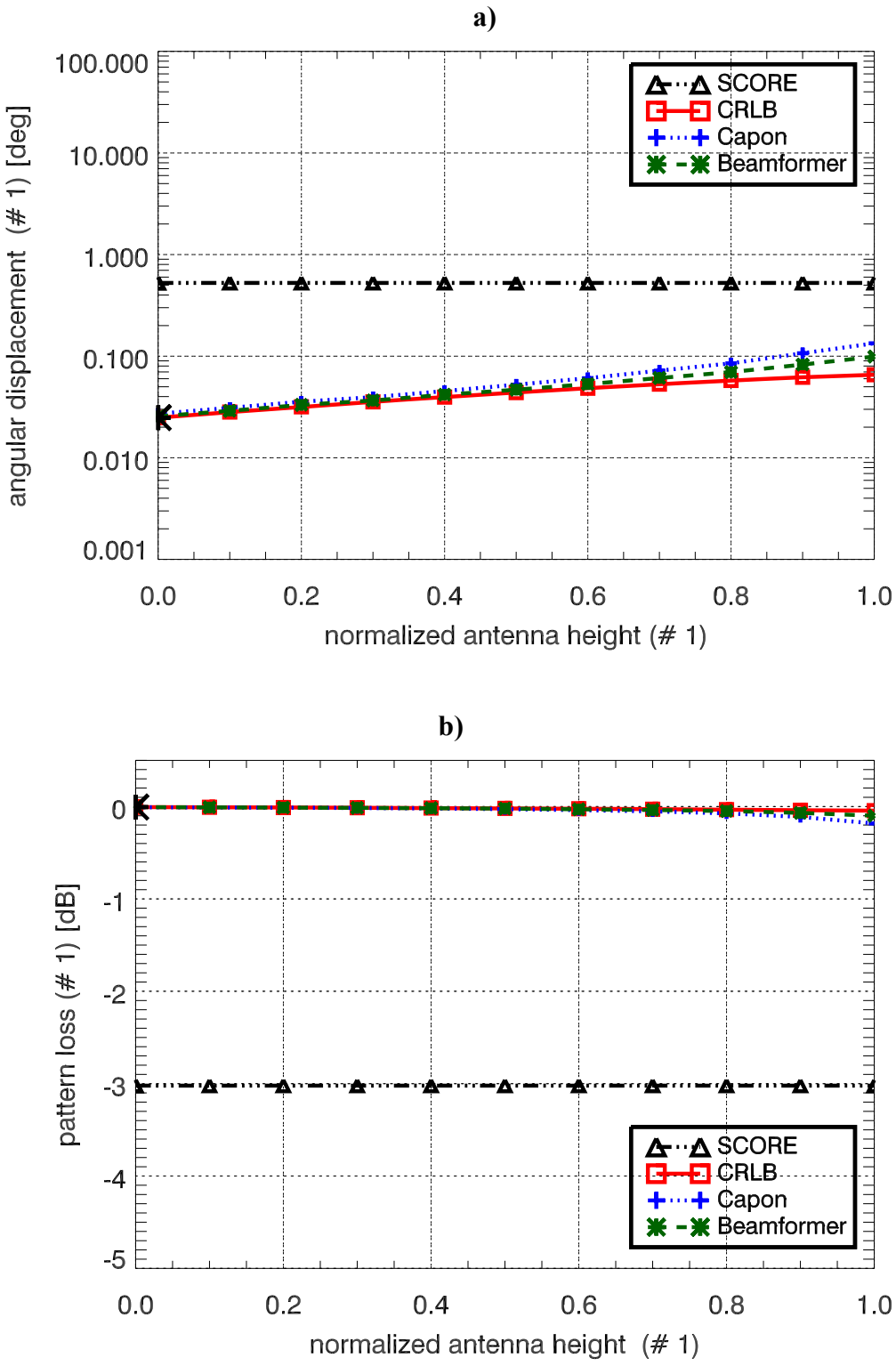

Figure 7-16: a) Angular displacement and **b)** pattern loss on source #1 vs. normalized antenna height of source #1.

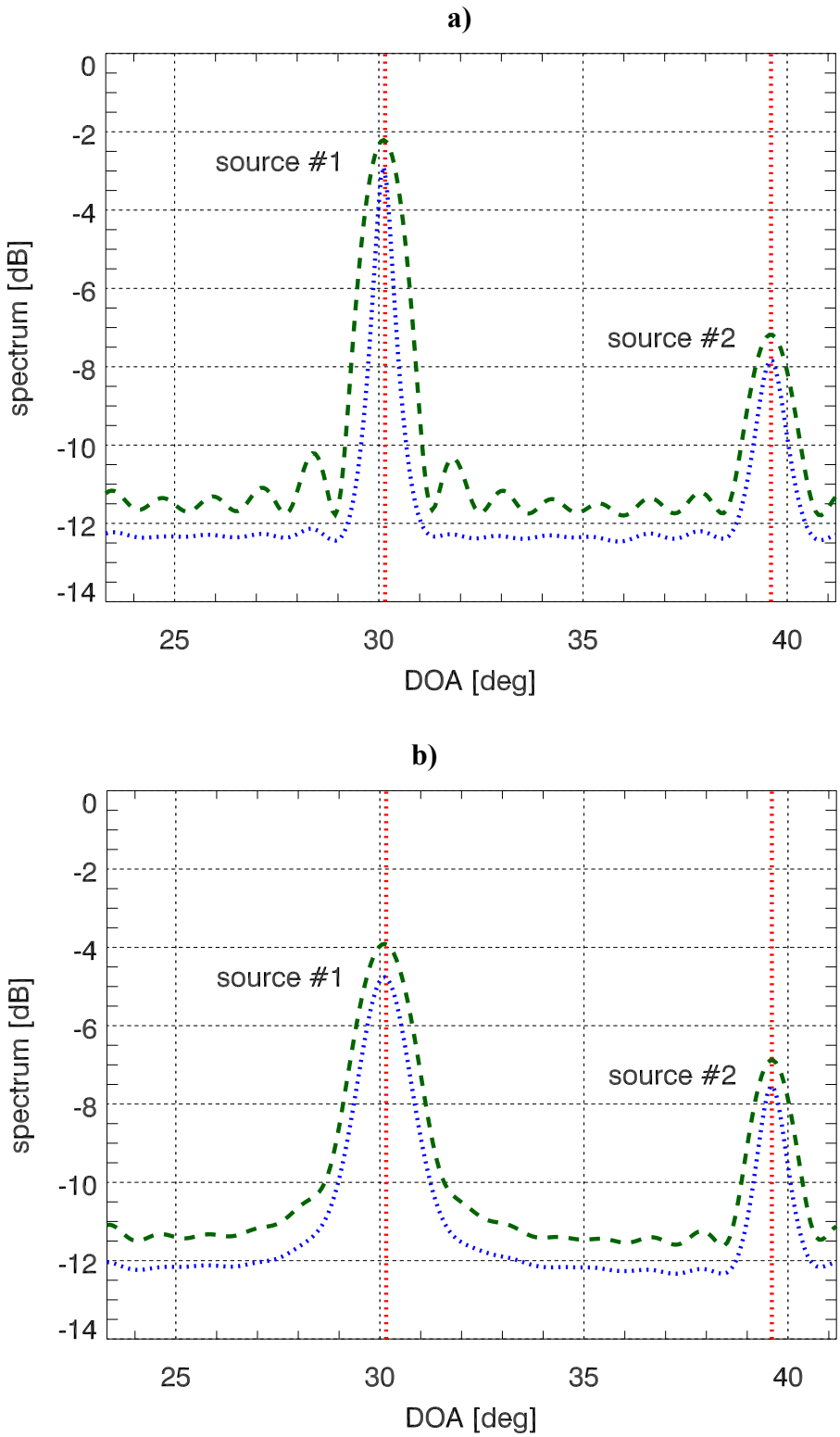

Figure 7-17: Beamformer (green dashed curve) and Capon (blue dotted curve) spectrums vs. DOA, averaged over 100 trials, for **a)** $H_1 = 0$ and **b)** $H_1 = 1$.

7.3.7 Number of snapshots

Beamformer and Capon require from the estimation of the spatial covariance matrix $\mathbf{R}_{\mathbf{y}}$ to retrieve the corresponding DOA. This matrix should be estimated from the available set of samples at the output of the different sub-apertures. In this scenario is analyzed the effect of the total number of snapshots on the efficiency of the ADBF approach.

In the model here considered, the different N samples correspond to subsequent azimuth acquisitions. The total number of these observations is limited by the related DOA variation and RCM (annex A.2). Values of $N < 72$ allows neglecting both effects.

In Figure 7-18 a), the angular displacement on source #1 for Beamformer and Capon decreases following the CRLB[39] as the number of snapshots increases, since more accurate is the estimation of the covariance matrix. Both methods provide almost the same performance, whose improvement is not so significant when the number of samples is higher. This is mainly due to the fact that source #1 is far from the influence of the second source and with higher $ASNR$, which makes the detection of the associated peak accurate. Figure 7-19 illustrates these effects on the angular displacement trend when considering a worse scenario (angular separation $1 \cdot \mathrm{HPBW}$ and same $ASNR$). In this situation, the Beamformer performance has a floor since the sources are separated below its resolution capability.

From Figure 7-18 a), the angular displacement of Capon is slightly greater than in Beamformer for snapshots below 40, because the former one is based on the computation of the inverse of the estimated covariance matrix, $\mathbf{R}_{\mathbf{y}}^{-1}$. Then, when N is in the order of the number of sub-apertures $K = 15$, the inversion is not so accurate. For values of $N < K$, the finite sample effects lead to a high variation between the eigenvalues of the covariance matrix, which is translated into numerical problems in the matrix inversion. In those cases, the *Diagonal Loading* (DL) technique can alleviate this effect to obtain a robust inversion of the matrix [26],[50].

The ADBF outperforms the conventional SCORE for any number of snapshots, with a constant improvement of 3 dB in the pattern loss, Figure 7-18 b). Then, increasing the total number of snapshots above the reference scenario $N = 50$ do not provide a substantial gain, but the associated computational effort increases as higher number of range lines should be compressed.

[39] From the general definition of the CRLB its angular displacement decreases as the square root of the number of snapshots.

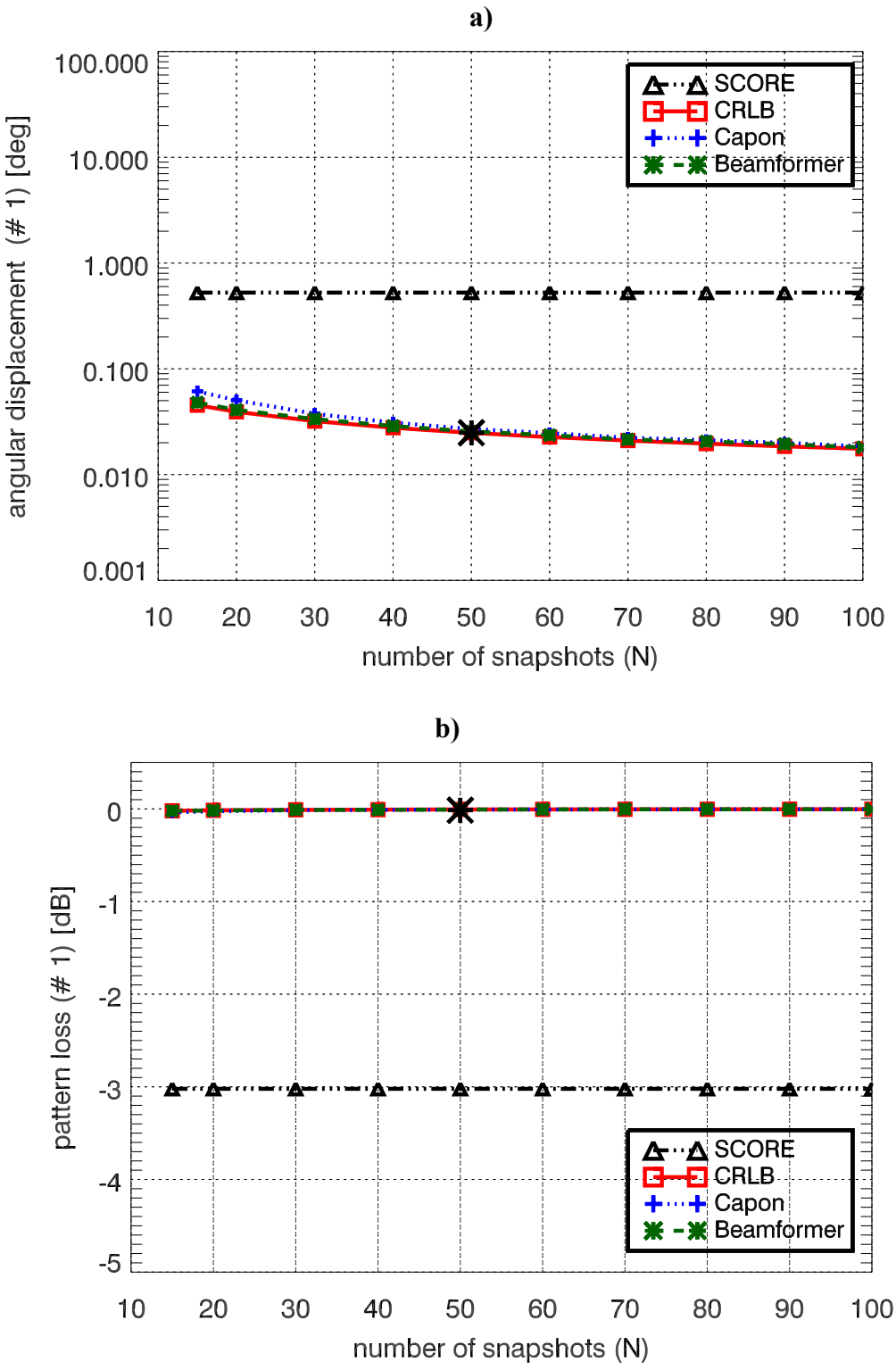

Figure 7-18: a) Angular displacement and **b)** pattern loss on source #1 vs. number of snapshots. $ASNR_{1,2} = [9\text{ dB}, 3\text{ dB}]$ and separation between sources ≈ 9 HPBW

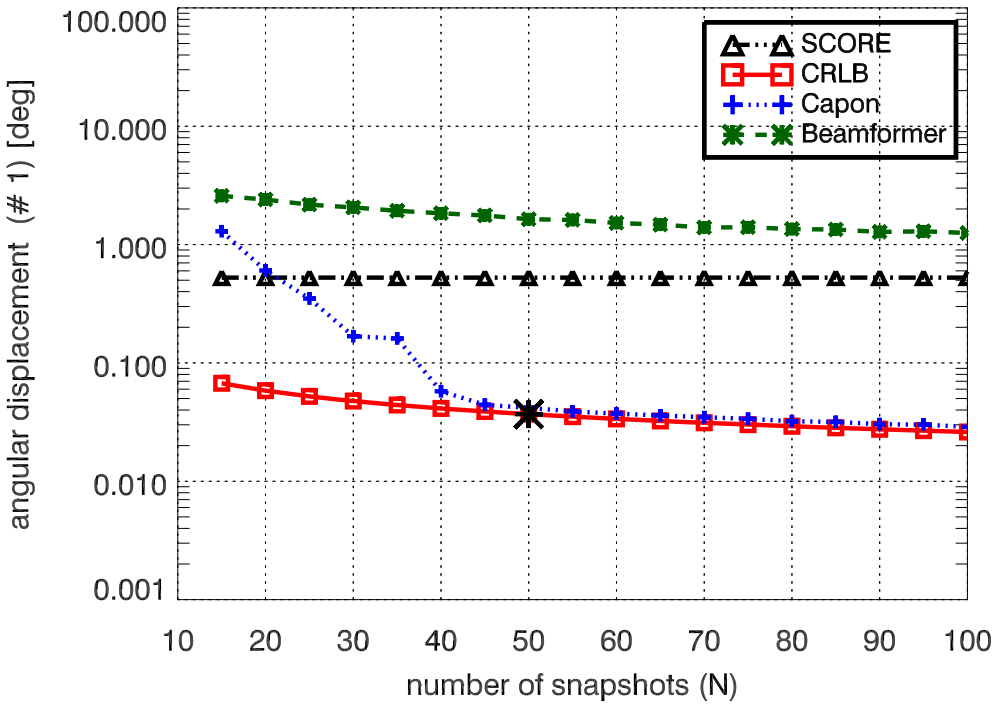

Figure 7-19: Angular displacement on source #1 vs. number of snapshots. $ASNR_{1,2} = 9$ dB and separation between sources ≈ 1 HPBW .

Parameter variation (scenario)	Angular displacement		Pattern loss		Comments
	ADBF	SCORE	ADBF	SCORE	
$\Delta\boldsymbol{\theta}$ (0)	decreases till 0.025º (CRLB) for $\Delta\theta > 1.5$ HPBW	constant	--------	--------	worse scenario ($ASNR_2 = ASNR_1$), MUSIC discarded
$\boldsymbol{h}_{1,2}$ (1)	insensitive follows CRLB (0.025º)	increases till 1.42º (at 8 Km)	negligible	increases (values between 0 to -25 dB)	--------
$\boldsymbol{g}_{1,2}$ (2)	insensitive follows CRLB (0.025º)	decreases till 0.43º	negligible	decreases from -3.1 till -2.0 dB	source #2 out UR for $g_1 > 325$ km
$\boldsymbol{ASNR}_1$ (3)	decreases approaching CRLB ($ASNR_1 > 3$ dB)	insensitive at 0.52º	negligible for $ASNR_1 > 3$ dB	constant at -3.0 dB	--------
$\boldsymbol{H}_a$ with const. $\boldsymbol{d}$ (4)	decreases from 0.1º till *ca.* 0.019º following CRLB	insensitive at 0.52º	negligible	increases from -0.2 dB till -5.8 dB	assumed const. $ASNR_{1,2}$
$\boldsymbol{H}_a$ with const. $\boldsymbol{K}$ (5)	decreases from 0.1º till *ca.* 0.019º following CRLB	insensitive at 0.52º	negligible	increases from -0.2 dB till -5.8 dB	assumed const. $ASNR_{1,2}$
$\boldsymbol{K}$ with const. $\boldsymbol{H}_a$ (6)	small fluctuations around 0.025º	insensitive at 0.52º	negligible	nearly const. at -3.0 dB	source #2 out UR ($K < 13$); CRLB not conditioned at $K = 4,\ 8$
$\boldsymbol{H}_1$ (7)	increases from 0.025º to *ca.* 0.14º departing the CRLB	insensitive at 0.52º	slightly increases till -0.18 dB	constant at -3.0 dB	widening of associated peak in estimated spectrum
$\boldsymbol{N}$ (8)	decreases from 0.06º/0.05º to *ca.* 0.018º approaching the CRLB	insensitive at 0.52º	negligible	constant at -3.0 dB	$N < 72$ to avoid RCM correction

Table 7-3: Numerical simulations summary for the different operational scenarios.

7.4 Azimuth topography effect

In the model considered along the thesis, it is assumed a simple reference surface with homogeneous backscattering and constant topographic height along ISO-range. However, in real acquisition scenarios this hypothesis can not be always regarded as true. In the following, it is presented a preliminary discussion on how the performance of the ADBF would be affected in such conditions.

In ADBF the steering direction corresponds to the estimated DOA associated to each range sample. Till now, it has been analyzed the presence of range ambiguities with the actual echo of interest. However, a multi-source scenario can also be considered due to layover, i.e. sources with the same slant range distance as the echo of interest but different topographic height. Then, these signals arrive at the same instant of time and are mapped to the same range sample.

In fact, the analysis of the layover problem will allow understanding the effect of topographic height variation along ISO-range lines. All the points located over a sphere of radius equal to the slant-range distance to the echo of interest and centered on the satellite constitute sources in layover. Then, the ones located in azimuth positions different form center of the azimuth beam, will be mapped also into this vertical slant-range plane with some specific DOA. Thus, the presence of targets at the same slant-range distance as the source of interest and illuminated by the azimuth pattern are sources in layover on the same vertical/elevation plane.

In Figure 7-20 a), this effect is illustrated considering the actual source of interest (#1) and two sources (#2 and #3) with the same slant-range distance as #1 (R_1), but at different azimuth positions. The source denoted as #2 has the same topographic height as source #1 (h_1), whereas the other one differs in this parameter (h_3). The different targets will be mapped into the same vertical slant range plane, where source #1 and #2 have the same DOA ($\theta_1 = \theta_2$) because the azimuth aperture is small enough to consider negligible the curvature of the earth; whereas the third has a different DOA (θ_3), see Figure 7-20 b). The two first sources exemplify the model assumption of constant topographic height made in the thesis and the presence of azimuth topography changes can be modeled by this third source.

This variation on the topographic heights is translated into a variation on the DOA and so the angular separation of the sources in layover. Then, it is expected a different distribution of the received power as a function of the DOA. In Figure 7-21, the difference in terms of DOA has been computed for two sources in layover when the topography of one of them is varied respect from the other reference source. This situation perfectly models the case of source #1 and #3 in Figure 7-20.

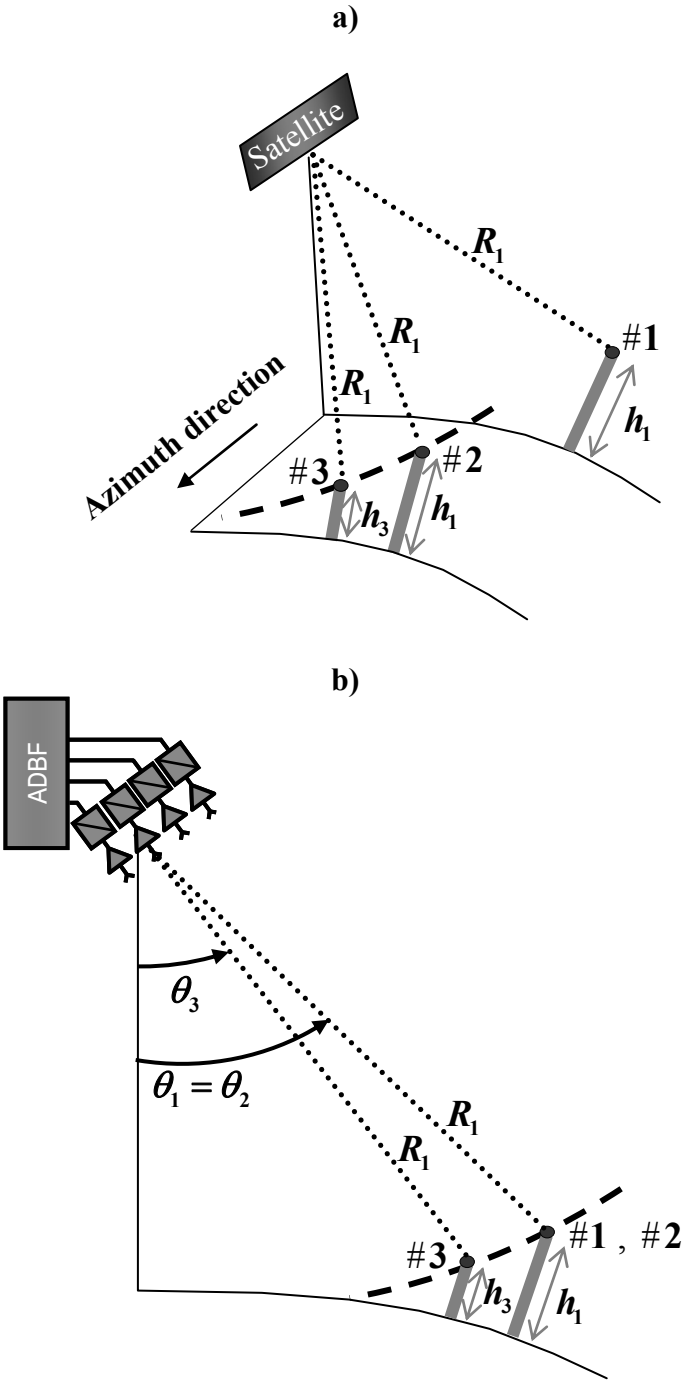

Figure 7-20: a) Sources (#2, #3) in layover with the echo of interest (#1), **b)** projection of the sources into the same slant-range vertical plane.

The results obtained in Figure 7-21 consider the reference SAR system in Table 7-1 and one source located at the near edge of the imaged swath (300 km) with no topographic height. The second source has the same slant-range distance but its topographic height is varied between 0 km and 4 km. From the approximate extension of the footprint about 13 km (azimuth) by 70 km (range), the assumption on a topographic variation in the order of 4 km can fit suitable. The angular separation between the sources is below 0.7°. Then, in the estimated spectrums from Beamformer and Capon, there will be a unique peak since the separation is under the resolution capabilities of both methods, see Figure 7-3 a). In this situation the ADBF will steer the beam to an intermediate DOA. Considering the synthesized receive pattern according to the reference system, the ADBF will recover the energy backscattered from both sources within the -3 dB mainlobe of the receive pattern ($HPBW \approx 1^{\circ}$). However, in the case of conventional SCORE that assumes no topography, the layover source at 4 km will be acquired with approximately -6 dB respect the maximum gain, see Figure 7-4 b). Under these conditions of azimuth topographic change, ADBF performs better than SCORE as it can recover the different backscattered energy from the illuminated swath maximizing the gain in reception.

For higher topographic variations and/or nearer ground positions[40] the DOA variation is 1 HPBW – 2.5 HPBW and the estimation methods can resolve two different peaks in the spectrum. In general ADBF directs the beam where most of the power is concentrated. Under the previous conditions a different approach should be analyzed. A possible option is the generation of simultaneous multiple beams steered towards the different DOAs associated with the highest power concentrations.

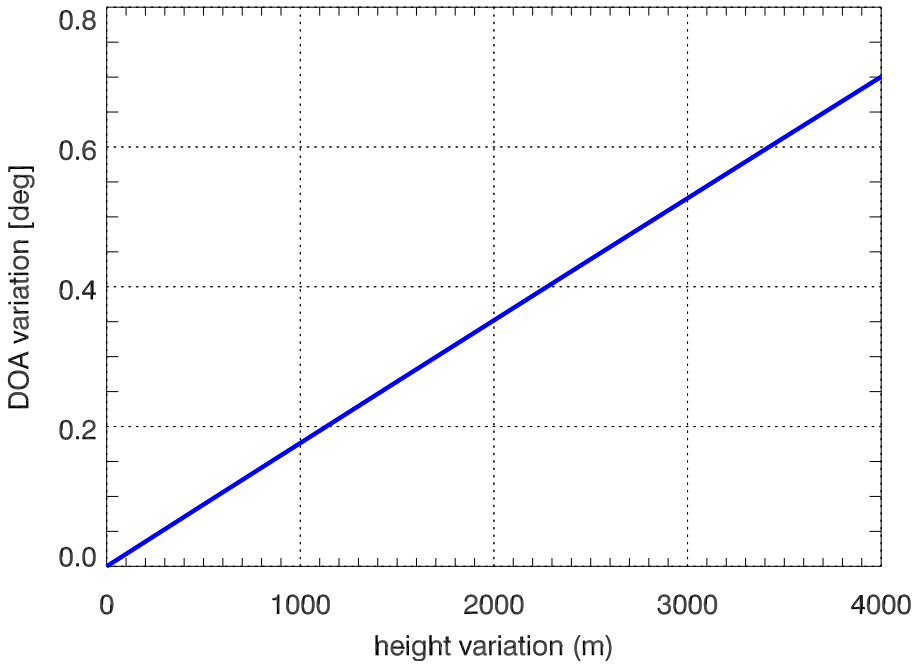

Figure 7-21: Variation on the DOA between two sources in layover for topographic height variations of one of them w.r.t. the other (reference height 0 km).

[40] The HRWS SAR reference system covers a whole swath of ground range 140 km – 557 km from nadir of the satellite.

Chapter 8 Conclusions and Future Work

This thesis has proposed a novel algorithm, denoted as Adaptive Digital Beam-Forming, to steer the elevation receive beam pattern on high-resolution wide-swath SAR systems. The actual mechanism, SCan-On-REceive, does not include in its implementation topographic information of the acquisition geometry, which is translated into a performance degradation respect ideal conditions, i.e. no topography.

The new contribution of this algorithm is the application of DOA estimation in the SAR field, taking advantage of digital processing the signals available from the multi-channel receive antenna. This option provides an adaptive mechanism for steering of the elevation receive pattern, trying to overcome the SCORE limitation.

The DOA estimation on high-resolution wide-swath SAR spaceborne shows some specific challenges/peculiarities, as on-board processing of wideband chirp signals and presence of superimposed ambiguous returns to the useful signal from the wide illuminated areas. The existing algorithms in the estimation literature do not fulfill the SAR specificities, either due to the wideband SAR signal model, which do not enable the use of narrowband methods, or the additional constrains on the complexity introduced by the wideband approaches.

The proposed ADBF method introduces a pre-processing step, based on range compression and coregistration of the signals from the multiple elevation channels. This approach allows a direct application of simple robust narrowband spectral estimation methods, Beamformer and Capon. The superresolution capabilities offered by another well-known narrowband algorithm as MUSIC, are not required in the specific high-resolution wide-swath SAR scenario since the angular separation between the echo of interest and the range ambiguous returns is large enough ($> 5º$). Additionally, this estimation method is model-based, assuming some specific data distribution (sinusoidal signals) and the knowledge of the number of sources results crucial to its correct operation.

In this thesis the potentiality of the adaptive approach has been evaluated comparatively to the conventional SCORE. To this end, the performance of the ADBF has been numerically simulated via Monte Carlo experiments considering different operational scenarios, where single parameters of interest are varied keeping the rest constant, under a realistic SAR system/scenario. A Cramér-Rao Lower Bound analysis has been also included in the comparative study setting a benchmark on the achieved performance. The different numerical results, summarized in Table 7-3 prove the capability of the ADBF to improve SCORE performance in presence of topography.

From this analytical study, the ADBF algorithm results almost insensitive to the variation on the topographic profiles and the location of the sources along the swath; whereas SCORE performance degrades proportionally to the topographic height and at closer ranges. In the reference scenario, the pattern loss associated to ADBF is negligible for the whole swath of interest and different surface elevations.

The numerical simulations have shown that *ASNR* turns to be one of the most sensitive parameters in the performance of the ADBF, which improves as a function of the *ASNR* of the echo of interest; whereas SCORE remains unaltered. A threshold value exists, where the performance of ADBF becomes comparatively better than SCORE. This boundary is around 0 dB for the reference scenario, above which the ADBF reaches the CRLB and has a negligible PL.

Antenna parameters such as dimension and number of sub-apertures strongly affect the complexity/cost of the system and the ADBF implementation itself. The different numerical simulations involving the receive antenna geometry configuration allow considering the alternative to use a sub-set of the available reference sub-apertures, reducing the complexity of the ADBF while keeping the power requirements.

The variation on the number of elements keeping the inter-element spacing, i.e. unambiguous DOA range (UR), shows that a good performance can be obtained with a reduced number of elements. Therefore, it is possible to activate a set of the total channels for the estimation of the DOA implemented by the ADBF; then, the receive sharp beam is synthesized using the whole antenna, keeping the gain and the imaging requirements in terms of RASR.

The invariance on the results respect the previous scenario when the antenna height is varied keeping the number of sub-apertures ($K = 15$), confirms that redundant information is obtained for the reference elements. This justifies the suggested approach of using just a reduced set of them in the ADBF DOA estimation. For this latter option the unambiguous DOA range (UR) covers the swath extension but not the first range ambiguity for the whole illuminated area. Then, the estimation performance associated to this range ambiguity degrades, which can be translated into a wrong implementation of a possible null-steering. An antenna configuration with the same number of sub-apertures ($K = 15$) but reduced size will result in wider UR, at expenses of increasing the power requirements and ADBF complexity.

The alternative antenna configuration analysis, where the total size is kept and the number of elements is modified, prove also that redundant information is provided by an increased number of sub-apertures as the performance remains almost unaltered. In this sense, antenna geometry with a reduced number of elements favors a relaxation on the ADBF complexity, but implies a reduction on the UR and the range ambiguity performance. Then, the antenna geometry choice should compromise complexity/cost, UR extension and ambiguity performance.

The presence of multiplicative speckle, which models the extended characteristic of the sources, under conditions of complete decorrelation at the extreme channels of the reference receive antenna still allows obtaining better results than conventional SCORE. The associated PL can be regarded as imperceptible for the considered realistic SAR scenario.

The simulated scenario accounting for a variation on the number of subsequent azimuth acquisitions, illustrates an improvement on the ADBF performance when more snapshots are available. These results also prove that with a low number of snapshots (10 – 50) a good operation with the ADBF can be obtained, reducing the complexity implementation of this adaptive approach.

It is possible to consider a greater number of snapshots in order to alleviate the degradation of the ADBF in situations of reduced $ASNR$. In any case the value of these observations should be kept below 72 to avoid additional computation, required to compensate the Range Cell Migration effect derived from the different geometry acquisition along azimuth.

Summarizing, the numerical simulations have shown that the novel algorithm ADBF outperforms the conventional SCORE in presence of topographic height for the different operational scenarios. Moreover, it is also possible to still obtain satisfactory results when a sub-set of the available sub-apertures is used reducing the complexity of the ADBF approach.

The evaluation of the ADBF has considered a data model characterization analogous to the case of multibaseline interferometry. In this thesis it is assumed homogeneous backscattering and constant topographic height along the ISO-range surface delimited by the range cell size and the mainlobe aperture of the azimuth pattern. Though simple, this approach allows for a first comparison between SCORE and the ADBF performance. Then, a further future step should consider the study of a more realistic model and the influence of the variation of both, backscattering properties and azimuth topography.

A rough preliminary analysis has been carried to better understand the impact of the azimuth topographic changes. In this case, surface azimuth variations have been translated into presence of sources in layover with slightly different DOAs. Changes of the topography in the order of thousands of meters imply variation of the associated DOA of several tenths of degrees. These values are below the resolution capabilities of Beamformer and Capon. Then, from the estimated spatial PSD the ADBF will steer the receive beam towards an intermediate DOA where more power concentration exists, recovering the backscattered energy from the different sources in layover. These azimuth topographic variations are not considered in the conventional SCORE, where the degradation in such layover situation can result in the order of several dBs, depending on the topographic height and the beam sharpness. Therefore, information associated to the sources in layover with some elevation profiles may not be recovered.

The analysis of a scenario with sources in layover is an open point that must be carefully studied. Of special interest is how the ADBF should be implemented in those situations where the angular separation between the layover areas in terms of DOA is greater than the lowest resolution of the estimation methods.

A future step can deal with the estimation of the range ambiguous returns and the associated null-steering implementation trying to improve the ambiguity performance. An additional complexity in this case can result from the inability to distinguish between sources in layover and the range ambiguities that can overfold in the unambiguous DOA range when non-homogeneous backscattering is considered.

This thesis has contribute to the application of adaptive digital processing in the SAR field, which is a hot research topic and a wide range of applications are expected in a near future.

Annex A Data Model

A.1 Coregistration

After range compression, the different channels have responses located at different slant range positions (see section 4.1). Then, they should be aligned respect to the reference (first) sub-aperture in order to ensure that the recorded complex samples at the different sub-apertures correspond to the same backscattering area.

The difference in slant range between the different sub-apertures of the receive antenna depends on the acquisition geometry. In the following it is analyzed the evolution of the slant range variation along the imaged swath for the extreme sub-apertures.

Figure A-1 illustrates the geometry of the problem for a target with topographic height h, where a spherical Earth model is assumed. The parameter to be computed is the difference between the slant range at the first phase center R_1 and at the $K-th$, R_K.

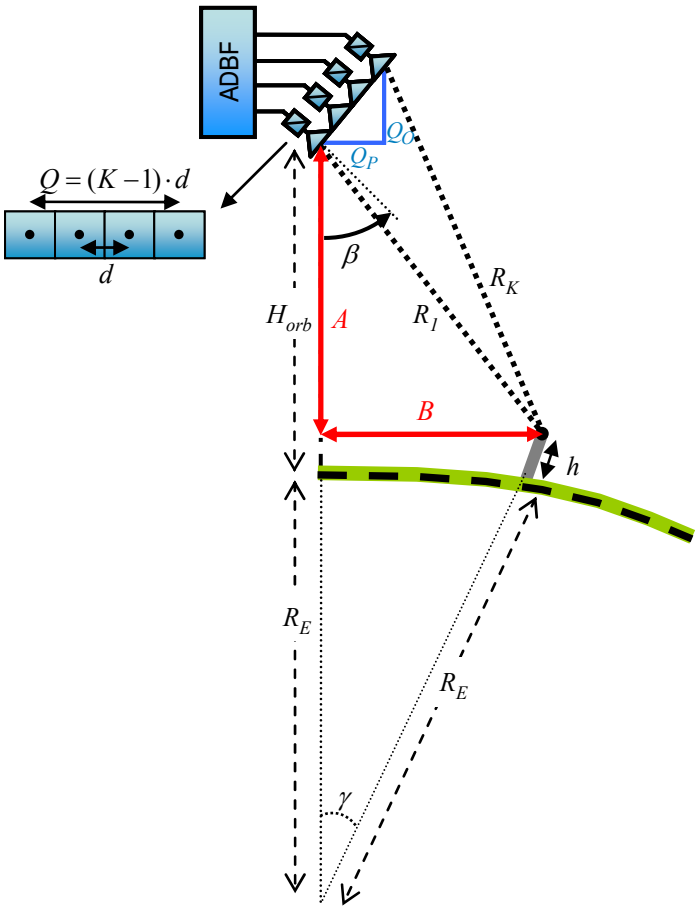

Figure A-1: Acquisition geometry: different slant range distances at extreme sub-apertures (distances and angles not in scale).

After some trigonometry, the variation on the slant range between the extreme sub-apertures of the ULA receive antenna is:

$$\Delta R = R_K - R_1 = \sqrt{(A+Q_O)^2 + (B-Q_P)^2} - R_1 \tag{A.1}$$

where Q_O and Q_P are respectively the orthogonal and parallel components of the distance between the two extreme phase centers of the receive antenna Q, Figure A-1:

$$Q_O = Q \cdot \sin(\beta) \tag{A.2}$$

$$Q_P = Q \cdot \cos(\beta) \tag{A.3}$$

with β the tilt angle of the receive antenna. The components A and B can be computed as:

$$A = H_{orb} + R_E - (R_E + h) \cdot \cos(\gamma) \tag{A.4}$$

$$B = (R_E + h) \cdot \sin(\gamma) \tag{A.5}$$

where H_{orb} is the orbit height; R_E the radius of the earth; h the topographic height and γ is the angle at the center of the earth, which can be obtained from the law of cosines based on the knowledge of R_1 and h:

$$\gamma = \arccos\left(\frac{(H_{orb} + R_E)^2 + (h + R_E)^2 - R_1^2}{2 \cdot (H_{orb} + R_E) \cdot (h + R_E)} \right) \tag{A.6}$$

Figure A-2 represents the evolution of the slant range difference as a function of the ground position for different topographic heights. It has been considered the reference system in Table 7-1. From Figure A-2, ΔR has a linear evolution along the swath with different variation for the set of topographic heights. In any case, the divergence between the slant ranges at the extreme sub-apertures is confined to $|\Delta R| \leq 0.07$ m, which is approximately one tenth of the slant range resolution ($\delta_r = 0.6$ m). Then, for each range sample there is a different compensation.

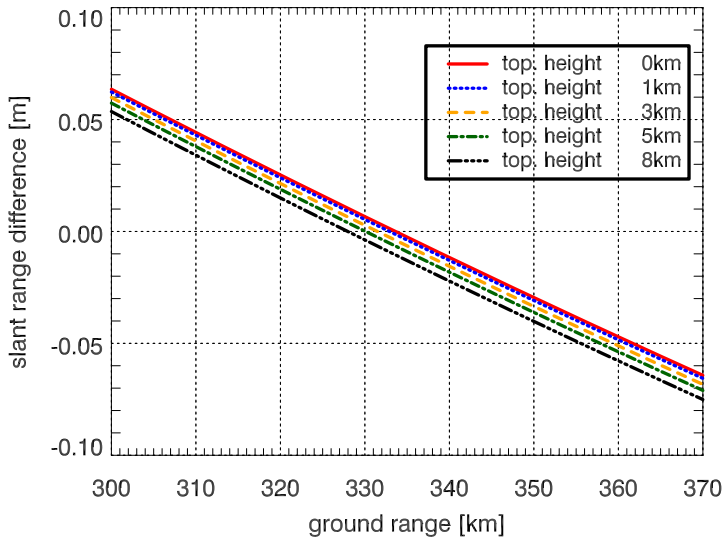

Figure A-2: Slant range difference at extreme phase centers of a multi-channel receive antenna vs. ground position.

A.2 Multiple azimuth acquisitions

In Chapter 4 and Chapter 5, the term *snapshots* constitutes the observations over the same target acquired from multiple consecutive pulse transmissions, i.e. each pulse repetition interval (PRI[41]) a new sample is obtained.

The geometry of the acquisition is changing when the satellite is displacing in the azimuth direction and two effects should be considered: variation of DOA corresponding to the same target and the range cell migration on the time delay, i.e. the recorded samples for the same target have different slant range distances. In the following, these two effects are analyzed for a specific SAR real scenario.

A.2.1 DOA variation

In this section, it is studied the evolution of the DOA as a function of the multiple snapshots under the variation of specific parameters in the acquisition geometry: topographic height of the source, orbit height and location of the source in the imaged swath.

The geometry of the problem is presented in Figure A-3 a). The idea is to compare the DOA θ_1 at the closest approach and θ_n, when the satellite has acquired the $n-th$ snapshot. It must be pointed out that the analysis here described contemplates half of the total number of samples, because of symmetry considerations. However, it is possible to double the number of snapshots if the observations from the symmetric position P_n' to P_1, Figure A-3 b), are also included.

It is assumed that the flight path of the satellite is in a constant plane of elevation equal to the orbit's height H_{orb} and with constant velocity V_s during the multiple acquisitions. Then, the slant range distance R_n can be expressed in terms of the one at the closest approach R_1 as:

$$R_n = \sqrt{R_1^2 + \left(V_s \cdot t_n\right)^2}, \qquad n = 1,...,N/2 \tag{A.7}$$

where $t_n = \left(n-1\right)/PRF$ is the time corresponding to the azimuth displacement between P_1 (first acquisition) and P_n ($n-th$ acquisition); PRF is the pulse repetition frequency and N is the total number of snapshots.

Once computed the slant range distance R_n, the corresponding θ_n is retrieved from the geometry in Figure A-3 a), for a spherical Earth model as:

$$\theta_n = \arccos\left(\frac{\left(H_{orb}+R_E\right)^2 + R_n^2 - \left(R_E+h\right)^2}{2\cdot\left(H_{orb}+R_E\right)\cdot R_n}\right) \tag{A.8}$$

where H_{orb} is the orbit's height, R_E radius of the earth and h the topographic height.

[41] The PRI corresponds to the inverse of the Pulse Repetition Frequency (PRF).

The different results here presented consider the reference system described in Table 7-1 with a $\mathrm{PRF} = 1775$ Hz. Moreover, the DOA variation has been computed for a reference source located at a ground position of 304.42 km (for $H_{orb} = 520$ km) and topographic height $h = 3$ km.

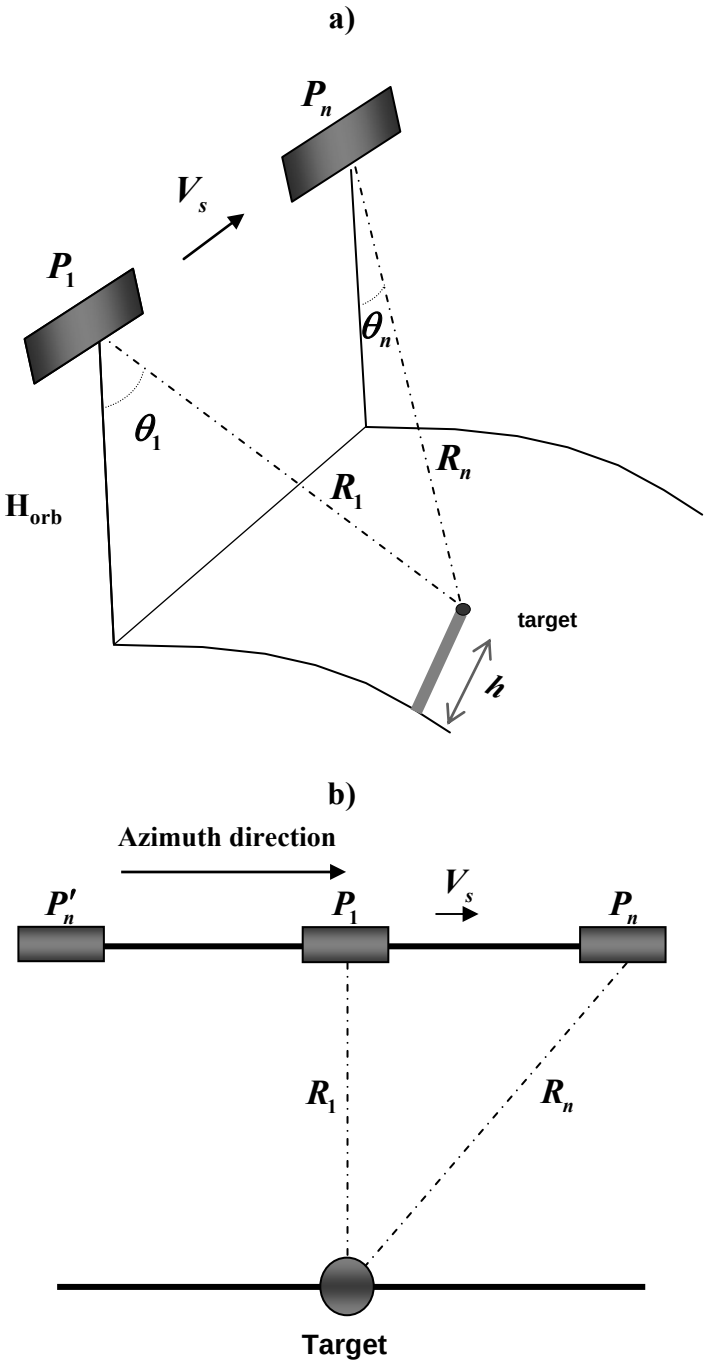

Figure A-3: Acquisition geometry, **a)** vertical plane and **b)** slant plane view.

A.2.1.1 DOA variation versus number of snapshots

Figure A-4 illustrates the DOA variation as a function of the different azimuth acquisitions. It can be observed that the higher is the number of snapshots, the higher is this variation because the associated slant range distance also increases.

In order to consider the multiple acquisitions equivalents and to avoid that the DOA variation introduces additional error in the estimation procedure, a number of snapshots below 50 allows neglecting its influence. In this case the corresponding change on DOA is under 10^{-5} degrees, which is two orders of magnitude below the best achievable performance of the ADBF through the Cramér-Rao Lower Bound (RMSE[42] $\approx 0.003º$, see section 7.3.4). Then, this number of snapshots can be doubled to 100, considering the symmetric acquisitions from position P'_n to P, Figure A-3 b).

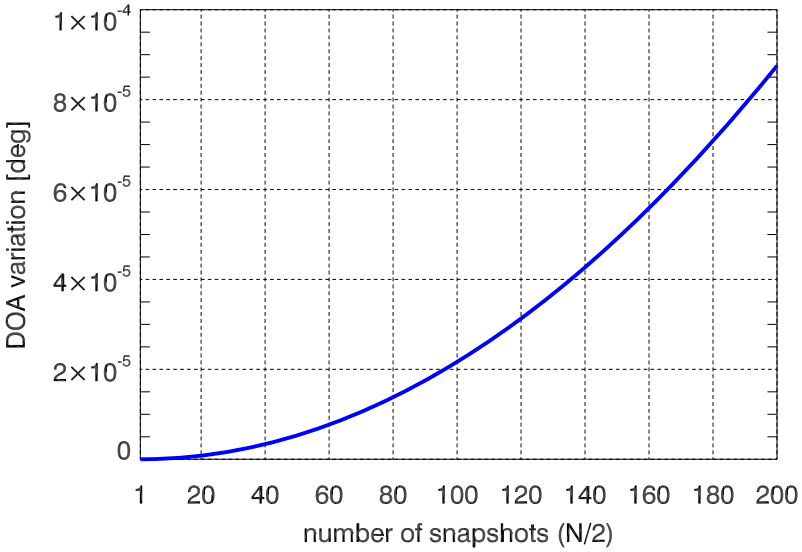

Figure A-4: DOA variation vs. number of snapshots.

A.2.1.2 DOA variation and topographic height

From Figure A-5, a change on the topographic height has not too much influence on the variation of the DOA as a function of the snapshots. This parameter affects the slant range distances R_1, R_n and θ_n, but for the considered topographic values (< 8 km) the change is almost imperceptible.

[42] RMSE indicates the root-mean square error on the estimation (section 7.1)

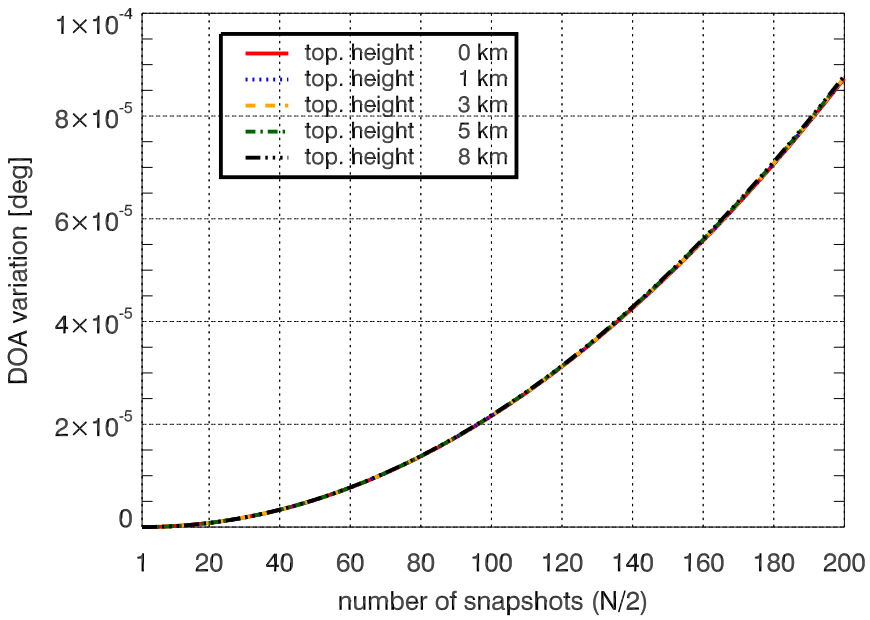

Figure A-5: DOA variation vs. number of snapshots for different topographies.

A.2.1.3 DOA variation and orbit height

In this case the influence of the orbit height variation is studied keeping the reference topographic height $h = 3$ km . From Figure A-6, the higher the orbit of the satellite, the lower is the variation on the DOA. Increasing the orbit height decreases the satellite velocity and the slant range variation is lower for the same number of acquisitions. Hence, the associated DOA variation is smaller.

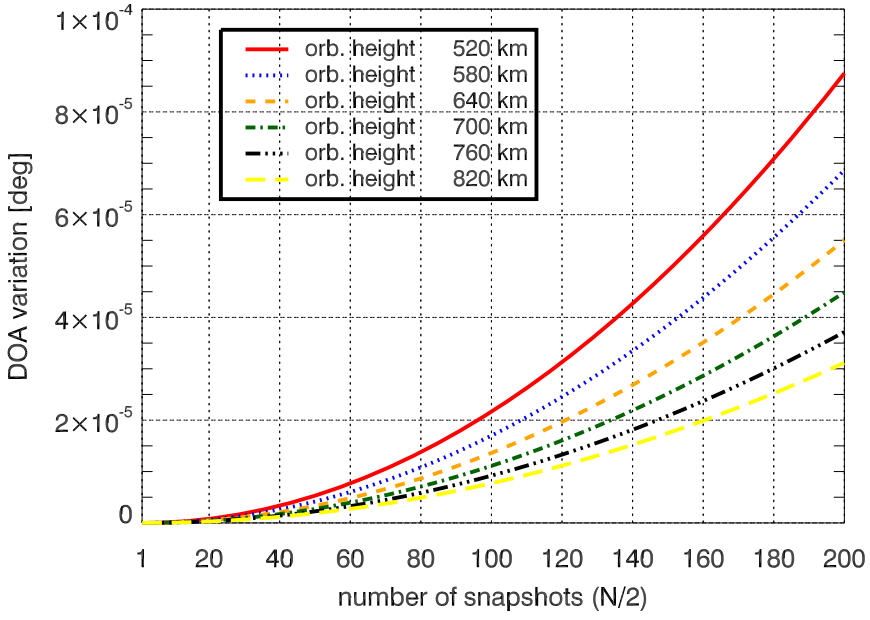

Figure A-6: DOA variation vs. number of snapshots for different orbit heights.

A.2.1.4 DOA variation and ground position

It is analyzed how the DOA varies for different positions of the target along the swath extension (300 km -370 km), keeping the reference topographic height. The DOA variation for the same number of acquisitions is higher for targets located in near range than the ones in far range, Figure A-7.

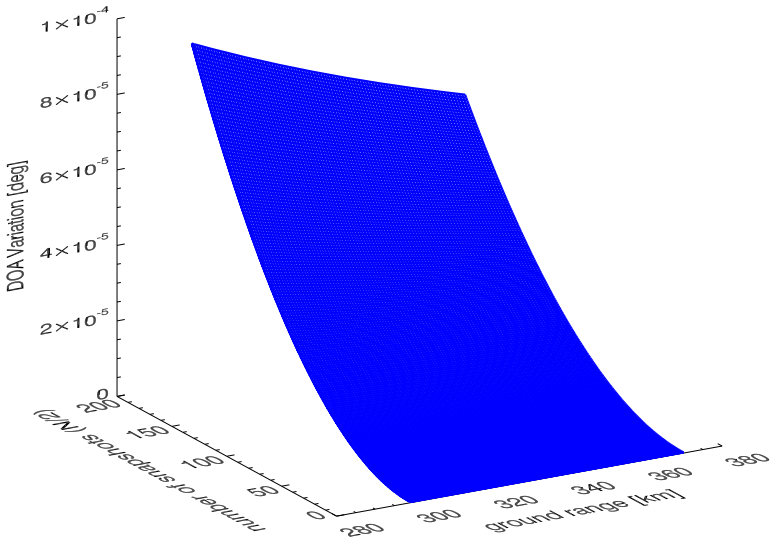

Figure A-7: DOA variation vs. number of snapshots for different ground locations.

From the previous analysis, the orbit height variation turns to be the most sensitive parameter in the DOA variation. However, it must be pointed out that if it is just considered a number of snapshots below 100 (also included the symmetric acquisitions), the variation of the orbit height doesn't affect the evolution of the DOA variation.

As it has been mentioned, the DOA variation should be well below the best accuracy performance, trying not to influence the estimation. In this sense and after the analysis, the number of snapshots should be considered below 100 (also included the symmetric acquisitions). It must be noted that the DOA variation for these values ($N < 100$) is negligible not only for the imaged reference swath/subswath 300 km -370 km) but for the whole swath that the HRWS SAR system should cover (170 km -557 km)[43].

[43] The DOA variation along the whole swath is below $1.25x10^{-5}$ degrees for $N < 100$.

A.2.2 Range Cell Migration (RCM)

A related effect is the RCM, i.e. the time-delay associated to the same backscattering source changes during the multiple acquisitions. Therefore, the echoes from the same target corresponding to successive pulse transmissions are located at different range positions. This effect is similar to the problem of range variation for the different sub-apertures in elevation, which was reduced by coregistration procedure (annex A.1). Then, it is required to compute the corresponding RCM in order to understand whether the different snapshots are still located within the same range resolution cell.

Based on the geometry in Figure A-3, the RCM is computed as the difference between R_1 and R_n:

$$RCM = R_n - R_1 = \sqrt{R_1^2 + \left(V_s \cdot t_n\right)^2} - R_1, \quad n = 1, \ldots, N/2 \tag{A.9}$$

In Figure A-8, the RCM has been evaluated as a function of the number of snapshots for the same system/scenario parameters considered in the previous section. The higher the number of acquisitions the higher is the range variation.

To neglect the effect of RCM on the different samples, its value should be well below the slant range resolution of the system, which is in the order of 0.6 m. A number of snapshots under 36 produces a RCM < 0.02 m, which is 1/30 times the slant resolution. It must be noted that this number of snapshots can be doubled to 72 if the symmetric acquisitions are considered. Then, the RCM can be neglected for a number of snapshots below 72, which is valid for the whole swath (170 km – 557 km) covered by the HRWS SAR system in Table 7-1.

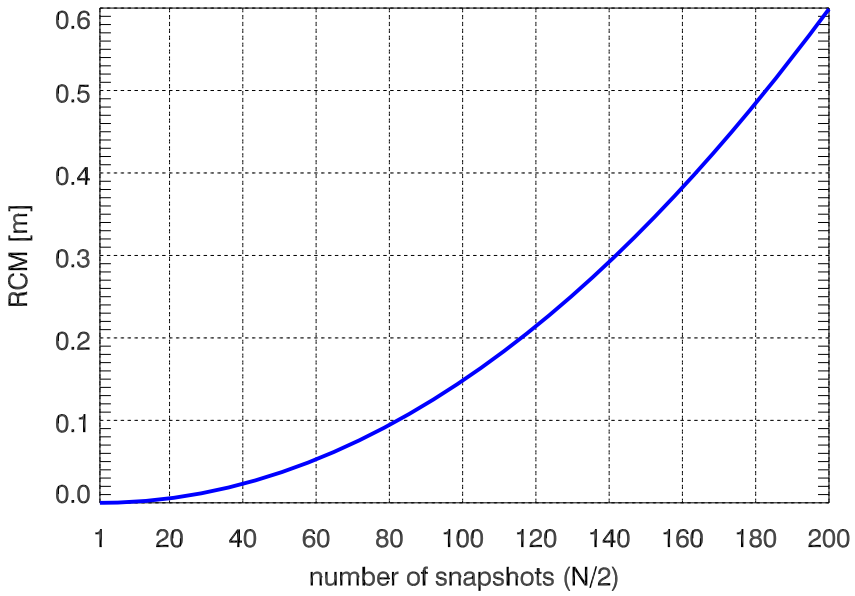

Figure A-8: Range Cell Migration (RCM) vs. number of snapshots.

A.3 Critical antenna height

In section 5.1, the term of critical antenna height H_c is introduced in the statistical description of the model. The idea behind this concept is intuitive: considering the two extreme sub-apertures of the receive antenna, they observe the same range resolution cell but over two different angles due to the physical separation (Figure A-9). Then, this difference in the observation perspective causes diverse combinations of the scatterers within the resolution cell, i.e. different speckle patterns. Therefore, increasing the separation between the two extreme elements, the variation of the observation angles increases and so the decorrelation of the speckle. This decorrelation is complete when the separation matches the critical antenna height.

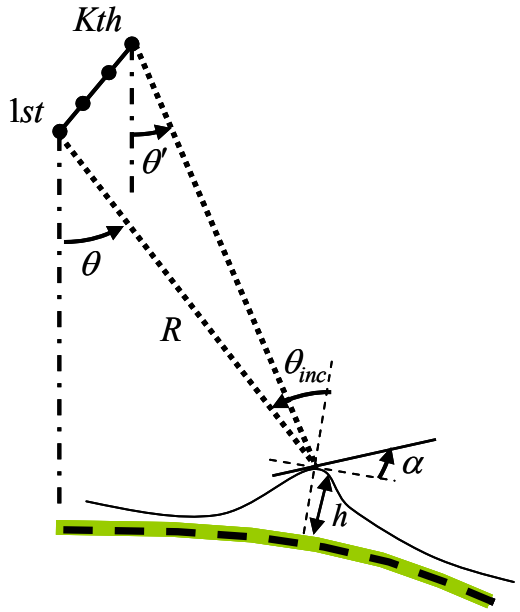

Figure A-9: Acquisition geometry at extreme phase centers of a *K*-channel antenna.

To derive the critical antenna height it is referred to the analog critical baseline defined in InSAR. As it is well-known, the cross-track interferometry combines two SAR images acquired by two sensors separated by a baseline to form an interferogram, which provides information of the elevation dimension (InSAR conceptual review can be found in [2]).

In [18], the different components of the ground spectrums observed at the two sensors are used to explain the concept of critical baseline, which is obtained when the spectral shift equates the system bandwidth. For a *bistatic*[44] configuration the spectral shift induced by a given baseline is half that obtained by a *monostatic* case. Thus, the critical baseline in the bistatic case is doubled.

[44] In the bistatic configuration one sensor is equipped with a transmitter and a receiver, whereas the other with a receiver. In the monostatic case the two sensors have transmitter and receiver.

The high-resolution wide-swath SAR system here considered has a bistatic configuration and the corresponding critical antenna height can be obtained from [18]:

$$H_c = \frac{2 \cdot \lambda \cdot R \cdot BW \cdot \tan(\theta_{\text{inc}} - \alpha)}{c_0} \tag{A.10}$$

where λ corresponds to the carrier wavelength; R slant range distance; BW is the system bandwidth; θ_{inc} indicates the incidence angle; α the local slope and c_0 the light velocity.

In fact, the previous expression corresponds to the so called orthogonal critical baseline, i.e. orthogonal projection of the baseline to the line of sight [23]. In abuse of nomenclature, the antenna critical height refers to the line of sight orthogonal projection of the distance between the extreme phase centers.

From Figure A-10, the critical antenna height[45] increases linearly along the imaged swath (slant range and incidence angle increases) and has lower values when the local slope increases. From these values of the critical antenna height (several and tens of km), the speckle can be regarded as completely correlated along the sub-apertures since the distance between the extreme phase centers for the reference antenna is 1.4 m.

[45] Computed for the reference system in Table 7-1, working at 9.65 GHz and a bandwidth of 250 MHz.

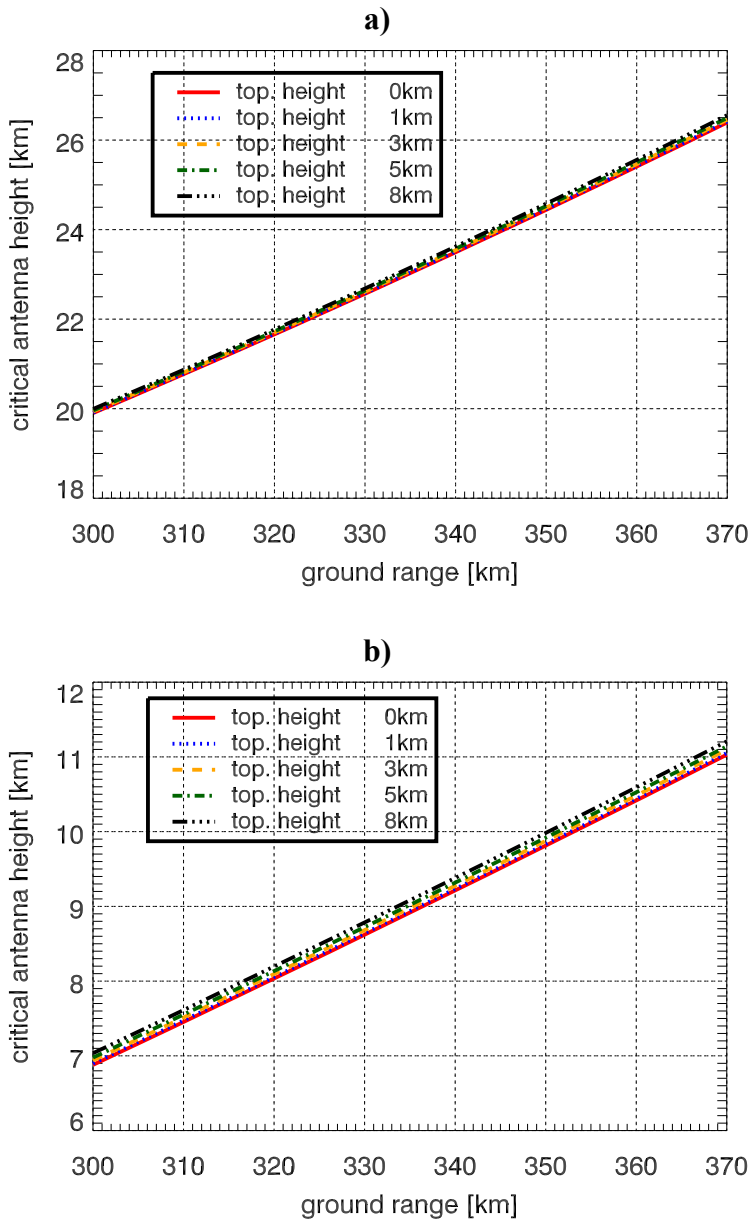

Figure A-10: Critical antenna height variation vs. ground position for different topographic heights and local slope of **a)** $\alpha = 0^{\circ}$ and **b)** $\alpha = 20^{\circ}$.

Annex B Range Ambiguities

A multi-source scenario is considered due to the presence of layover or range ambiguities. In the later case, echoes from preceding and succeeding pulses arrive simultaneously with the echo of interest. The slant range positions of the ambiguous signals are given by [14]:

$$R_i = R + i \cdot \frac{c_0}{2 \cdot PRF}, \quad i \in \{-N_N, \ldots, -1, 1, \ldots, N_F\} \tag{B.1}$$

where R corresponds to the slant range of the useful signal, N_N and N_F are the number of ambiguities in near and far range, respectively. Assuming that the ambiguities have the same topographic height h as the echo of interest, the ambiguous slant range is limited by:

$$H_{orb} - h \leq R_i \leq R_{horiz} \tag{B.2}$$

with H_{orb} the altitude of the satellite and R_{horiz} the slant range distance at the horizon.

Figure B-1 illustrates the difference of DOAs between the echo of interest and the range ambiguities along the imaged swath[46]. The corresponding DOA of the echo of interest is indicated in a secondary axis. In this case, the closest range ambiguity is located at $\approx 9^o - 10^o$ from the source of interest, which is a value much higher than the resolution capabilities of any estimation methods (see section 7.3.1). In general, the closest range ambiguity is located between 5º-15º from the signal of interest within the whole swath covered by the HRWS SAR (170 km – 557 km).

As described in Chapter 4, the estimation of the sources DOA is limited to an unambiguous DOA range (UR)[47]. For the reference system, the DOAs are restricted to $23.3^o < \theta_{unamb} < 41.2^o$. This span allows covering the DOA of the echoes of interest, $29.6^o \leq \theta_{swath} \leq 35.3^o$, within the swath and for topographic heights from 0 km to 8 km. However, the corresponding range ambiguities can be located out of this interval depending on the ground location of the useful source and the ambiguity itself as can be seen form the values presented in Figure B-1. These range ambiguities fold back into the unambiguous DOA interval due to the periodicity of the spatial spectrum.

This backfolding effect can perturb the estimation of the useful signal, when the DOA of the range ambiguity is close to an ambiguous DOA associated to the echo of interest. In Figure B-1, the dashed black lines indicate the angular separation of the ambiguous DOA of the echo of interest: the closest range ambiguities to the ambiguous DOAs are the second, third and fourth far range (blue, orange and green solid curves) and the first near range ambiguity (red dotted curve).

[46] It has been considered the reference system in Table 7-1 with a $PRF = 1775$ Hz and a topographic height $h = 3$ km (source of interest and ambiguities). The angular separation slightly changes for other topographic heights.

[47] The ambiguities in DOA estimation are consequence of spatial aliasing and they must not be confused with the range ambiguities, which can have ambiguous DOA if they lay out of the unambiguous interval of DOAs.

In any case the effect of these range ambiguities (close to ambiguous DOA) can be neglected since they are not weighted by the -3 dB mainlobe of the transmit pattern as it is depicted in Figure B-2. This plot considers the source of interest located at 304 km with a DOA of 30.15º. The associated far range ambiguities of order higher than the first and the first near ambiguity are more than 18 dB below the source of interest. Thus they can be omitted in the analysis.

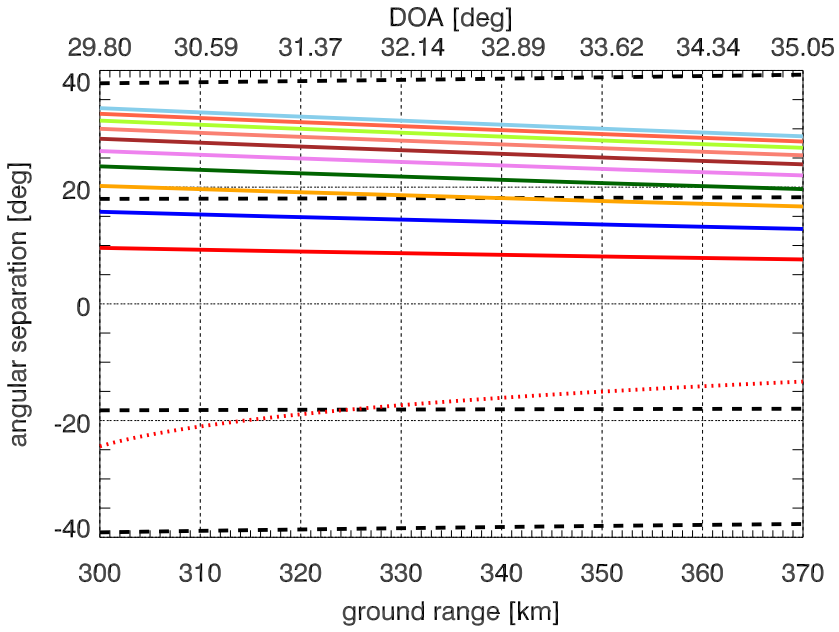

Figure B-1: Angular separation echo of interest and range ambiguities along the swath (colored lines: solid lines far and dotted near ambiguities). Dashed black lines indicate the angular separation of the ambiguous DOAs associated to echo of interest.

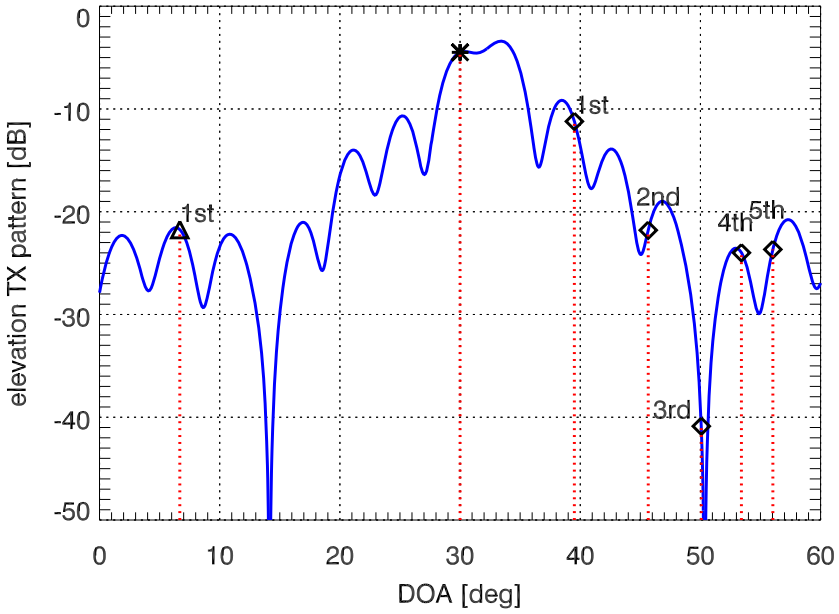

Figure B-2: Transmit elevation pattern (pure phase excitation taper); source interest (asterisk), far range (diamonds) and near range (triangle) ambiguities.

Bibliography

[1] Amin, M.G., and Zhang,Y., "Spatial time-frequency distributions and their applications", *Time-Frequency Signal Analysis and Processing*, Editor, Boashash, B., Elsevier, Oxford, United Kingdom, 2003.

[2] Bamler, R., and Hartl, P., "Synthetic Aperture Radar Interferometry", *Inverse Problems*, vol. 14, pp. R1-R54, 1998.

[3] Belouchrani, A., and Amin, M. G., "Time-Frequency MUSIC", *IEEE Signal Processing Letters*, vol. 6, no. 5, pp. 109-110, May 1999.

[4] Blythe, J. H., "Radar Systems", United States Patent 4,253,098, February 24, 1981.

[5] Bordoni, F., Gini, F., and Verrazzani, L., "Capon-LS for Model Order Selection of Multicomponenet Interferometric SAR signals", *IEEE Proceedings, Part-F, Radar, Sonar and Navigation*, vol. 151, no.5, pp. 299-305, October 2004.

[6] Bordoni, F., and Younis, M., *HRWS Konzeptstudie Phase III*, DLR-Insititut für Hochfrequenztechnik und Radarsysteme.

[7] Bordoni, F., Younis, M., Makhoul Varona, E., Gebert, N., and Krieger, G., "Performance Investigation on SCan-On-REceive and Adaptive Digital Beam-Forming for High-Resolution Wide-Swath Synthetic Aperture Radar", *Proceedings International ITG Workshop on Smart Antennas*, WSA 2009, pp. 114-119, Berlin, February 2009.

[8] Bordoni, F., Younis, M., Makhoul, E., Gebert, N., and Krieger, G., "Adaptive SCan-On-REceive Based on Spatial Spectral Estimation for High-Resolution Wide-Swath Synthetic Aperture Radar", to be published in *Proceedings IEEE International Geoscience and Remote Sensing Symposium*, IGARSS'09, Cape Town, July 2009.

[9] Bordoni, F., Younis, M., Makhoul Varona, E., and Krieger, G., "Adaptive Digital Beam-Forming Algorithm for High-Resolution Wide-Swath Synthetic Aperture Radar", to be published in *International Radar Symposium,* IRS'09, Hamburg, September 2009.

[10] Callaghan, G. D., and Longstaff, I. D., "Wide Swath Space-borne SAR and Range Ambiguity", *Radar 97 (Conf. Publ. no. 449)*, pp 248-252, 14-16 October 1997.

[11] Carrara, W., Goodman, R., and Majewski, R., *Spotlight Synthetic Aperture Radar: Signal Processing Algorithms.* Boston, MA: Artech House, 1995.

[12] Cohen, L, "Time-Frequency Distributions- A Review". *Proceedings on the IEEE*, vol. 77, no.7, pp. 941-981, July 1989.

[13] Cumming, I. G., and Wong, F. H., *Digital Processing of Synthetic Aperture Radar Data, Algorithms and Implementation*. Boston: Artech House, 2005.

[14] Curlander, J. C., and McDonough, R. N., *Synthetic Aperture Radar: Systems and Signal Processing*. New York: Wiley, 1991.

[15] Currie, A., and Brown, M. A., "Wide-swath SAR", *IEEE Proceedings-F*, vol. 139, no. 2, pp. 122-135, April 1992.

[16] Fischer, C., *Analyse eines neuen SAR Konzeptes. Konsolidierung Basisanforderungen und Referenzsystem (AP2400)*. Technical Report, 2632-AST-TB-2400, Issue 2, EADS Astrium, 22.11.2007.

[17] Freeman, A., Johnson, W. T. K., Huneycutt, B., Jordan, R., Hensley, S., Siqueira, P., and Curlander, J., "The Myth of the Minimum SAR Antenna Area Constrain". *IEEE Transactions on Geoscience and Remote Sensing*, vol. 38, no.1, pp. 320-324, January 2000.

[18] Gatelli, F., Guarnieri, A. M., Parizzi, F., Pasquali, P., Prati, C., and Rocca, F., "The Wavenumber Shift in SAR Interferometry", *IEEE Transactions on Geoscience and Remote Sensing*, vol. 32, no. 4, pp. 855-865, July 1994.

[19] Gebert, N., Krieger, G., and Moreira, A., "Digital Beamforming on Receive: Techniques and Optimization Strategies for High-Resolution Wide-Swath SAR Imaging", *IEEE Transactions on Aerospace and Electronic Systems*, 2008, accepted for publication.

[20] Gershman, A. B., and Amin, M. G., "Coherent Wideband DOA Estimation of Multiple FM Signals Using Spatial Time-frequency Distributions", *IEEE Signal Processing letters*, vol. 7, no. 6, pp. 152-155, June 2000.

[21] Gershman, A. B., Pesavento, M., and Amin, M. G., "Estimating Parameters of Multiple Wideband Polynomial-Phase Sources in Sensor Arrays", *IEEE Transactions on Signal Processing*, vol. 49, no. 12, pp. 2924-2934, December 2001.

[22] Gini, F., Montanari, M., and Verrazzani, L., "Estimation of Chirp Radar Signals in Compound-Gaussian Clutter: A Cyclostationary Approach", *IEEE Transactions on Signal Processing*, vol. 48, no. 4, pp. 1029-1039, April 2000.

[23] Gini, F., Lombardini, F., and Montanari, M., "Layover Solution in Multibaseline SAR Interferometry", *IEEE Transactions on Aerospace and Electronic Systems*, vol. 38, no. 4, pp. 1344-1356, October 2002.

[24] Lagunas, M. A., *Lectures on Array Processing I: Introducción*. [Online]. Available: www.cttc.es/en/undergradpubs.jsp

[25] Lagunas, M. A., *Lectures on Array Processing I: Conformación y estimación de dirección de llegada*. [Online]. Available: www.cttc.es/en/undergradpubs.jsp

[26] Lombardini, F., and Gini, F., "Model Order Selection in Multibaseline Interferometric Radar Systems", *EURASIP Journal on Applied Signal Processing 2005:20*, pp. 3206–3219, May 2005.

[27] Griffiths, H. D., and Mancini, P., "Ambiguity Suppression in SARs using adaptive array techniques", *International Geoscience and Remote Sensing Symposium,* IGARSS, vol. 2, pp. 1015-1018, June 1991.

[28] Hung, H., and Kaveh, M., "Focusing Matrices for Coherent Signal-Subspace Processing", *IEEE Transactions on Acoustics, Speech and Signal Processing*, vol. 36, no.8, pp. 1272-1281, August 1988.

[29] Jian Li, and Compton, R.T., "Maximum likelihood angle estimation for the signals with known waveforms", *IEEE Transactions on Signal Processing,* vol. 41, no. 9, pp. 2850-2862, September 1993.

[30] Kay, Steven M., *Fundamentals of Statistical Signal Processing: Estimation Theory*. Prentice Hall, New Jersey, 1993.

[31] Kare, J. T., "Moving Receive Beam Method and Apparatus for Synthetic Aperture Radar". United States Patent 6,175,326, January 16, 2001.

[32] Krieger, G., Gebert, N., and Moreira, A., "Multidimensional Waveform Encoding: A new Digital Beamforming Technique for Synthetic Aperture Radar Remote Sensing", *IEEE Transactions on Geosciences and Remote Sensing*, vol. 46, no. 1, pp. 31-46, January 2008.

[33] Krim, H., and Viberg, M., "Two decades of array signal processing research: the parametric approach", *IEEE Signal Processing Magazine*, vol. 13, no. 4, pp. 67-94, July 1996.

[34] Leou, M. L., Yeh, C. C., and Ucci, D. R., "Bearing estimations with mutual coupling present", *IEEE Transactions on Antennas and Propagation*, vol. 37, pp. 1332-1335, October 1989.

[35] Li, F., and Johnson, W. T. K., "Ambiguities in spaceborne synthetic aperture radar systems", *IEEE Transactions on Aerospace and Electronic Systems*, vol. AES-19, no. 3, pp. 389-397, May 1983.

[36] Moreira, A, Mittermayer, J., and Scheiber, R., "Extended Chirp Scaling Algorithm for Air- and Spaceborne SAR Data Processing in Stripmap and ScanSAR Imaging Modes", *IEEE Transactions on Geoscience and Remote Sensing*, vol.34, no. 5, pp. 1123-1136, September 1996.

[37] Ning, Ma, and Joo, Thiam Goh, "Ambiguity-Function-Based Techniques to Estimate DOA of Broadband Chirp Signals", *IEEE Transactions on signal Processing*, vol. 54, no. 5, pp. 1826-1839, May 2006.

[38] RTO Lecture Series, “Waveform Diversity for Advanced Radar Systems”. *NATO/PFP unclassified lectures* series under sponsorship of the Sensors and Electronics Technology Panel (SET) and Exchange Program of RTA, Hamburg, 15-16 September.

[39] Schmidt, R., “Multiple Emitter Location and Signal Parameter Estimation”, *IEEE Transactions on Antennas and Propagation*, vol. AP-34, no. 3, pp. 276-280, March 1986.

[40] Shan, Tie-Jun, Wax, M., and Kailath, T., “On Spatial Smoothing for Direction-of-Arrival Estimation of Coherent Signals”. *IEEE Transactions on Acoustics, Speech and Signal Processing,* vol. ASSP-33, no. 4, pp. 806-811, August 1985.

[41] Stoica, P., and Nehorai, A., “MUSIC, Maximum Likelihood, and Cramer-Rao Bound”, *IEEE Transactions on Acoustics, Speech, and Signal Processing,* vol. 37, no. 5, pp. 720-741, May 1989

[42] Stoica, P., and Nehorai, A., “MUSIC, Maximum Likelihood, and Cramer-Rao Bound: Further Results and Comparisons”, *IEEE Transactions on Acoustics, Speech, and Signal Processing,* vol. 38, no. 12, pp. 2140-2150, December 1990

[43] Stoica, P., and Nehorai, A., “Performance Study of Conditional and Unconditional Direction-of-Arrival Estimation”, *IEEE Transactions on Acoustics, Speech and Signal Processing*, vol. 38 no. 10, pp. 1783-1795, October. 1990

[44] Stoica, P., and Moses, R., *Introduction to Spectral Analysis*. Prentice Hall, 1997

[45] Suess., M., Grafmueller, R., and Zahn, R., “A Novel High Resolution, Wide Swath SAR System”, *International Geoscience and Remote Sensing Symposium 2001*, IGARSS ’01,vol. 3, pp. 1013-1015, 2001.

[46] Suess., M., and Wiesbeck, W., “Side-Looking Synthetic Aperture Radar System”. European Patent Application, EP 1 241 487 A1, September 18, 2002.

[47] Su, G., and Morf, M., “Signal Subspace Approach for multiple wideband emitter location”, *IEEE Transactions on Acoustics, Speech and Signal Processing*, ASSP-31, no. 6, pp. 1502-1522, December 1983.

[48] System study Technical Note (WP 1110+1120), *Active Receive-Only Digital Front-End for Radar and SAR*. EADS Astrium, March 2007.

[49] Tomiyasu, K., “Conceptual Performance of a Satellite Borne, Wide Swath Synthetic Aperture Radar”, *IEEE Transactions on Geoscience and Remote Sensing*, vol. GE-19, no. 2, pp. 108-116, April 1981.

[50] Van Trees, H. L., *Optimum array processing. Detection, Estimation, and Modulation Theory, Part IV*. Wiley, New York, 2002.

[51] Wax, M., Shan, T., and Kailath, T., "Spatio-temporal spectral analysis by eigenstructure methods", *IEEE Transactions on Acoustics, Speech and Signal Processing* , vol. ASSP-32, pp. 817-827, August 1984.

[52] Wang, H., and Kaveh, M., "Coherent signal-subspace processing for the detection and estimation of angles of arrival of multiple wide-band sources", *IEEE Transactions on Acoustics, Speech and Signal Processing*, vol. ASSP-33, pp. 823-831, August 1985.

[53] Wang, G., and Xia, X. G., "Iterative algorithm for direction of arrival estimation with wideband chirp signals", *Proceedings IEEE Radar, Sonar and Navigation*, vol. 147, no. 5, pp. 233-238, October 2000.

[54] Younis, M., Fischer, C., and Wiesbeck, W., "Digital Beamforming in SAR Systems", *IEEE Transactions on Geoscience and Remote Sensing*, vol. 41, no. 71, pp. 1735-1739, July 2003.

[55] Younis, M., Bordoni, F., Gebert, N., and Krieger, G., "Smart Multi-Aperture Radar Techniques for Spaceborne Remote Sensing", *Proceedings IEEE Geosciences and Remote Sensing Symposium*, IGARSS'08, pp. III-278-III-281, Boston, July 2008.